Technische Universität München
TUM School of Engineering and Design

# Dynamics of Lean Kerosene Flames of Different Premixing Levels Compared to Natural Gas

**Jan Kaufmann**

Vollständiger Abdruck der von der TUM School of Engineering and Design der Technischen Universität München zur Erlangung eines

DOKTORS DER INGENIEURWISSENSCHAFTEN (DR.-ING.)

genehmigten Dissertation.

Vorsitz:
Prof. Dr.-Ing. Michael W. Gee
Prüfer*innen der Dissertation:
1. Prof. Dr.-Ing. Thomas Sattelmayer
2. Prof. Dr.-Ing. Andreas Huber

Die Dissertation wurde am 19.06.2023 bei der Technischen Universität München eingereicht und durch die TUM School of Engineering and Design am 13.10.2023 angenommen.

# Vorwort

Die vorliegende Arbeit entstand im Rahmen meiner Tätigkeit als wissenschaftlicher Mitarbeiter am Lehrstuhl für Thermodynamik der Technischen Universität München. Das Projekt wurde als Teil des Verbundprojektes ECOFlex-turbo im Rahmen der AG Turbo durchgeführt und von GE Power sowie dem Bundesministerium für Wirtschaft und Klimaschutz (BMWK) unter dem Förderkennzeichen 0324295C gefördert.

Zuallererst gilt mein Dank meinem Doktorvater, Herrn Prof. Dr.–Ing. Thomas Sattelmayer, für die Möglichkeit, unter seiner Betreuung zu promovieren. Vielen Dank für das entgegengebrachte Vertrauen und Ihre Unterstützung! Auch möchte ich mich herzlich für die Gelegenheit bedanken, an der Lehrveranstaltung „Grundlagen der Thermodynamik“ mitzuwirken und so auch abseits des fachlichen Erkenntnisgewinns wertvolle Erfahrungen zu sammeln.

Herrn Prof. Dr.-Ing. Andreas Huber danke ich herzlich für die freundliche Übernahme des Koreferats und die Begutachtung meiner Arbeit. Weiterhin danke ich Herrn Prof. Dr.-Ing. Michael W. Gee für den Vorsitz bei der mündlichen Prüfung.

Die freundschaftliche Atmosphäre, die weit über die reine Zusammenarbeit hinaus ging, hat die Zeit am Lehrstuhl für mich zu einem besonderen Erlebnis gemacht. Aus vielen Kolleginnen und Kollegen sind Freunde geworden. Besonderer Dank gilt dabei Manuel Vogel, der gemeinsam mit mir alle Höhen und Tiefen unseres Forschungsprojektes gemeistert hat sowie Daniel Heilbronn, der mit mir die „Grundlagen der Thermodynamik“ durch die Corona-Zeit und wechselnde Zuständigkeiten begleitet hat. Bessere Teampartner als euch beide hätte ich mir nicht wünschen können.

Unserem Oberingenieur Dr.-Ing. Christoph Hirsch danke ich für die zahlreichen interessanten und lehrreichen Diskussionen, Anregungen und Denkanstöße. Für die wertvolle Hilfe bei der Prüfstandsanpassung danke ich den Mitarbeitern der mechanischen und der elektrischen

Werkstatt. Helga Bassett, Sigrid Schulz-Reichwald und Brigitte Hirsch danke ich für die Unterstützung bei allen organisatorischen und administrativen Angelegenheiten.

Weiterhin gilt mein Dank allen Studierenden und wissenschaftlichen Hilfskräften, die an diesem Forschungsprojekt beteiligt waren. Besonders hervorheben möchte ich Muhammad Yasir, Jannes Papenbrock und Paul Siegele, die durch ihre herausragenden Leistungen wesentlich zum Erfolg der Arbeit beigetragen haben.

Abschließend möchte ich von ganzem Herzen meinen Freunden und meiner Familie für den Rückhalt während meiner gesamten Ausbildung danken. Vor allem dir, liebe Yue, vielen Dank für all deine Geduld und Unterstützung!

Danke!

München, im Januar 2024 Jan Kaufmann

# Kurzfassung

Die Option der Verbrennung von Flüssigbrennstoffen in stationären Gasturbinen erhöht die Brennstoffflexibilität und ist daher erstrebenswert. Um die strengen Emissionsvorschriften einzuhalten, werden stationäre Gasturbinen in der Regel mager vorgemischt betrieben, was die Entwicklung thermoakustischer Instabilitäten begünstigt. Während thermoakustische Instabilitäten bei mager-vorgemischter Erdgasverbrennung bereits umfangreich erforscht wurden, gibt es bisher nur wenige Untersuchungen zu thermoakustischen Instabilitäten bei der mager-vorgemischten Verbrennung von flüssigen Brennstoffen.

Die vorliegende Arbeit vergleicht die longitudinale Flammendynamik von mager-vorgemischter Kerosin- und Erdgasverbrennung unter atmosphärischen Bedingungen. Anhand von experimentell gemessenen Flammentransferfunktionen wird die Flammendynamik über einen weiten Betriebsbereich charakterisiert. Es werden Experimente für zwei Flüssigbrennstoffkonfigurationen mit unterschiedlichem Vormischgrad durchgeführt und mit perfekt und technisch vorgemischter Erdgasverbrennung verglichen. Es wird gezeigt, dass die Flammendynamik nur schwach von der Brennstoffart abhängig ist, solange Brennstoff und Luft vollständig vorgemischt sind. Die beobachteten Trends im Fall der teilweise vorgemischten Flüssigbrennstoffverbrennung weichen dagegen deutlich von den anderen Konfigurationen ab.

Zur Interpretation der Ergebnisse wird ein analytisches Flammentransferfunktionsmodell aufgestellt. Die unterschiedlichen Rückkopplungsmechanismen, die zur Flammendynamik beitragen, werden dabei einzeln modelliert und aufsummiert. Die Modellparameter für die Erdgasverbrennung und den vollständig vorgemischten Flüssigbetrieb können linear mit der Flammengeometrie verknüpft werden. Dies lässt darauf schließen, dass die beobachtete Flammendynamik bei der Verbrennung von Erdgas und im vollständig vorgemischten Flüssigbetrieb auf dieselben Rückkopplungsmechanismen zurückzuführen ist. Die gute Übereinstimmung zwischen den experimentellen Daten und dem Mo-

dell über einen breiten Betriebsbereich erlaubt die physikalische Interpretation des Modells als Zerlegung der Flammentransferfunktion in die verschiedenen Rückkopplungsmechanismen. Von besonderer Bedeutung sind dabei Äquivalenzverhältnisschwankungen, die bei technischer Vormischung durch das akustische Feld am Ort der Brennstoffeindüsung verursacht werden. Diese unterscheiden sich zwischen dem Erdgas- und dem vollständig vorgemischten Kerosinbetrieb. Die beobachteten Unterschiede zwischen den Flammentransferfunktionen lassen sich großteils hierauf zurückführen. Die experimentellen Ergebnisse für den teilweise vorgemischten Flüssigbrennstoffbetrieb können dagegen nicht mit dem analytischen Modellansatz reproduziert werden, was darauf hindeutet, dass die relevanten Rückkopplungsmechanismen anderer Natur sind.

## Abstract

To enhance fuel flexibility, it is desirable to have the option of liquid fuel combustion in stationary gas turbines. To comply with emission regulations, stationary gas turbines are usually operated under lean premixed conditions, which are prone to developing thermoacoustic instabilities. While extensive research on this topic has been conducted for lean premixed natural gas operation, the research on thermoacoustic instabilities of lean premixed liquid fuel combustion has been limited so far. This study compares the longitudinal flame dynamics of kerosene and natural gas combustion in a lean premixed gas turbine combustor under atmospheric conditions. Flame transfer functions are measured over a broad range of operating conditions to quantify flame dynamics. Experiments are conducted for two liquid fuel configurations with different degrees of premixing and compared to perfectly and technically premixed natural gas combustion. Results show that the fuel type has little impact on the flame dynamics as long as fuel and air are fully premixed. In contrast, the trends for partially premixed liquid fuel combustion differ from all others. A physically-motivated analytical flame transfer function model is applied. The various feedback mechanisms contributing to the flame dynamics are individually modeled and then superposed. The model parameters can be linearly linked to the flame geometry for natural gas and fully premixed liquid fuel combustion, suggesting that these configurations share the same feedback mechanisms. The good agreement between the experimental data and the model allows for the physical interpretation of the model as a decomposition of the flame transfer function into the various feedback mechanisms. Equivalence ratio fluctuations caused by the acoustic field at the point of fuel injection in the case of technical premixing were identified as particularly important, as these differ between natural gas and fully premixed kerosene operation. The observed differences between the flame transfer functions can largely be attributed to this. The experimental results from the partially premixed liquid fuel combustion cannot be reproduced by the analytical model, thus indicating that the relevant feedback mechanisms are of a different nature.

# Contents

# List of Figures

# List of Tables

# Nomenclature

## Latin letters

| | |
|---|---|
| $c$ | Speed of sound [m/s] |
| $c$ | POD mode coefficient [-] |
| $c_p$ | Isobaric specific heat capacity [J/(kgK)] |
| $d$ | Diameter [m] |
| $f$ | Frequency [1/s] |
| $f$ | Riemann invariant [m/s] |
| $g$ | Riemann invariant [m/s] |
| $h$ | Specific enthalpy [J/kg] |
| $\mathbf{H}$ | Coefficient matrix [-] |
| $i$ | Imaginary unit [-] |
| $I$ | Normalized chemiluminescence intensity [-] |
| $k^{+/-}$ | Wave number [1/m] |
| $l$ | Length [m] |
| $m$ | Mass [kg] |
| $\dot{m}$ | Mass flow [kg/s] |
| $n_S$ | Vortex interaction index [-] |
| $p$ | Pressure [Pa] |
| $P_{th}$ | Thermal power [W] |
| $\dot{Q}$ | Heat release rate [W] |
| $R$ | Specific gas constant [J/(kgK)] |
| $R^{+/-}$ | Reflection coefficient [-] |
| $\mathbf{SM}$ | Scattering matrix [-] |
| $SMD$ | Sauter mean diameter [m] |
| $t$ | Time [s] |

| | |
|---|---|
| $T$ | Oscillation period [s] |
| $T$ | Temperature [K] |
| $T^{+/-}$ | Transmission coefficient [-] |
| $\mathbf{TM}$ | Transfer matrix [-] |
| $u$ | Flow velocity [m/s] |
| $x$ | Spatial coordinate [m] |

## Greek letters

| | |
|---|---|
| $\alpha$ | FTF model parameter [s] |
| $\gamma$ | Specific heat ratio [kJ/kgK] |
| $\theta$ | Temperature rise [K] |
| $\vartheta$ | Specific impedance [-] |
| $\lambda$ | Wave length [m] |
| $\rho$ | Density [kg/m$^3$] |
| $\sigma$ | Time delay width [s] |
| $\tau$ | Time delay [s] |
| $\varphi$ | Phase angle [rad] |
| $\phi$ | Equivalence ratio [-] |
| $\omega$ | Angular frequency [rad/s] |
| $\mathbf{\Omega}$ | Transformation matrix [-] |

## Operators

| | |
|---|---|
| $(...)'$ | Perturbation |
| $\bar{(...)}$ | Time-averaged value |
| $(...)^{fg}$ | $fg$ notation of a matrix |
| $(...)^{pu}$ | $pu$ notation of a matrix |
| $(...)^{A}$ | Forcing location upstream |
| $(...)^{B}$ | Forcing location downstream |
| $\lvert...\rvert$ | Magnitude |
| $\angle ...$ | Phase angle |

| | |
|---|---|
| $(...)^{\dagger}$ | Pseudo-inverse |
| $(...)^{\top}$ | Transpose |
| $\mathcal{O}$ | Order of magnitude |

## Subscripts

| | |
|---|---|
| A | Upstream excitation |
| air | Main air |
| at | Atomizing air |
| B | Downstream excitation |
| B | Burner outlet |
| c | Cold |
| cc | Combustion chamber |
| cg | Center of gravity |
| d | Downstream |
| evap | Evaporation |
| fl | Flame |
| h | Hot |
| IB | Injection to burner outlet |
| kero | Kerosene |
| M | Mass flow fluctuation contribution |
| mix | Mixing |
| NG | Natural gas |
| $\phi$ | Equivalence ratio fluctuation contribution |
| pp | Perfectly premixed |
| pre | Preheater |
| S | Swirl fluctuation contribution |
| st | Stochiometric |
| tp | Technically premixed |
| u | Upstream |

## Dimensionless numbers

| | |
|---|---|
| Ma | Mach number |
| Re | Reynolds number |
| Sr | Strouhal number |

## Abbreviations

| | |
|---|---|
| $A^2EV$ | Advanced$^2$ En-Vironmental burner |
| ALR | Air-liquid ratio |
| CFD | Computational fluid dynamics |
| FTF | Flame transfer function |
| $k_{30}$ | Partially premixed kerosene combustion configuration |
| $k_{70}$ | Fully premixed kerosene combustion configuration |
| MMM | Multi-microphone method |
| $NG_{pp}$ | Perfectly premixed natural gas combustion configuration |
| $NG_{tp}$ | Technically premixed natural gas combustion configuration |
| $NO_x$ | Nitrogen oxides |
| POD | Proper orthogonal decomposition |
| TMM | Two-microphone method |

# 1 Introduction

Modern land-based gas turbines are essential for meeting the increasing global demand for electricity due to their flexibility in application. They can cover peak loads and base-load supply alike and offer short start-up times. Despite limited fossil fuel resources and the growth of renewable energy sources, gas turbines will therefore continue to play a crucial role in the future energy supply [34].

In order to reliably supply electrical energy, especially in case of high prices or limited availability of the primary fuel, fuel flexibility becomes a matter of great importance in modern gas turbine technology [16,55,100]. This issue has recently gained importance, particularly due to the politically motivated shortage of natural gas supplies following the Crimean Crisis in 2014 [44] and the Russian invasion of Ukraine in 2022 [46]. Consequently, developing combustion systems capable of burning liquid fuels in gas turbines is a key objective of current research. In the case of liquid fuel combustion, the mixture preparation involves additional subprocesses, namely fuel atomization, droplet-air mixing, and fuel evaporation, which increase the complexity of the process. Besides, modern heavy-duty gas turbines have to comply with restrictive emission regulations [86]. Meeting those requirements while at the same time enhancing overall efficiency and flexibility are challenges to ensure that gas turbines remain a viable energy option in the face of ecological concerns and competition with other energy sources.

One major pollutant group emitted by gas turbines are nitrogen oxides ($NO_x$). They contribute to the formation of ground-level ozone, acid rain, and smog, all of which have harmful effects on human health, vegetation, and ecosystems [4]. $NO_x$ also contribute to the depletion of the ozone layer. Because the formation of ground-level ozone contributes to

the greenhouse effect, $NO_x$ is also considered a greenhouse gas [39]. The formation of $NO_x$ emissions depends heavily on the local combustion temperature. The control of the flame temperature thus offers considerable potential for reducing $NO_x$ emissions.

Historically, gas turbines relied on diffusion combustion due to its inherent stability of the combustion process [28]. In such systems, fuel and air are injected separately. Mixing and combustion occur simultaneously in the combustion chamber. For this reason, most of the reaction takes place at almost stoichiometric conditions, and consequently, particularly high flame temperatures are reached [48]. The transition from diffusion to premixed combustion has significantly reduced $NO_x$ emissions [29, 51, 89]. Here, the mixing process is decoupled from combustion, and fuel and air enter the combustion chamber as a homogeneous mixture. Combustion takes place under lean conditions, i.e., with an excess of air. This reduces the local flame temperatures and, thus, the $NO_x$ emissions.

However, the emission reductions come at the cost of increased susceptibility to combustion instabilities, such as flame extinguishing and flame flashback into the burner. Furthermore, lean premixed combustion favors the formation of thermoacoustic combustion instabilities. These can lead to significant pressure and temperature oscillations in the combustion chamber and thereby affect the efficiency and reliability of the system [19, 29, 40, 53].

## 1.1 Thermoacoustic Instabilities

Thermoacoustic instabilities arise from an undesirable constructive interaction between the unsteady flame heat release and the system acoustics. Small-scale perturbations in the acoustic field lead to fluctuations in the flame heat release rate. An unsteady heat release rate generally represents a source of sound due to the associated volume fluctuation. The sound waves emitted by the flame travel up- and downstream and are partially reflected back to the flame at the combustion chamber walls and at the

inlets and outlets. This again causes heat release fluctuations and hence acoustic perturbations.

For harmonic oscillations, the effect of the interaction between the pressure fluctuation in the reaction zone, $p'$ and the flame heat release rate oscillation $\dot{Q}'$ can be either amplifying or damping depending on their phase relation. This was first investigated by Lord Rayleigh in 1878 [74]. He discovered that the oscillations would be amplified most if the heat is added at the instant of the pressure maximum, or in other words if $p'$ and $\dot{Q}'$ are in phase and vice versa. The Rayleigh criterion, which is derived from this, states that a thermoacoustic instability can only occur if the integral product of heat release fluctuation $\dot{Q}'$ and pressure fluctuation $p'$ is positive over a period $T$:

$$\int_0^T p'(t) \cdot \dot{Q}'(t) dt > 0. \tag{1.1}$$

The sign of this integral is determined by the phase difference between the two fluctuations. The integral is positive for absolute phase differences smaller than $\pi/2$, and the fluctuations are amplified. If the value is greater than $\pi/2$, the fluctuations are damped.

The Rayleigh criterion is necessary but not sufficient for the occurrence of thermoacoustic instabilities. In addition, there needs to be an increase in the system's acoustic energy, which can only occur if the energy added to the acoustic field by the flame exceeds the damping and losses in the combustor [54, 70]. In such cases, the fluctuation variables experience a persistent increase, potentially leading to unbounded amplitude values. However, in practice, nonlinear effects hinder this growth and establish a limit cycle characterized by the maximum fluctuation amplitudes [21].

### 1.1.1 Thermoacoustic Modes

The thermoacoustic oscillations appear as natural modes at distinct eigenfrequencies of the system. The modes can be categorized according to the direction of the oscillations with respect to the flow direction.

For narrow combustion chambers with a length significantly larger than their height, the following modes can develop:

- **Longitudinal modes:** These modes typically exhibit eigenfrequencies in the range below 1000 Hz [23]. The oscillation direction is parallel to the main flow direction in the combustion chamber. The wave propagation is usually analyzed as one-dimensional. Because the acoustic wavelength is considerably longer than the flame length, the flame can be assumed to be acoustically compact. This means that the acoustic properties remain constant across the flame region. In gas turbines, acoustic waves are commonly reflected at the combustor outlet due to the fast acceleration of the flow beyond the combustor. As a result, longitudinal modes often appear as standing waves within the combustion chamber [23, 43].

  As discussed further in Section 4.3, the flame response of longitudinal thermoacoustic oscillations is commonly dominated by convective effects. Acoustic perturbations are convectively transported from the burner to the flame, where they cause heat release perturbations $\dot{Q}'$. Due to the convection, the heat release perturbations lag the pressure perturbations $p'$ by a convective time delay $\tau$. To obtain self-excitation according to the Rayleigh criterion, the convective time delay $\tau$ must be related to the oscillation period $T$ as follows:

$$0 < \tau < \frac{T}{4}, \qquad \frac{3T}{4} < \tau < \frac{5T}{4}, \qquad etc. \tag{1.2}$$

- **Azimuthal modes:** In annular combustors, azimuthal modes can occur. These modes cause oscillations in the circumferential direction, with frequencies generally within the same range as longitudinal modes. For adjacent burners within an annular combustor, the azimuthal mode can modulate the axial mass flow in the corresponding burners and also generate transverse excitation. Acoustic wave propagation can therefore be described by a combination of one- and two-dimensional approaches [30]. Usually, it is valid to consider the system as acoustically compact [8].

- **Transverse modes:** Transverse modes occur at eigenfrequencies above 1000 Hz [82]. The oscillation direction is perpendicular to the main flow direction in the combustion chamber. The dimensions of the flame length and the acoustic wavelength are in the same order of magnitude. The acoustic field, therefore, changes considerably over the flame volume. As a result, it cannot be assumed that the flame is acoustically compact. Hence, a spatially resolved analysis of the interaction between acoustics and flame is required. The resulting acoustic field is multi-dimensional [19,65].

### 1.1.2 Feedback Mechanisms

Essential for the formation of a self-excited thermoacoustic oscillation is the existence of a feedback mechanism to close the loop. For this reason, extensive studies on this topic have been conducted in recent years. For lean premixed combustion, the following mechanisms have been found to be dominant in the formation of thermoacoustic instabilities:

- **Velocity perturbations:** The feedback is initialized by a deflection of the velocity field and the associated modulation of the flame heat release. The hereby generated sound wave is partially reflected at the combustion chamber exit and consequently causes, in turn, a deflection of the velocity field.
- **Forced coherent flow structures:** Acoustic perturbations at the burner can cause modulations of the flow field, resulting in coherent flow structures. These structures pulsate with the excitation frequency and generate significant heat release fluctuations by modulating the flame surface, the reaction rate, or both [66,69,79]. In swirl-stabilized systems, swirl fluctuations additionally contribute to the generation of instabilities. They are generated by the acoustic waves impinging on the swirler [37,45].
- **Equivalence ratio fluctuations:** In technical combustion systems, fuel supply and mixing usually take place in the burner. Pressure

and velocity perturbations at the fuel injector nozzle cause fluctuations of the equivalence ratio $\phi$. The equivalence ratio is defined as the ratio of fuel mass flow rate to air mass flow rate, normalized by the stoichiometric ratio of the two [93]:

$$\phi = \frac{\dot{m}_{fuel}/\dot{m}_{air}}{\dot{m}_{fuel,st}/\dot{m}_{air,st}}. \tag{1.3}$$

The equivalence ratio fluctuations $\phi'$ are convectively transported with the mean flow. In the flame, they cause a modulation of the heat release rate. This can be either directly via the energy content of the flow and also via the flame temperature and thus the resulting reaction rate [12,41,52,76,85]. In liquid fuel combustion systems, the generation of equivalence ratio fluctuations is affected by the additional processes of atomization and evaporation, which may react to the acoustic perturbations [13,27].

- **Entropy waves:** Entropy waves s′ are perturbations in the hot gas temperature that are generated by the heat release of the flame resulting from equivalence ratio fluctuations. A feedback mechanism can be formed if such a perturbation is convected into a choked or nearly-choked nozzle at the combustor exit, where it is reflected as a pressure wave [26,59,72,90].

In addition, turbulent noise and naturally occurring flow structures like vortex separation at edges can act as a trigger to start an instability. However, they usually do not participate in the feedback cycle [15,91].

### 1.1.3 Spray Combustion

For natural gas combustion, thermoacoustic oscillations in lean premixed combustion have already been extensively studied [23,38]. Research on liquid combustion has mainly focused on the primary zone of aero engines, in which usually rich, non-premixed conditions prevail, and the combustion remains incomplete [26,60,97]. So far, only limited research

has been conducted on thermoacoustic instabilities of lean premixed liquid fuel combustion [75]. Compared to natural gas, liquid fuel combustion includes the additional sub-processes of fuel atomization, spray dispersion, and evaporation [19]. Consequently, especially the formation of equivalence ratio fluctuations $\phi'$ at the burner outlet may exhibit different mechanisms.

Sujith [92] experimentally investigated the influence of acoustic excitation on the fuel spray for high forcing amplitudes. He reported that high-amplitude velocity oscillations reduce the length of the spray cone and spray velocity. Moreover, he demonstrated that the impact of acoustic oscillations on the spray is contingent on the phase of the acoustic field at the spray injection site. The effect is strongest when the spray is injected at an acoustic velocity antinode, i.e., when the acoustic velocity amplitude is at its maximum, and the corresponding acoustic pressure amplitude is at its minimum.

Eckstein [27] investigated the influence of acoustic velocity fluctuations on the droplet size distribution under non-premixed, rich conditions. His findings indicate that even minor velocity fluctuations can significantly impact the droplet size distribution, resulting in a modulation of the heat release rate. The unstable oscillation frequency was observed to be predominantly governed by the droplets' transport and combustion time scales.

Chishty [11] explored the influence of acoustic perturbations for lean kerosene combustion. He reported that sprays are particularly susceptible to oscillations at low frequencies. The associated cut-off frequency is determined by the relaxation time of the droplets, which correlates with the mean droplet size. More precisely, the spray reacts to acoustic disturbances when the time scales of the droplet lifetime correspond to those of an acoustic period.

Christou et. al. [13] investigated the effects of air mass flow oscillations on droplet formation and transport for a pre-filming airblast atomizer. They observed that fluctuations in air mass flow cause oscillations of

the mean droplet diameter and modulations of the droplet velocity. They concluded that even if the average evaporation quality is only marginally affected by acoustic excitation, the different inertia of droplets of different sizes causes the segregation of small droplets at velocity antinodes, whereas bigger droplets remain unaffected by the excitation. Achury [3] reported similar findings in CFD simulations when replicating experimental data from Gurubaran [35].

## 1.2 Thesis Outline

This study compares longitudinal thermoacoustic oscillations in a lean premixed gas turbine combustor fueled by natural gas and kerosene under atmospheric conditions. A downscaled version of the A$^2$EV burner is retrofitted using a central twin-fluid nozzle to inject liquid fuel. This allows for investigating the combustion of liquid fuel and natural gas using the same burner hardware. Flame transfer functions (FTFs) are used as a measure to quantify flame dynamics. The comparison of FTFs across different operating conditions and configurations aims to identify similarities and differences in sensitivity. Particular emphasis is placed on highlighting the similarities and differences between the configurations. Based on the experimental results, an analytical FTF model is derived. The model incorporates physically-motivated fit parameters to replicate the individual feedback mechanisms. The good agreement between the experimental data and the model allows for the physical interpretation of the model as a decomposition into the various feedback mechanisms. Lastly, the model is extended to predict the FTF for a given operating point.

The thesis is structured as follows: Chapter 2 presents the relevant thermoacoustic theory. The derivation of the linear wave equation is explained, followed by a representation of wave propagation in simple ducts by solving the wave equation. The propagation of waves in acoustic systems is described through low order network models. Finally, FTFs

are introduced as measure of flame dynamics. Chapter 3 describes the experimental setup, including an overview of the atmospheric single burner test rig and the modular swirl burner used for the investigations. The operation range and the burner configurations studied are also introduced. Chapter 4 outlines the diagnostic equipment and methods used in the study. Besides the description of the experimental FTF determination, this includes a review of existing analytical FTF modeling approaches in general and the applied models in particular. Chapter 5 presents and discusses the stationary operation properties of the combustion system. The degree of premixing for the different liquid fuel configurations is determined based on fuel droplet size measurements and $NO_x$ emission measurements. Stationary OH*-chemiluminescence flame images are presented and compared across all configurations. Chapter 6 focuses on the dynamic properties of the combustion system. The scattering matrices for the burner with and without liquid fuel injector are compared with each other, followed by a discussion of FTFs for all operating points. Chapters 7 and 8 deal with the analytical FTF model. Scaling rules for the model fit parameters are derived in Chapter 7. The approach of linking the parameters to the flame geometry is motivated. The reconstructed FTFs are compared to the experimental data and interpreted with regard to the importance of the individual coupling mechanisms. Chapter 8 extends the model to predict the FTF based on the operating conditions. To achieve this, the flame geometry for the considered operating point is predicted using proper orthogonal decomposition (POD). Finally, a summary of the thesis is provided in Chapter 9.

# 2 Longitudinal Thermoacoustics

In this chapter, the theoretical foundation for analyzing thermoacoustic instabilities is presented. First, the basics of linear 1D acoustics are explained. This includes deriving the solution of the linear wave equation, which describes the propagation of acoustic waves. Section 2.2 introduces low order network modeling as a technique for characterizing intricate acoustic networks by combining multiple simple elements. Subsequently, the fundamentals of thermoacoustics are discussed, and the concept of FTFs, which are commonly used as a measure to describe flame dynamics, is introduced.

## 2.1 Linear 1D Acoustics

The propagation of acoustic waves in time and space can be described based on conservation equations. Neglecting body forces and viscous stress, the conservation equations for mass (cf. Equation 2.1) and momentum (cf. Equation 2.2) can be formulated as follows:

$$\frac{\partial \rho}{\partial t} + \frac{\partial \rho u_i}{\partial x_i} = 0 \tag{2.1}$$

$$\frac{\partial \rho u_i}{\partial t} + u_j \frac{\partial \rho u_i}{\partial x_j} + \frac{\partial p}{\partial x_i} = 0. \tag{2.2}$$

Here, $p$ represents the pressure, $\rho$ is the density, $x_{i,j}$ are the cartesian coordinates, and $u_{i,j}$ is the corresponding velocity field.

If the radial extension of the combustor is small compared to the axial length and if, furthermore, the oscillation frequency is low, the waves can be assumed to be one-dimensionally propagating plane waves. Conse-

quently, the entire problem becomes one-dimensional, and only the axial direction of the velocity field and the coordinates is considered:

$$u_{i,j} = u \qquad x_{i,j} = x. \tag{2.3}$$

Neglecting stochastic fluctuations, the flow variables can be split into their mean quantity ($\bar{...}$) and a fluctuating component ($...'$) as:

$$p(x,t) = \bar{p}(x,t) + p'(x,t) \tag{2.4}$$
$$\rho(x,t) = \bar{\rho}(x,t) + \rho'(x,t) \tag{2.5}$$
$$u(x,t) = \bar{u}(x,t) + u'(x,t). \tag{2.6}$$

### 2.1.1 Derivation of the Wave Equation

The one-dimensional wave equation is first derived without taking into account the mean flow. Subsequently, considering the mean flow velocities yields the convective wave equation. Applying the decomposition based on Equations 2.4-2.6 to the conservation equations and assuming that the fluctuating components are significantly smaller than the mean, the products of the fluctuating parts cancel out. Equations 2.1 and 2.2 can be reformulated as:

$$\frac{\partial \rho'}{\partial t} + \bar{u}\frac{\partial \rho'}{\partial x} + \bar{\rho}\frac{\partial u'}{\partial x} = 0 \tag{2.7}$$
$$\bar{\rho}\left(\frac{\partial u'}{\partial t} + \bar{u}\frac{\partial u'}{\partial x}\right) + \frac{\partial p'}{\partial x} = 0. \tag{2.8}$$

In gas turbine combustors, the Mach number of the mean flow $Ma = \bar{u}/c$ is often low. This allows to neglect the mean flow velocity. Equations 2.7 and 2.8 thus simplify to:

$$\frac{\partial \rho'}{\partial t} + \bar{\rho}\frac{\partial u'}{\partial x} = 0 \tag{2.9}$$
$$\bar{\rho}\frac{\partial u'}{\partial t} + \frac{\partial p'}{\partial x} = 0. \tag{2.10}$$

For an isentropic flow, the oscillations of acoustic pressure $p'$ and density $\rho'$ are coupled via the speed of sound $c$:

$$\rho' = \frac{p'}{c^2}. \tag{2.11}$$

This allows to derive the wave equation by partially deriving the mass conservation equation (cf. Eq. 2.9) with respect to $x$ and the momentum conservation equation (cf. Eq. 2.10) with respect to $t$ and subtracting the two. For constant mean density $\rho \neq \rho(x, y, z)$ this yields:

$$\frac{\partial^2 p'}{\partial t^2} - c^2 \frac{\partial^2 p'}{\partial x^2} = 0. \tag{2.12}$$

For non-neglectable homegeneous mean flow $\bar{u} \neq \bar{u}(x, y, z)$, the convective wave equation can be derived from Equations 2.7 and 2.8:

$$\left(\frac{\partial}{\partial t} + \bar{u}\frac{\partial}{\partial x}\right)^2 p' - c^2 \frac{\partial^2 p'}{\partial x^2} = 0. \tag{2.13}$$

### 2.1.2 Solution of the Wave Equation

First, the solution of the one-dimensional wave equation with no mean flow is outlined. Subsequently, this is transferred to the solution of the one-dimensional convective wave equation. The wave equation (cf. Eq. 2.12) can be solved analytically using d'Alembert's method:

$$\frac{p'(x,t)}{\rho c} = f(x - ct) + g(x + ct). \tag{2.14}$$

Herein $f$ and $g$ are the so-called Riemann Invariants. They are arbitrary, frequency-dependent functions that depend on the initial values and boundary conditions and represent upstream ($f$) and downstream ($g$) traveling waves propagating with the speed of sound.

Inserting the solution of the wave equation (cf. Eq. 2.14) into the mass conservation equation for no mean flow (cf. Eq. 2.9) yields the corresponding acoustic velocity fluctuation:

$$u'(x,t) = f(x - ct) - g(x + ct). \tag{2.15}$$

Equations 2.14 and 2.15 can be rearranged for $f$ and $g$ to:

$$f(x,t) = \frac{1}{2}\left(\frac{p'(x,t)}{\rho c} + u'(x,t)\right) \tag{2.16}$$

$$g(x,t) = \frac{1}{2}\left(\frac{p'(x,t)}{\rho c} - u'(x,t)\right). \tag{2.17}$$

Assuming $f$ and $g$ to be harmonic in time, they can be written as a function of the angular frequency $\omega = 2\pi f$:

$$\frac{p'(x,t)}{\bar{\rho} c} = f \cdot e^{(i\omega t - ikx)} + g \cdot e^{(i\omega t + ikx)} \tag{2.18}$$

$$u'(x,t) = f \cdot e^{(i\omega t - ikx)} - g \cdot e^{(i\omega t + ikx)}. \tag{2.19}$$

$k$ denotes the wave number, which represents the spatial frequency, i.e., the number of cycles in a unit distance of a wave. It is defined as:

$$k = \frac{\omega}{c}. \tag{2.20}$$

The solution of the convective wave equation (cf. Eq. 2.13) follows a similar procedure. Again, the d'Alembert method is applied and combined with the mass conservation equation (cf. Eq. 2.7) to obtain the solutions for $p'$ and $u'$:

$$\frac{p'(x,t)}{\rho c} = f(x - (c + \bar{u})t) + g(x + (c - \bar{u})t) \tag{2.21}$$

$$u'(x,t) = f\left(x - (c + \bar{u})t\right) - g(x + (c - \bar{u})t). \tag{2.22}$$

Compared to the case without mean flow, the propagation speed of the Riemann Invariants $f$ and $g$ is modified by the mean flow field. $f$ is propagating downstream with a speed of $c + \bar{u}$, and $g$ is propagating against the mean flow with a speed of $c - \bar{u}$.

Again assuming harmonic functions for $f$ and $g$, they can be rewritten to:

$$\frac{p'(x,t)}{\bar{\rho} c} = f \cdot e^{(i\omega t - ik^+ x)} + g \cdot e^{(i\omega t + ik^- x)} \tag{2.23}$$

$$u'(x,t) = f \cdot e^{(i\omega t - ik^+ x)} - g \cdot e^{(i\omega t + ik^- x)}. \tag{2.24}$$

Here, $k^{\pm}$ denotes the convective wave number defined as:

$$k^{\pm} = \frac{\omega}{c \pm \bar{u}}. \tag{2.25}$$

## 2.2 Low Order Network Modeling

When different acoustic components are connected in series, the acoustic field altered by one component becomes the inlet condition for the other. Therefore, it is convenient to treat complex acoustic geometries as networks of interconnected simple elements with well-known acoustic properties. The acoustic properties of each element are represented by transfer matrices that linearly link the acoustic state variables upstream and downstream of the element. Low order network models are originally known from electrical engineering and have become a commonly used way to represent the acoustic properties of gas turbine combustors with the aim to predict thermoacoustic instabilities [20,62,63]. Some simple elements, such as straight ducts, area jumps, joints, and forks, can be described by analytical expressions [32]. In principle, any acoustic element can be integrated into a network model by its acoustic transfer matrix obtained from measurements, analytical models, or numerical simulations.

The transfer matrix couples either the acoustic pressure (cf. Eq. 2.26) and velocity fluctuations or the Riemann invariants $f$ and $g$ (cf. Eq. 2.27) upstream (index u) and downstream (index d) of the element of interest as follows:

$$\begin{bmatrix} \frac{p'}{\bar{\rho}c} \\ u \end{bmatrix}_d = \underbrace{\begin{bmatrix} TM_{11} & TM_{12} \\ TM_{21} & TM_{22} \end{bmatrix}}_{\mathbf{TM}^{pu}} \begin{bmatrix} \frac{p'}{\bar{\rho}c} \\ u \end{bmatrix}_u \tag{2.26}$$

$$\begin{bmatrix} f \\ g \end{bmatrix}_d = \underbrace{\begin{bmatrix} TM_{11} & TM_{12} \\ TM_{21} & TM_{22} \end{bmatrix}}_{\mathbf{TM^{fg}}} \begin{bmatrix} f \\ g \end{bmatrix}_u. \tag{2.27}$$

$\mathbf{TM}^{pu}$ and $\mathbf{TM}^{fg}$ can be converted into another as follows [32]:

$$\mathbf{TM}^{pu} = \mathbf{\Omega} \cdot \mathbf{TM}^{fg} \cdot \mathbf{\Omega}^{-1} \tag{2.28}$$

$$\mathbf{TM}^{fg} = \mathbf{\Omega}^{-1} \cdot \mathbf{TM}^{pu} \cdot \mathbf{\Omega}. \tag{2.29}$$

Here, $\mathbf{\Omega}$ represents a linear coordinate transformation matrix and $\mathbf{\Omega}^{-1}$ its inverse:

$$\mathbf{\Omega} = \begin{bmatrix} 1 & 1 \\ 1 & -1 \end{bmatrix} \tag{2.30}$$

$$\mathbf{\Omega}^{-1} = \frac{1}{2} \begin{bmatrix} 1 & 1 \\ 1 & -1 \end{bmatrix}. \tag{2.31}$$

The scattering matrix $\mathbf{SM}^{fg}$ provides another common way to describe the acoustic properties of an element. The matrix relates the waves $f_u$ and $g_d$ traveling towards the element from both directions to the waves $g_u$ and $f_d$ traveling outwards. The acoustic element can be considered a scattering process, where the waves that enter the element are split into a reflected and transmitted wave. These two waves are characterized by the complex reflection coefficients ($R^+$, $R^-$) and transmission coefficients ($T^+$, $T^-$) of the scattering matrix. The advantage of scattering matrices over transfer matrices is that they can be interpreted more intuitively because the waves leaving and entering the acoustic element appear separately. The scattering matrix is defined as follows [1,32]:

$$\begin{bmatrix} f_d \\ g_u \end{bmatrix} = \underbrace{\begin{bmatrix} T^+ & R^- \\ R^+ & T^- \end{bmatrix}}_{\mathbf{SM}^{fg}} \begin{bmatrix} f_u \\ g_d \end{bmatrix}. \tag{2.32}$$

Reformulating Equations 2.27 and 2.32, the following relationship between the transfer matrix $\mathbf{TM}^{fg}$ and the scattering matrix $\mathbf{SM}^{fg}$ can be derived [67]:

$$\mathbf{SM}^{fg} = \frac{1}{\mathrm{TM}_{22}^{fg}} \begin{bmatrix} TM_{11}^{fg}TM_{22}^{fg} - TM_{12}^{fg}TM_{21}^{fg} & TM_{12}^{fg} \\ -TM_{21}^{fg} & 1 \end{bmatrix}. \tag{2.33}$$

## 2.3 Flame Dynamics

To accurately predict thermoacoustic oscillations in gas turbine combustors, it is crucial to understand how the flame's heat-release source term varies with frequency. This thesis relies on experimentally measured FTFs to provide insight into how the flame responds to acoustic disturbances. In the following, the concept of FTFs is presented, and the underlying assumptions are explained first. After that, the Rankine-Hugoniot relations that connect the FTFs and the previously discussed transfer matrices are introduced.

### 2.3.1 Flame Transfer Functions

The FTF correlates flame heat release fluctuations $\dot{Q}'$ to the perturbations of acoustic velocity at the burner exit $u'_B$. Both quantities are normalized with their respective mean values $\bar{\dot{Q}}$ and $\bar{u}_B$, thus yielding the following equation:

$$FTF = \frac{\dot{Q}'/\bar{\dot{Q}}}{u'_B/\bar{u}_B}. \tag{2.34}$$

Assuming that the fluctuating quantities $u'_B$ and $\dot{Q}'$ undergo harmonic oscillations at a particular angular frequency $\omega$, they can be converted into the frequency domain. Both quantities can be expressed by their

complex-valued Fourier coefficients:

$$\dot{Q}'(\omega) = |\dot{Q}'|(\omega)e^{\left(i\omega t+\varphi_{\dot{Q}}\right)} \tag{2.35}$$

$$u'_B(\omega) = |u'_B|(\omega)e^{\left(i\omega t+\varphi_{u_B}\right)}. \tag{2.36}$$

This allows splitting up the FTF into its frequency-dependent amplitude and phase response, defined as:

$$\begin{aligned} |FTF|(\omega) &= \frac{|\dot{Q}'|/\bar{\dot{Q}}}{|u'_B|/\bar{u}_B} \\ \measuredangle FTF(\omega) &= \varphi_{\dot{Q}} - \varphi_{u_B}. \end{aligned} \tag{2.37}$$

For very low frequencies $\omega \to 0$, the FTF describes the quasi-steady flame response [71]. This is a characteristic feature that depends on the combustion configuration.

For perfectly premixed combustion, where the homogeneously premixed fuel-air mass flow is modulated, this describes a pure thermal power modulation. The heat release rate is varied proportionally to the velocity at the burner outlet with no phase shift:

$$\lim_{\omega\to 0} |FTF_{pp}| = 1 \tag{2.38}$$

$$\lim_{\omega\to 0} \measuredangle FTF_{pp} = 0. \tag{2.39}$$

In the case of technically premixed flames, equivalence ratio fluctuations additionally contribute to the FTFs as discussed in Section 1.1.2. In the following, it is shown that this contribution can also be expressed as a function of the burner outlet velocity fluctuation. Thus, the concept of FTFs is also applicable to technically premixed flames.

For low oscillation amplitudes, the overall heat release rate fluctuation $\dot{Q}'$ can be expressed as a linear superposition of the equivalence ratio contribution $G_\phi$ onto the FTF of a perfectly premixed flame [33, 81]:

$$\frac{\dot{Q}'}{\bar{\dot{Q}}} = FTF_{pp} \cdot \frac{u'_B}{\bar{u}_B} + G_\phi \cdot \frac{\phi'}{\bar{\phi}}. \tag{2.40}$$

If the pressure loss in the fuel injector is high compared to the oscillation amplitudes, the fuel supply can be considered acoustically stiff, which means that the fuel flow rate does not react to acoustic perturbations. In this case, the equivalence ratio fluctuations depend only on the air mass flow perturbations. Those are directly related to the acoustic velocity perturbations. Thus, both FTF contributions can be formulated as functions of $u'_B$:

$$\frac{\dot{Q}'}{\bar{\dot{Q}}} = FTF_{pp} \cdot \frac{u'_B}{\bar{u}_B} + FTF_{\phi} \cdot \frac{u'_B}{\bar{u}_B} \tag{2.41}$$

$$= FTF_{tp} \cdot \frac{u'_B}{\bar{u}_B}. \tag{2.42}$$

For determining the quasi-steady flame response of $\mathrm{FTF_{tp}}$, the equivalence ratio contribution $\mathrm{FTF}_{\phi}$ is considered first. Due to the acoustically stiff fuel supply, only the air mass flow is modulated. A positive acoustic velocity fluctuation causes a dilution of the mixture, and vice versa [12]. The equivalence ratio fluctuations are hence out of phase with respect to the velocity fluctuations by $\pi$:

$$\lim_{\omega \to 0} |FTF_{\phi}| = 1 \tag{2.43}$$

$$\lim_{\omega \to 0} \angle FTF_{\phi} = \pi. \tag{2.44}$$

The superposition of $\mathrm{FTF_{pp}}$ and $\mathrm{FTF}_{\phi}$ results in the following low frequency limits of $\mathrm{FTF_{tp}}$ [33]:

$$\lim_{\omega \to 0} |FTF_{tp}| = 0 \tag{2.45}$$

$$\lim_{\omega \to 0} \angle FTF_{tp} = \frac{\pi}{2}. \tag{2.46}$$

At $\omega = 0$, the phase value is not defined due to the vanishing amplitude.

For high frequencies, the FTF amplitude tends towards zero for any configuration due to the increasing axial dispersion of the flame response [33]:

$$\lim_{\omega \to \infty} |FTF| = 0. \tag{2.47}$$

### 2.3.2 Rankine-Hugoniot Relations

In the following, the FTF is expressed as a function of the acoustic state variables $p'$ and $u'$ upstream and downstream of the flame. This is achieved by making use of the Rankine-Hugoniot relations. This approach allows the extraction of the FTF from acoustic measurements only, without requiring a direct measurement of the oscillating heat release rate $\dot{Q}'$. As mentioned in Section 1.1.1, the frequency range under investigation has a much larger wavelength than the flame's axial expansion in longitudinal thermoacoustics. Consequently, the flame can be regarded as acoustically compact. As a result, the thickness of the flame can be disregarded, and it can be treated as a thin sheet that marks the boundary between the cold reactants (index c) and hot products (index h) in the reacting flow [14,40,72]. Integrating the conservation equations for mass (cf. Eq. 2.1) and momentum (cf. Eq. 2.2) across a control volume that includes the flame leads to:

$$\rho_h u_h - \rho_c u_c = 0 \tag{2.48}$$

$$p_h + \rho_h u_h^2 - p_c - \rho_c u_c^2 = 0. \tag{2.49}$$

Additionally, energy conservation is considered:

$$\rho_h u_h^2 \left( h_h + \frac{u_h^2}{2} \right) - \rho_c u_c^2 \left( h_c + \frac{u_c^2}{2} \right) - \dot{Q} = 0. \tag{2.50}$$

Here, $h$ denotes the specific enthalpy. Assuming a stationary, isentropic one-dimensional flow up- and downstream of the flame, the ideal gas law $\rho = RT/p$ applies and the specific enthalpy can be expressed as:

$$h = c_p T = \frac{\gamma}{\gamma - 1} \frac{p}{\rho}. \tag{2.51}$$

Herein, $\gamma$ denotes the specific heat ratio. Applying the definition of the Mach number, $Ma = u/c$ and inserting Equation 2.51, Equations 2.48-2.50 can be reformulated. The result are the Rankine-Hugoniot relations, which describe the jump conditions for velocity, pressure, and tempera-

ture across the flame [83]:

$$\frac{u_h}{u_c} = 1 + \frac{\gamma - 1}{\gamma} \frac{\dot{Q}}{p_c u_c} + \mathcal{O}\left(Ma^2\right) \tag{2.52}$$

$$\frac{p_h}{p_c} = 1 - (\gamma - 1) \frac{\dot{Q}}{p_c u_c} Ma_c^2 + \mathcal{O}\left(Ma^4\right) \tag{2.53}$$

$$\frac{T_h}{T_c} = \left(\frac{c_h}{c_c}\right)^2 = 1 + \frac{\gamma - 1}{\gamma} \frac{\dot{Q}}{p_c u_c} + \mathcal{O}\left(Ma^2\right). \tag{2.54}$$

$$\tag{2.55}$$

For low Mach numbers, as usually present in gas turbine combustors, higher order Mach number terms $\mathcal{O}(...)$ can be neglected. The total flow quantities in Equations 2.52-2.54 are decomposed into their respective mean and fluctuating components using Equations 2.4-2.6. Then, by retaining only first-order terms and linearizing the resulting expressions, two equations that establish a correlation between acoustic pressure and velocity fluctuations across the flame can be derived:

$$\frac{p'_h}{\bar{\rho}_h c_h} = \vartheta \frac{p'_c}{\bar{\rho}_c c_c} - \theta \vartheta Ma_c \left(1 + \frac{\dot{Q}'/\bar{\dot{Q}}}{u'_c/\bar{u}_c}\right) u'_c \tag{2.56}$$

$$u'_h = -\vartheta \gamma Ma_c u'_c \frac{p'_c}{\bar{\rho}_c c_c} + \left(1 + \frac{\dot{Q}'/\bar{\dot{Q}}}{u'_c/\bar{u}_c}\right) u'_c. \tag{2.57}$$

Herein, the specific impedance $\vartheta$ and the relative temperature rise $\theta$ are defined as:

$$\vartheta = \frac{\bar{\rho}_c c_c}{\bar{\rho}_h c_h} \tag{2.58}$$

$$\theta = \frac{T_h}{T_c} - 1. \tag{2.59}$$

Incorporating the FTF definition according to Equation 2.34 and representing Equations 2.56 and 2.57 in matrix-vector notation yields the acoustic transfer matrix of the flame in $pu$-notation, $\mathbf{FTM}^{pu}$:

$$\begin{bmatrix} \frac{p'}{\bar{\rho}c} \\ u' \end{bmatrix}_h = \underbrace{\begin{bmatrix} \vartheta & -\vartheta\theta Ma_c(1+FTF) \\ -\theta\gamma Ma_c & 1+\theta FTF \end{bmatrix}}_{\mathbf{FTM}^{pu}} \begin{bmatrix} \frac{p'}{\bar{\rho}c} \\ u' \end{bmatrix}_c \tag{2.60}$$

For very low Mach numbers, Equation 2.60 can be further simplified to:

$$\begin{bmatrix} \frac{p'}{\bar{\rho}c} \\ u' \end{bmatrix}_h = \underbrace{\begin{bmatrix} \vartheta & 0 \\ 0 & 1+\theta FTF \end{bmatrix}}_{\mathbf{FTM}^{pu}} \begin{bmatrix} \frac{p'}{\bar{\rho}c} \\ u' \end{bmatrix}_c . \tag{2.61}$$

This formulation serves as the basis for the experimental FTF determination as outlined in Section 4.2.2.

# 3 Experimental Setup

This chapter describes the experimental setup. All experiments were carried out on an atmospheric single burner test rig. The rig is described first. Second, the swirl burner used is described in detail. The chapter ends with the introduction of the operating range covered in the experiments described in Chapters 5 and 6.

## 3.1 Atmospheric Combustion Test Rig

Figure 3.1 presents a schematic of the test rig. The rig is an axial arrangement of plenum, combustor, and exhaust silencer with a swirl burner mounted at the combustor inlet. Combustion air is drawn from a compressed air supply header. It is filtered and regulated to maintain a pressure of approximately 10 bar. The air mass flow is electrically preheated to maintain a burner inlet temperature of $T_{pre}$=573 K. At the outlet of the preheater, natural gas can be introduced into the air flow if the test rig is operated in perfectly premixed natural gas configuration ($NG_{pp}$).

Via a 3-way valve, half of the heated mixture is then supplied directly to the plenum and the other half through a hot gas siren that serves for upstream acoustic excitation. The siren consists of a stator and a rotor disc with double sine-shaped orifices that generate a harmonic excitation signal. The rotor is driven by a 1.1 kW three-phase motor with a frequency converter to control the rotation speed. The rotation speed is monitored by a photo sensor, which is interrupted by a profiled disk mounted on the siren shaft. Effective excitation frequencies up to 800 Hz can be realized. A detailed description of the siren is given by Eckstein [27]. The pipes connecting the preheater and the plenum provide enough buffer

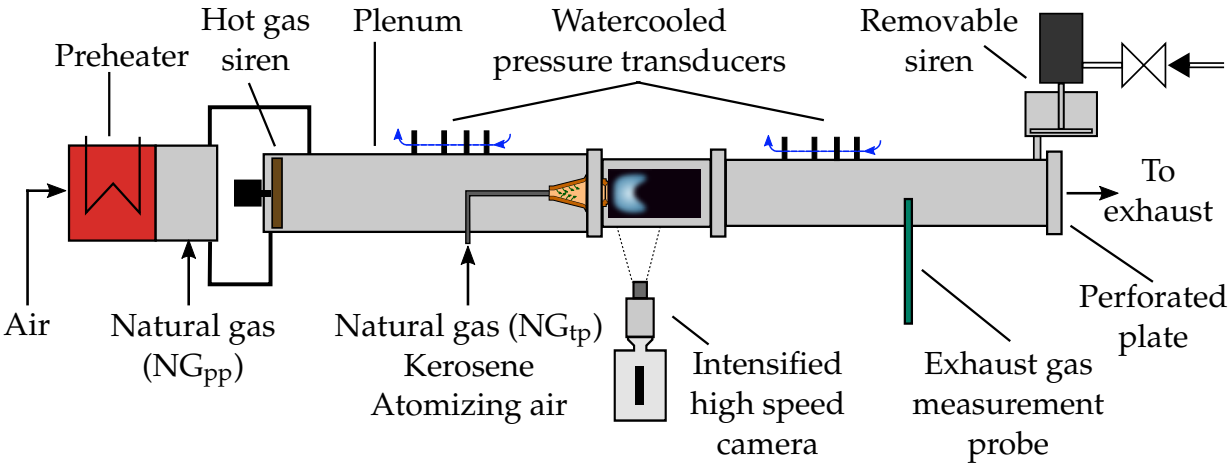


**Figure 3.1:** Schematic of the atmospheric single burner test rig. Adapted from Stadlmair [88].

volume for acoustically isolating the plenum from upstream infrastructure [25]. The plenum is a cylindrical tube with a length of 1727 mm and a diameter of 124 mm. It provides ports for pressure and temperature measurement. External insulation is provided to minimize the heat loss in the plenum. Kerosene, atomizing air, and natural gas for the technically premixed configuration ($NG_{tp}$) are supplied via an interface at the downstream end of the plenum. The combustion chamber has a rectangular section of 150 × 150 mm and a length of 730 mm. It provides optical access to the flame through a quartz glass window and ports for pressure and global $NO_x$ emission measurement. Impingement air cooling is provided on the combustor walls and the quartz glass window. Downstream of the measuring port section, a removable siren that serves as the second acoustic excitation source [47] can be attached. A perforated plate at the test rig outlet generates a lowly-reflecting acoustic boundary condition. More detailed descriptions of the test rig can be found in [87] and [6].

## 3.2 A$^2$EV Swirl Burner

The burner used in this study is a scaled-down version of the modular A$^2$EV swirl burner developed by Sangl [77] and Mayer [61]. The design

was derived from the Alstom AEV burner and optimized with respect to flame flashback safety and low $NO_x$ emissions across a wide range of operating conditions. Figure 3.2 depicts a schematic of the burner in the original gas burner configuration (a) and in the dual fuel burner configuration, which was developed in the present work (b).

The burner consists of a conical element with four tangential slots by which the air flow is swirled. In technically premixed natural gas operation, natural gas is fed directly into the swirler at each of the four trailing edges of the slots through ten evenly spaced holes. The apex of the conical element is cut off, and a head air port at the center axis allows part of the airflow to bypass the swirl slots. The conical mixing tube connected to the swirler regulates the swirl number by increasing the axial flow component due to the decrease in the cross-sectional area [77]. From a thermoacoustic perspective, this creates a convective time delay between the fluctuations of swirl and axial velocity at the burner exit [6]. The thermoacoustic importance of the time delays is discussed further in Section 4.3. The sudden area increase at the burner outlet induces a vortex breakdown. This leads to the formation of shear layers in the inner and outer recirculation zones as well as a flow stagnation point at the burner centerline, which serves for flame stabilization. The properties of the natural gas configuration have been studied by Bade [6].

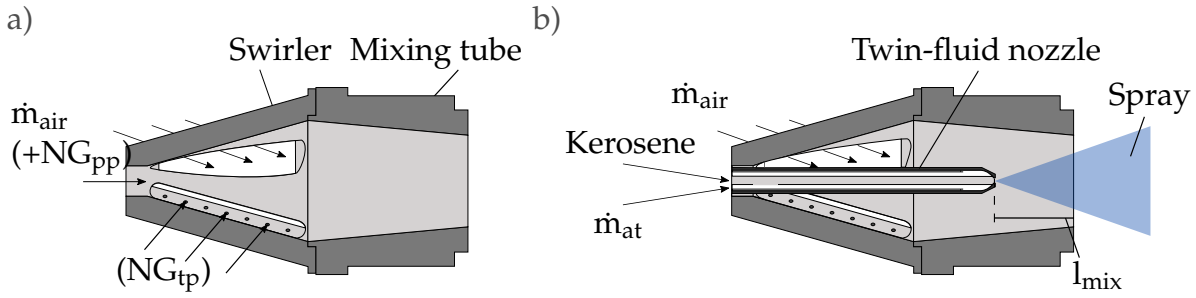


**Figure 3.2:** A²EV swirl burner in (a) gas burner configuration and (b) dual fuel burner configuration.

In order to allow liquid fuel combustion, the burner is retrofitted with a movable twin-fluid nozzle, which is mounted at the center axis at the head air port of the swirler [95] as shown in Figure 3.2 (b). The nozzle

is fed with kerosene and atomizing air, which are brought into contact at the nozzle exit, where the liquid flow is atomized by the high momentum air flow. The atomizing air is not preheated. To enhance the atomization quality, the atomizing air is swirled in the nozzle. The atomizing air swirl has the same direction as the main air. The spray cone has a narrow opening angle of 20°. In operation, the nozzle is choked at the exit.

In order to vary the degree of fuel-air premixing in the combustion chamber, the axial distance between the nozzle outlet and the combustor inlet can be changed. This distance is referred to as mixing length $l_{mix}$. Fuel-air premixing is affected by this in two ways: Firstly, a longer premixing distance leads to better turbulent mixing of fuel and air. Secondly, the spatial distribution of the fuel becomes more homogeneous. Because of the narrow spray cone opening angle, the spray is not distributed over the entire burner cross section when the nozzle exit is close to the combustor inlet, as indicated in the schematic in Figure 3.1. In contrast to that, the fuel is distributed over the entire cross section of the burner outlet if the nozzle is retracted far enough.

The insertion of the twin fluid nozzle blocks the head air port and thus changes the flow field. Due to the increased mass flow through the swirl slots, the swirl number of the flow increases. Furthermore, the axial momentum of the flow is reduced, and the recirculation zone moves towards the burner exit. In liquid operation, this is counteracted by the atomizing air flow. For natural gas combustion, the nozzle is removed in all experiments in this study. The impact of the nozzle on the acoustic properties of the burner is discussed in Section 6.1.

## 3.3 Operating Range

Experiments are conducted for four different burner configurations in total in order to stepwise increase the mixture preparation complexity. The $NG_{pp}$- and the $NG_{tp}$-configuration serve as reference as they have already been studied before [6]. For kerosene combustion, a highly pre-

mixed configuration with a mixing length of $l_{mix}$ = 70 mm ($k_{70}$) and a partially premixed configuration with a mixing length of $l_{mix}$ = 30 mm ($k_{30}$) are investigated.

The operating range is spanned by the systematic variation of equivalence ratio $\phi$ and main air mass flow $\dot{m}_{air}$ for all configurations. For the two liquid fuel configurations, the atomizing air mass flow $\dot{m}_{at}$ is a third variable that determines the operating point. The reference operating point is at $\dot{m}_{air}$ = 25 g/s and $\phi$ = 0.675. For the two liquid fueled configurations, the atomizing air mass flow is $\dot{m}_{at}$ = 0.875 g/s which is 3.5% of $\dot{m}_{air}$.

Three test series are carried out for both nozzle configurations, in each of which one parameter is varied separately. First, the main air mass flow is altered between $\dot{m}_{air}$ = 20 g/s and $\dot{m}_{air}$ = 30 g/s at constant equivalence ratio $\phi$ = 0.675. In liquid operation, the atomizing air mass flow is kept proportional to the main air mass flow at a constant ratio of $\dot{m}_{at}/\dot{m}_{air}$ = 3.5%. This aims to maintain the flow field self-similarity from the natural gas configurations [77] also for the cases with liquid fuel injection. This means that fuel, main air, and atomizing air mass flow are changed proportionally.

The second series of experiments comprises a variation of the equivalence ratio between $\phi$ = 0.575 and $\phi$ = 0.775 at a fixed main air mass flow of $\dot{m}_{air}$ = 25 g/s. Due to the prescribed coupling of $\dot{m}_{at}$ to $\dot{m}_{air}$, this means that the air-liquid-ratio at the liquid injection nozzle (ALR) is changed. As discussed in Section 5.1, this affects the liquid fuel atomization quality.

In order to separately investigate the influence of the atomization quality on the combustion dynamics for the liquid fuel configurations, the atomizing air mass flow is varied between $\dot{m}_{at}$ = 0.63 g/s and $\dot{m}_{at}$ = 1.13 g/s at a fixed equivalence ratio of $\phi$ = 0.675 and a fixed main air mass flow of $\dot{m}_{air}$ = 25 g/s.

Table 3.1 provides an overview of the reference operating point and the three test series for natural gas and kerosene. Except for the atomizing air variation, the operating parameters of each test series are listed in

two rows. The first row denotes the parameters for natural gas, and the second row for kerosene. Parameters that remain unchanged between the two configurations are written centered. The atomizing air is only varied in kerosene operation. Due to the different stoichiometric air requirement of the two fuel types, the fuel mass flow rates differ. The resulting thermal power is almost equal between the two fuels.

| Varied parameter | $\dot{m}_{air}$ $(g/s)$ | $\dot{m}_{NG}$ $(g/s)$ | $\dot{m}_{kero}$ $(g/s)$ | $\dot{m}_{at}$ $(g/s)$ | $P_{th}$ $(kW)$ | $\phi$ |
|---|---|---|---|---|---|---|
| Reference | 25 | 1.03 | 1.19 | 0.875 | 51<br>51 | 0.675 |
| $\dot{m}_{air}$ | 20 – 30 | 0.83 – 1.24 | 0.95 – 1.43 | 0.70 – 1.05 | 41 – 61<br>41 – 62 | 0.675 |
| $\phi$ | 25 | 0.88 – 1.19 | 1.00 – 1.35 | 0.875 | 43 – 58<br>43 – 58 | 0.575 – 0.775 |
| $\dot{m}_{at}$ | 25 | | 1.19 | 0.63 – 1.13 | 51 | 0.675 |

**Table 3.1:** Overview of the operating parameters in the reference operation point and for systematic variations of air mass flow, equivalence ratio, and atomizing air mass flow.

# 4 Diagnostics and Methodology

This chapter provides information about the diagnostics used and the applied methods. The chapter starts with a brief description of the stationary characterization. Particular focus is set on the dynamic flame behavior. The experimental determination of flame transfer matrices and flame transfer functions is outlined in Section 4.2. Finally, the approach for the analytical FTF modeling is described, and the relevant feedback mechanisms are discussed in Section 4.3.

## 4.1 Stationary Flame Characterization

### 4.1.1 Flame Imaging

Flame images are acquired using a *Photron FastCam SAX-2* high-speed camera equipped with a *Hamamatsu C10880* image intensifier. A bandpass filter with a center wavelength of 307±5 nm is installed in front of the intensifier in order to record only the OH*-chemiluminescence radiation. For each operating point, sets of 1000 images are recorded with a frame rate of 125 images per second and averaged in *MATLAB* to remove the influence of turbulent fluctuations. The correction with a calibration image of a reference target allows to remove the distortion of the images and scale the length. To facilitate the comparison of flame positions and flame shapes across different operating points, the OH*-chemiluminescence intensity values are scaled between 0 and 1 by normalizing with the individual maximum. The stationary flame geometry parameters are then calculated based on the normalized line-of-sight OH*-chemiluminescence intensity $I_{ij}$ as visualized in Figure 4.1:

- The flame center of gravity $x_{cg}$ is defined as follows:

$$x_{cg} = \frac{\sum_{i=1}^{x_{max}} \left( x_i \sum_{j=1}^{y_{max}} I_{ij} \right)}{\sum_{i=1}^{x_{max}} \sum_{j=1}^{y_{max}} I_{ij}}. \tag{4.1}$$

- In accordance with the previous works of Bade [6] and Stadlmair [88], the axial extension of the flame $l_{fl}$ is defined as the axial distance between the first and the last column where at least 5 pixels exceed a relative intensity of 18%.
- Similarly, the flame width $d_{fl}$ is determined by the vertical distance of the upper and lower row, where at least 5 pixels exceed the threshold value. Since the flame may extend close to the combustor walls, the intensity gradient at the radial boundaries is very steep. The threshold is therefore set to 50% to guarantee reliable width detection.

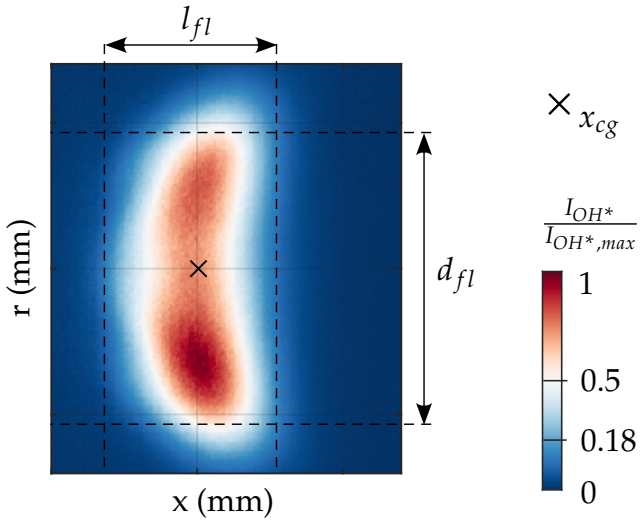


**Figure 4.1:** Determination of the flame geometry parameters from OH*-chemiluminescence images.

### 4.1.2 Droplet Sizing

For the droplet size measurements, the burner is installed outside of the test rig and operated without main air. The liquid fuel is replaced by a

mixture of 90% ethanol and 10% water, which provides similar atomization characteristics to kerosene [27]. The droplet spectrum is determined through optical measurements based on Mie scattering using a *Spraytec MALVERN Particle Sizer* 200 mm downstream of the nozzle exit on the central axis. Measurement data are acquired at a recording rate of 2500 Hz over a period of 1 second to obtain a statistically sufficient number of particles. The Sauter mean diameter (SMD) is chosen to describe the spray's size distribution by one representative value. The SMD represents the average volume-to-surface ratio of the droplets in the spray, which dominates heat and mass transfer phenomena [50]. For a control volume of N spherical droplets with the respective diameters $d_n$, it is defined as follows:

$$SMD = \frac{\sum_{n=1}^{N} N_n d_n^3}{\sum_{n=1}^{N} N_n d_n^2}. \tag{4.2}$$

### 4.1.3 $NO_x$ Measurement

The exhaust gas measurement port is located at a distance of 540 mm downstream of the burner exit. A water thermostat is used to keep the temperature in the exhaust gas at 353 K. This is necessary to quench the reaction and protect the exhaust probe in the hot gas from overheating. The extracted gas is fed to an *ECOphysics CLD700ELht* $NO_x$ analyzer. The hose that conveys the exhaust gases to the analyzer is temperature controlled to prevent water condensation. This is necessary because $NO_x$ species have good solubility in liquid water, and condensation would therefore falsify the measurement result. Time series of 20 s each are recorded at a sampling rate of 2 Hz and averaged to eliminate fluctuations of the measured values. In order to compare the measured values with each other, all concentrations are normalized to 15% $O_2$ in the dry exhaust gas.

## 4.2 Acoustic Characterization of Burner and Flame

The acoustic properties of the burner and the flame are characterized based on dynamic pressure measurements. For this, the test rig is equipped with in total eight water-cooled *PCB 106B* piezoelectric dynamic pressure transducers, four of which are located in the plenum and the other four in the combustion chamber. Dynamic pressure is recorded at a sample rate of 65536 samples per second. Time traces of 10 seconds are recorded for each excitation frequency in the range between 20 Hz and 800 Hz at a frequency stepping of 20 Hz. The recorded data is correlated to the excitation signal in the postprocessing to extract the amplitude and phase information of the dynamic pressure signal, which serve as input for the acoustic field reconstruction.

In the following, the calculation of acoustic scattering matrices using the multi-microphone method is described. The resulting scattering matrices are then employed as input for the FTF determination, which is described subsequently.

### 4.2.1 Determination of Scattering Matrices

The determination of scattering matrices from the acoustic measurements is schematically shown in Figure 4.2.

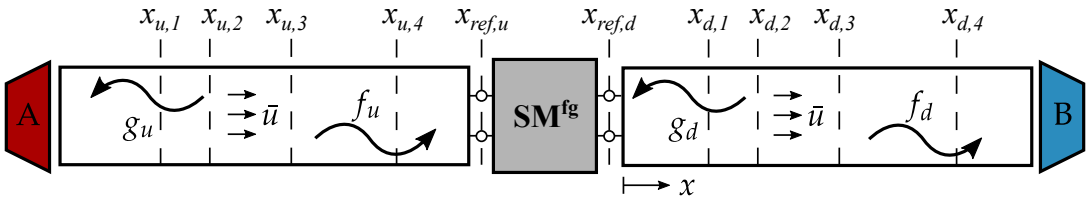


**Figure 4.2:** Experimental determination of scattering matrices. Adapted from Stadlmair [88].

The frequency-dependent acoustic scattering matrices of the burner with and without flame can be determined experimentally by imposing a known acoustic excitation state on one side of the element and measur-

ing its response on the other. In order to determine the four elements of the scattering matrix from two acoustic state variables, two independent excitation states are required. This can be achieved using the two-source location method in which two acoustic forcing conditions are imposed on the system by separately using the two acoustic sources upstream (A) and downstream (B) of the element [62]. From the dynamic pressure measurements at multiple discrete positions upstream and downstream, the analytical solution of the convective wave equation 2.23 and 2.24 can then be used to obtain the Riemann-invariants f and g. The minimum required number of microphones for this procedure is two on each side. The procedure is then referred to as two-microphone method [1]. If the distance between the two measurement points is equal to half of the acoustic wavelength, this method leads to the occurrence of singularities [2]. This problem can be overcome by the multi-microphone method (MMM), which uses more than two non-equidistantly spaced microphones on both sides [32,67,80]. The determination of the Riemann invariants according to Equations 2.23 and 2.24 thus becomes an optimization problem that can be reformulated to be solved by a least square method:

$$\begin{bmatrix} f^A_{u/d}(\omega) & f^B_{u/d}(\omega) \\ g^A_{u/d}(\omega) & g^B_{u/d}(\omega) \end{bmatrix} = \mathbf{H}^{\dagger}_{u/d}\mathbf{p}'_{u/d}. \tag{4.3}$$

$\mathbf{p}'_{u/d}$ denotes the spectral pressure amplitude of the acoustic pressure signal $p'(x,t)$ at the discrete measurement locations upstream and downstream, evaluated for the respective forcing frequency $f = \omega/2\pi$ for both forcing conditions A and B:

$$\mathbf{p}'_{u/d} = \begin{bmatrix} p'^A\left(x_{u/d,1} - x_{ref,u/d}, \omega\right) & p'^B\left(x_{u/d,1} - x_{ref,u/d}, \omega\right) \\ \vdots & \vdots \\ p'^A\left(x_{u/d,N} - x_{ref,u/d}, \omega\right) & p'^B\left(x_{u/d,N} - x_{ref,u/d}, \omega\right) \end{bmatrix}. \tag{4.4}$$

The reference coordinates $x_{ref,u/d}$ are the up- and downstream boundaries of the element under consideration, respectively. The matrix $\mathbf{H_{u/d}}$ contains the spatial field information, given by the convective wave numbers

$k^{\pm}$ and corresponding measurement locations $x_{u/d}$:

$$\mathbf{H}_{u/d} = \begin{bmatrix} e^{\left(-ik^{+}x_{u/d,1}-x_{ref,u/d}\right)} & e^{\left(ik^{-}x_{u/d,1}-x_{ref,u/d}\right)} \\ \vdots & \vdots \\ e^{\left(-ik^{+}x_{u/d,N}-x_{ref,u/d}\right)} & e^{\left(ik^{-}x_{u/d,N}-x_{ref,u/d}\right)} \end{bmatrix}. \tag{4.5}$$

$\mathbf{H}^{\dagger}$ represents the pseudo-inverse of $\mathbf{H}$, defined as:

$$\mathbf{H}^{\dagger} = \left(\mathbf{H}^{\top} \cdot \mathbf{H}\right)^{-1} \cdot \mathbf{H}^{\top}. \tag{4.6}$$

Finally, the scattering matrix can be obtained from the reconstructed f and g by rearranging Equation 2.32:

$$\underbrace{\begin{bmatrix} T^{+} & R^{-} \\ R^{+} & T^{-} \end{bmatrix}}_{\mathbf{SM^{fg}}} = \begin{bmatrix} f_d^A & f_d^B \\ g_u^A & g_u^B \end{bmatrix} \begin{bmatrix} f_u^A & f_u^B \\ g_d^A & g_d^B \end{bmatrix}^{-1}. \tag{4.7}$$

### 4.2.2 Measurement of Flame Transfer Functions

The FTF can be determined from purely acoustic measurements by applying the MMM and exploiting the relationship between the flame transfer matrix and the FTF via the Rankine Hugoniot relations as outlined in Section 2.3.2. Equation 2.61 can be solved for the FTF to:

$$FTF = \frac{FTM_{22}^{pu} - 1}{\theta} = \frac{FTM_{22}^{pu} - 1}{T_h/T_c - 1}, \tag{4.8}$$

with $T_c$ and $T_h$ being the local temperature just up- and downstream of the flame, respectively.

The direct experimental determination of the flame transfer matrix **FTM** is not possible since measurements with flame always also include the acoustic influence of the burner. However, this contribution can be eliminated in the evaluation procedure.

It is presumed that the acoustic qualities of both the burner and flame are linearly superposed. Based on this assumption, the exclusive flame transfer matrix can be expressed by the combined burner-flame transfer matrix (**BFTM**) and the matrix of the burner without flame (**BTM**) as follows [80]:

$$\mathbf{FTM} = \mathbf{BFTM} \cdot \mathbf{BTM}^{-1}. \tag{4.9}$$

The **BFTM** and the **BTM** can be determined separately from acoustic measurements with and without combustion and the procedure described in Section 4.2.1. The underlying assumption that the acoustic properties of the burner remain unaffected by the presence of the flame has been confirmed in several works in the past [5, 80].

For perfectly premixed flames, the equivalence ratio is locally constant. Thus, the normalized heat release fluctuations $\dot{Q}'/\bar{\dot{Q}}$ can be assumed proportional to the normalized integral OH*-chemiluminescence intensity $I'_{OH^*}/\bar{I}_{OH^*}$. Consequently, Equation 2.34 can be expressed as:

$$FTF = \frac{I'_{OH^*}/\bar{I}_{OH^*}}{u'_B/\bar{u}_B}. \tag{4.10}$$

The integral OH*-chemiluminescence intensity $I_{OH^*}$ can be measured using a photomultiplier. The velocity perturbations at the burner outlet can be obtained from acoustic pressure measurements in the plenum and the burner transfer matrix. More information on the method can be found in [88] and [6].

In the present work, the purely acoustic method based on the Rankine Hugoniot relations is applied, because it is suitable for all combustion configurations. In addition, for the $NG_{pp}$-configuration, the OH*-chemiluminescence-based method is applied in parallel to cross-validate the measurements. The comparison of both results can be found in Appendix A.2.

## 4.3 Analytical FTF Modeling

In addition to the qualitative explanation of the feedback mechanisms presented in Section 1.1.2, reliable methods for modeling the flame response are of significant importance. The modeling serves two purposes:

- First, replicating measured FTFs of existing systems allows for a deeper understanding of the physical processes that drive the combustion dynamics.
- Second, the prediction of FTFs allows to prevent potential instabilities during the development of new systems.

The analytical FTF model discussed in the following is applied for both purposes, as presented in Chapter 7. The model represents various mechanisms by which acoustic excitation can lead to heat release fluctuations, each based on physically-based fit functions. In the following, the different mechanisms are briefly described, and modeling approaches for the individual terms are given.

Two main coupling mechanisms for perfectly premixed, swirl-stabilized combustion have been identified: mass flow fluctuations and swirl fluctuations [38]. In the case of technical premixing, equivalence ratio fluctuations provide a third mechanism that contributes to the flame response. For low excitation amplitudes, these three mechanisms can be linearly superposed. The analytical FTF model for technically premixed combustion thus results from the summation of these three terms:

$$FTF = FTF_M + FTF_S + FTF_\phi. \tag{4.11}$$

The indices M, S, and $\phi$ represent the contribution of mass flow, swirl, and equivalence ratio fluctuations, respectively.

A common property of all three mechanisms is that the respective disturbance is convectively transported from its origin to the flame, where it causes heat release fluctuations. Each of the three model terms, therefore,

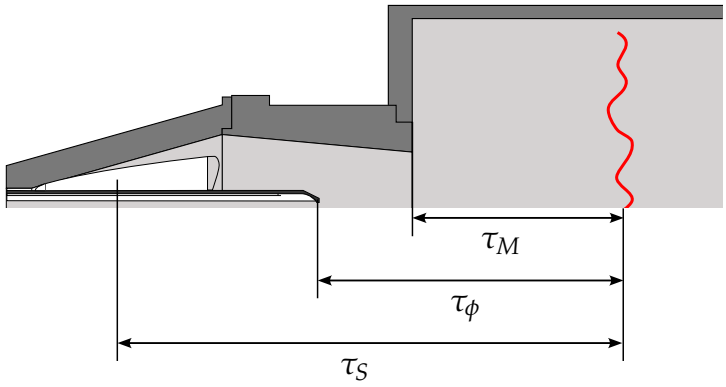


**Figure 4.3:** Visualisation of the different length scales associated with the convective transport of mass flow fluctuations, swirl fluctuations, and equivalence ratio fluctuations.

contains time delay elements of the type $e^{-i\omega\tau}$, where $\tau$ represents a convective time delay [18]. As indicated in Figure 4.3, the three mechanisms are triggered at different positions along the flow path and are thus associated with different convective time scales $\tau_M$, $\tau_S$ and $\tau_\phi$. This leads to a varying phase relation, causing the mechanisms to constructively or destructively interfere, depending on the respective time delay difference and frequency.

### 4.3.1 Mass Flow Fluctuations

Modulations of the mass flow can directly trigger heat release rate fluctuations. The mechanism was first investigated for perfectly premixed laminar gas flames [22, 24, 84], where the observed heat release fluctuations could directly be related to fluctuations of the flame surface. It was found that the mechanism is predominantly significant at low frequencies. For turbulent flames, local flame speed fluctuations must be taken into account. Schuermans et al. [81] proposed the $\tau - \sigma$ model, which describes the heat release rate fluctuations by a time delay $\tau$ and a standard deviation $\sigma$ to account for the spatially distributed heat release in the

flame:

$$FTF_{\tau-\sigma}(\omega) = e^{-i\omega\tau-\frac{1}{2}\omega^2\sigma^2}. \tag{4.12}$$

The model FTF is characterized by a linear phase and an amplitude decreasing from one to zero with increasing frequencies at a rate that is determined by the standard deviation $\sigma$. The model cannot reproduce amplitude values exceeding unity. To overcome this limitation, Alemela extended the model by a prefactor $n$, called interaction index [5]. However, this so-called $n-\tau-\sigma$ model violates the low frequency limits discussed in Section 2.3.1. Another approach was proposed by Freitag, who combined the time delay element with a second order delay element [33]:

$$FTF_M(\omega) = \frac{e^{-i\omega\tau_M}}{1+\alpha_{M1}i\omega+(\alpha_{M2}i\omega)^2}. \tag{4.13}$$

The model has a low frequency limit amplitude of one, thus fulfilling the required low frequency limit. Depending on the two damping parameters $\alpha_{M1}$ and $\alpha_{M2}$, the amplitude may first rise to a limit amplitude higher than one. For higher frequencies, the amplitude decays and approaches zero for high frequencies. The disadvantage of this model is the limited physical significance of the model variables. Especially the $\tau_M$ value cannot be directly interpreted as the time delay since the phase slope deviates from the linear form due to the combination with the second order delay term. In the present work, the approach proposed by Freitag is used to describe the contribution of mass flow fluctuations to the FTF.

### 4.3.2 Swirl Fluctuations

Hirsch et al. [37] have shown that swirl burners generate a time-delayed circulation fluctuation, which causes additional axial velocity fluctuations and consequently leads to the generation of heat release rate fluctuations. The mechanism can be explained based on the effect of vortex breakdown, which in swirl burners is responsible for the formation of the internal recirculation zone and, thus, for the aerodynamic stabilization of

the flame. While the circulation fluctuations are convectively transported along the cone-shaped reaction zone, they generate fluctuations in the azimuthal vorticity. According to the Biot-Savart law, these fluctuations induce axial velocity fluctuations at the flame front, which in turn cause heat release fluctuations. The analytical model proposed by Hirsch et al. is capable of predicting the swirl fluctuation-related FTF contribution entirely based on physical mechanisms. However, this requires a very detailed description of the flame parameters.

An alternative model was proposed by Komarek and Polifke [45]. They numerically applied a unit impulse of the tangential velocity to a swirl-stabilized flame and analyzed the flame response. They showed that the resulting heat release rate is first increased and subsequently decreased by the impulse. Since the overall heat release rate remains unaffected, the positive and the negative contribution are necessarily of the same intensity. In the FTF model, the increase and decrease of the heat release are approximated by two distributed time delay terms with opposite signs:

$$FTF_S = n_S \cdot \left( e^{-i\omega\tau_{S1} - \frac{1}{2}\omega^2\sigma_S^2} - e^{-i\omega\tau_{S2} - \frac{1}{2}\omega^2\sigma_S^2} \right). \tag{4.14}$$

The vorticity increases with the radial position, and therefore the magnitude of the mechanism depends on the flame diameter. This is represented by the interaction index $n_S$. Based on the observation that the heat release rate increases first, the time delay $\tau_{S1}$, which is associated with the positive heat release fluctuation, must be smaller than $\tau_{S2}$. The normal distribution $\sigma_S$ must have the same value for both terms in order to fulfill the requirement that the integral heat release rate fluctuation is zero. Hauser [36] compared the models of Hirsch et al. and Komarek and Polifke and showed that both models yield identical results. In the present work, the simple model of Komarek and Polifke is applied because it requires no a-priori modeling of the physical flame parameters.

### 4.3.3 Equivalence Ratio Fluctuations

Equivalence ratio fluctuations are generated at the fuel injection location. Fluctuations of the acoustic field cause air and fuel mass flow oscillations, thus modulating the equivalence ratio. After their generation, the equivalence ratio fluctuations are convectively transported to the reaction zone, where they induce heat release fluctuations.

A simple model to describe the impact of equivalence ratio fluctuations was presented by Lieuwen [52]. The model is focused on the convective transport, which is represented by a pure time delay with no amplitude modification. Any dispersive or diffusive effects are neglected. Sattelmayer developed a model that includes dispersive effects [78]. An estimate of the time delay distribution is obtained by investigating the velocity field. Schuermans et al. proposed to model the equivalence ratio contribution as a distributed time delay using a Gaussian distribution [81]:

$$FTF_\phi = -n_\phi e^{-i\omega\tau_\phi - \frac{1}{2}\omega^2\sigma_\phi^2}. \tag{4.15}$$

This model is applied in the present study. To satisfy the low frequency limit of technically premixed FTFs, the interaction index $n_\phi$ must be one and is therefore omitted in the following. In contrast to the other model terms, the value of $\tau_\phi$ corresponds directly to the convective time delay of the equivalence ratio fluctuations.

Bade [6] experimentally isolated the equivalence ratio fluctuation term by comparing flame transfer functions of perfectly and technically premixed natural gas combustion using the same burner hardware as in the present study. She showed that the equivalence ratio fluctuations predominantly affect the FTF at low frequencies and that the distributed time delay model can reproduce her experimental results. This was confirmed by Vogel et al. [96], who directly measured the equivalence ratio fluctuations in the flame for kerosene and natural gas combustion using an optical method and determined the numeric values of $\tau_\phi$ and $\sigma_\phi$ for different operating conditions. They pointed out that $\tau_\phi$ severely depends

on the fuel type. While natural gas can be considered to adapt to the local flow field initially after injection, the droplets need a non-negligible timespan to accelerate to the local flow velocity due to their inertia. The inertia and thus the acceleration time scale with the droplet diameter. The additional time delay significantly affects the dynamic properties of the flame, as discussed in Section 7.2.

# 5 Stationary Properties

In this chapter, the stationary properties throughout the operating range defined in Section 3.3 are presented and discussed. The focus is on the two liquid fuel configurations $k_{70}$ and $k_{30}$, while the two natural gas configurations serve as references. First, the atomizer performance for the liquid operation is discussed. $NO_x$ measurements are used to determine the degree of premixing that results from the measured droplet size spectrum for the two kerosene configurations. Emission measurements for the two natural gas configurations serve as reference. After this, the flame shapes for all configurations are discussed based on OH*-chemiluminescence images.

## 5.1 Atomizer Performance

This section addresses the mean droplet sizes of the liquid fuel spray. Analyzing the measured droplet diameters allows for drawing conclusions about the associated evaporation times. This, in turn, determines the level of fuel-air premixing that can be anticipated for the two different nozzle positions studied. Furthermore, conclusions can be drawn about the frequency range of possible interaction between the droplets and the acoustic field in the excited operation discussed in Chapter 6.

As discussed in Section 4.1.2, the experiments were conducted with a fuel substitute and in the absence of main air. The parameter variations of the test series according to the operating range definition from Table 3.1 are therefore also limited to $\dot{m}_{liq}$ and $\dot{m}_{at}$. However, in order to establish the connection between the droplet size measurements and the subsequent combustion experiments, the results are plotted against the correspond-

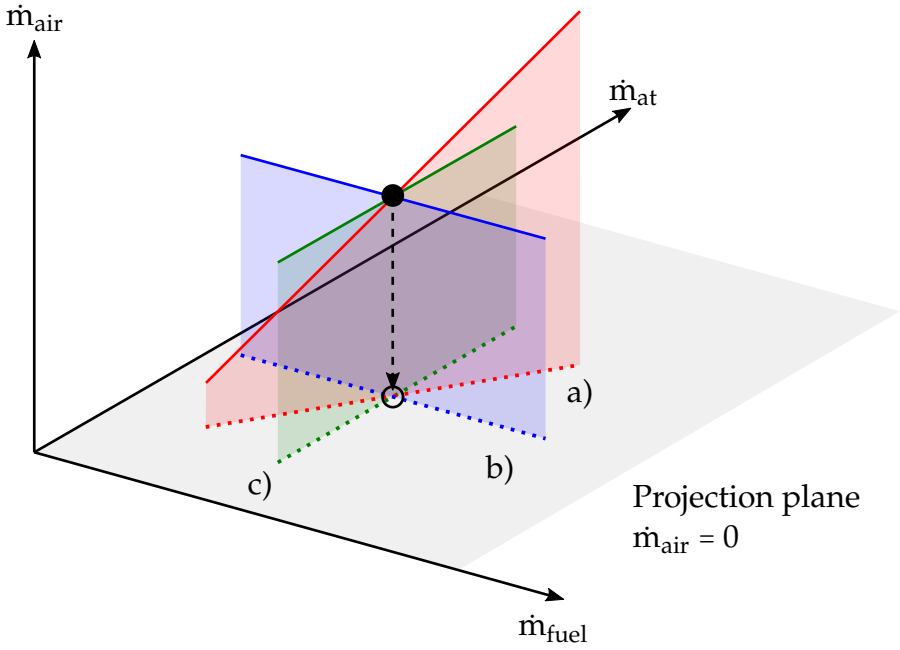


**Figure 5.1:** Qualitative visualization of the parametric variations for the original operation range (straight lines) and projected parametric variations for the SMD measurements in the absence of main air (dotted lines): (a): Variation of $\dot{m}_{at}$ and $\dot{m}_{fuel}$ at constant ratio representing the air mass flow variation, (b): Variation of $\dot{m}_{fuel}$ at constant $\dot{m}_{at}$ representing the equivalence ratio variation and (c): Variation of $\dot{m}_{at}$ at constant $\dot{m}_{fuel}$ representing the atomizing air variation.

ing variation parameters $\dot{m}_{air}$, $\phi$, and $\dot{m}_{at}$ from Table 3.1 in the following. This is illustrated in Figure 5.1.

The resulting SMD values for the three modified variation sets representing the sensitivities towards $\dot{m}_{air}$, $\phi$ and $\dot{m}_{at}$ are plotted in Figure 5.2. At the reference operating point defined in Section 3.3, the SMD equals 18.5 $\mu m$. The time required for a droplet to evaporate completely depends on its initial diameter and the local flow conditions and can be estimated using the $D^2$ law [50]. For the given conditions, the evaporation time calculates to $\tau_{evap}$ = 1.15 ms, which is well beyond the convective time delay between injection and burner outlet for the $k_{70}$-configuration $\tau_{IB,k70}$ = 3.11 ms calculated by Vogel et al. [96]. Therefore, it can be concluded

that the spray is fully evaporated at the burner outlet. This assumption is further confirmed in Section 5.2. The calculation of the evaporation time is provided in Appendix A.1.

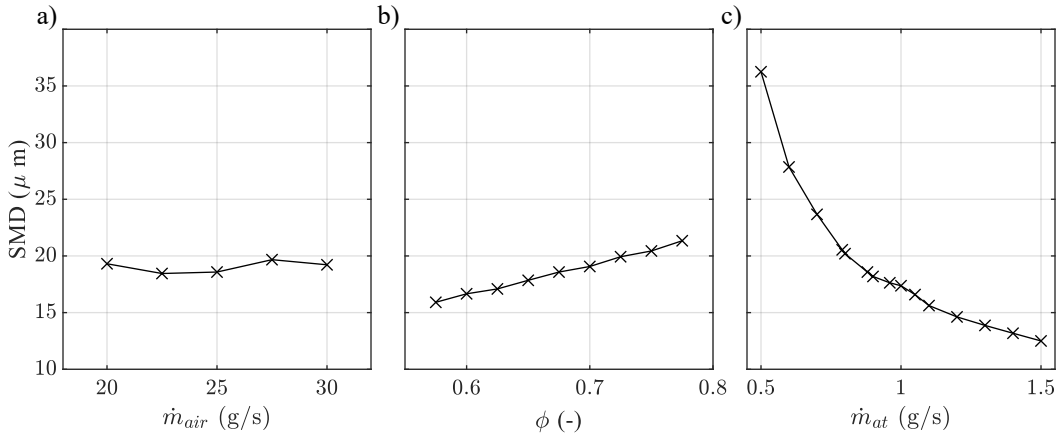


**Figure 5.2:** Measured SMD of the fuel substitute spray for (a) different liquid and atomizing air mass flows at constant ratio $\dot{m}_{liq}/\dot{m}_{at}$ = 1.36 over the corresponding air mass flow according to the operating range definition (cf. Table 3.1), (b) different liquid mass flows at constant atomizing air mass flow $\dot{m}_{at}$ = 0.875 g/s over the corresponding equivalence ratio according to the operating range definition (cf. Table 3.1), and (c) different atomizing air mass flows at constant liquid mass flow $\dot{m}_{liq}$ = 1.19 g/s.

Figure 5.2 (a) shows the SMD for a proportional variation of liquid and atomizing air mass flow, plotted over the corresponding main air mass flow according to the operation range definition from Table 3.1. The ALR remains constant. According to Lefebvre [50], the transfer of the atomizing air's kinetic energy to the droplets' surface energy dominates the atomization in air-assisted atomizers. If the nozzle was run under sub-critical conditions, i.e., the flow velocity at the nozzle exit was below the local speed of sound, the atomizer air velocity would have an impact on the SMD. However, this is not observed here, thus confirming the assumption that the nozzle is choked in operation. Due to the critical flow in the nozzle, the atomizer air velocity remains constant. The energy transfer

between the atomizing air and liquid flow, and hence the droplet size, is thus mainly determined by the mass flow ratio between the two [50]. This is inversely proportional to the ALR and constant in this case.

Figure 5.2 (b) displays the SMD for a variation of the liquid mass flow at constant atomizing air mass flow, representing an equivalence ratio variation according to the operating range defined in Table 3.1. In this case, the ALR is inversely proportional to $\phi$. The SMD scales linearly with the liquid mass flow and is hence, as expected, inversely proportional to the ALR.

The effect of the atomizing air on the SMD is shown in Figure 5.2 (c). The ALR is proportional to $\dot{m}_{at}$ in this case. As expected, the SMD scales inversely with $\dot{m}_{at}$. It can thus be concluded that the nozzle is choked for all operating conditions investigated in this study.

## 5.2 $NO_x$ Emissions

The $NO_x$ emissions in the exhaust gas are used to evaluate the quality of fuel-air mixing. $NO_x$ measurements for perfectly premixed natural gas combustion serve as reference. Since $NO_x$ emissions scale nonlinearly with the combustion temperature and, thus, with the local equivalence ratio, local mixture inhomogeneities lead to increased global $NO_x$ emissions in the exhaust gas [93]. Therefore, increased $NO_x$ emissions at a constant equivalence ratio indicate a poor degree of premixing and vice versa. Note that, because of the difference in chemical composition, the $NO_x$ values for kerosene are slightly higher than those for an identically premixed natural gas case [49].

Figure 5.3 (a) shows the $NO_x$ emissions over $\dot{m}_{air}$ at constant equivalence ratio for the four different configurations. The lowest emissions are observed for the natural gas cases, with no discernible difference between the perfectly and technically premixed configuration. This is in line with the findings of Mayer [61], who investigated the full-scale $A^2EV$

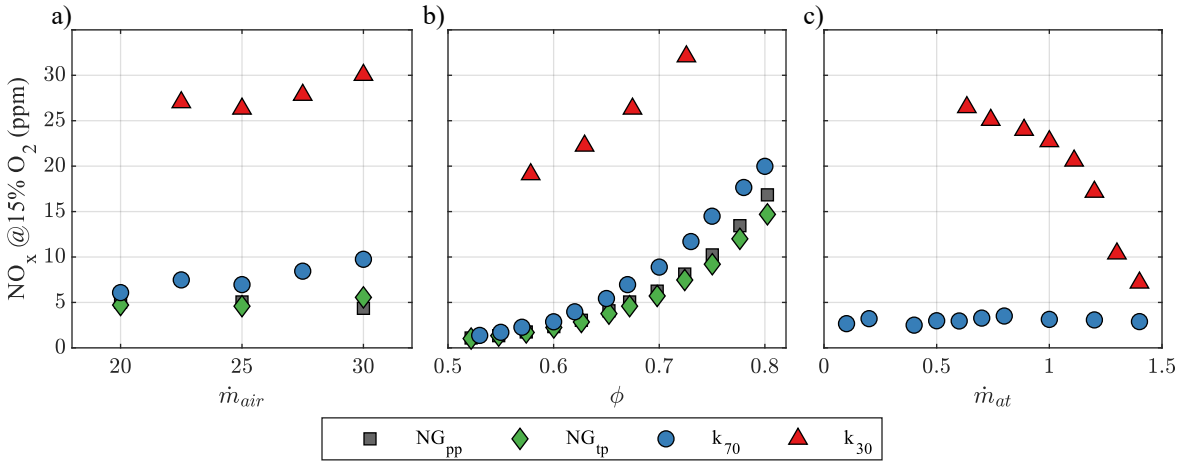


**Figure 5.3:** Measured $NO_x$ emissions for (a) different air mass flows at constant equivalence ratio, (b) different equivalence ratios at constant air mass flow, and (c) different atomizing air mass flows at constant equivalence ratio and constant air mass flow of the $NG_{pp}$-, $NG_{tp}$-, $k_{70}$- and $k_{30}$-configuration.

burner and only found differences in $NO_x$ emissions between the two natural gas configurations for near-stochiometric conditions. For the $k_{70}$-configuration, the $NO_x$ emissions are slightly higher but still very close to the natural gas levels. Considering that the $NO_x$ emissions are always higher for kerosene than for natural gas at the same degree of premixing, this indicates a very good premixing of kerosene and air. This supports the hypothesis from Section 5.1 that the fuel is completely evaporated at the burner outlet. The emissions in the $k_{30}$ case are higher than in the corresponding $k_{70}$ case by a factor of 5. This indicates the presence of mixture inhomogeneities and, thus, a more diffusive combustion character caused by the reduced premixing length.

The main air mass flow does not impact the emissions in any of the four cases. The $NO_x$ emissions show an exponential dependence on the equivalence ratio in all four cases, as visible in Figure 5.3 (b). Again, emissions are very similar for the two natural gas cases and the $k_{70}$-configuration, whereas emissions for the $k_{30}$-configuration are notably higher.

Figure 5.3 (c) shows the impact of atomizing air on $NO_x$ emissions for the two liquid cases. For the $k_{70}$-configuration, the emissions remain constant across the entire range. The fact that the $NO_x$ emissions remain constant even though, as previously discussed, the SMD changes indicates that the mixture quality in the flame is not controlled by the atomization quality at the nozzle outlet but by turbulent mixing in the mixing tube. The axial distance between the nozzle outlet and the flame is sufficiently long for this process to be completed regardless of the initial droplet diameter. In contrast to that, for the $k_{30}$-configuration, the $NO_x$ emissions show a strong dependency on the atomizing air mass flow. This indicates that the mixing process is not completed in the flame. $NO_x$ emission values for atomizing air mass flows below $\dot{m}_{at} = 0.6$ g/s are not plotted because no complete combustion could be achieved due to the insufficient atomization quality.

## 5.3 Flame Geometry

This section analyzes the stationary flame geometry. As discussed in Section 4.1.1, line of sight integrated OH*-chemiluminescence images are used for this purpose. First, flame shape and position at the reference operating point are compared across the four different configurations. After this, the flame shape sensitivity towards main air mass flow and equivalence ratio is discussed. Finally, the impact of the atomizing air mass flow on the flame shape is assessed for the two liquid fuel cases.

Figure 5.4 shows the OH*-chemiluminescence flame images of the four configurations at the reference operating point. The 50%-isocontour is added as a dashed black line to all images. The two left images depict the flames for natural gas combustion in perfectly and technically premixed configuration. The two images on the right side show liquid fuel combustion for the $k_{70}$- and $k_{30}$-configuration.

The natural gas flames are almost identical, with a disc-like shape characterized by a moderate radial and low axial extension. The intensity peak

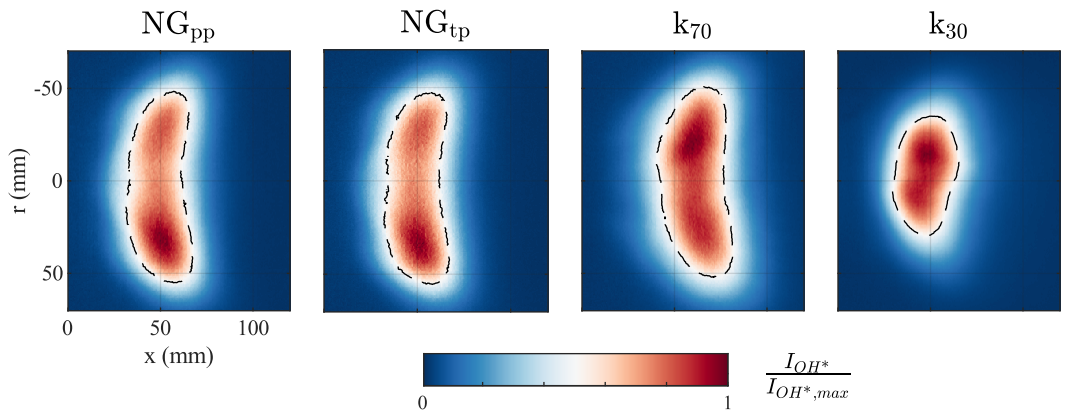


**Figure 5.4:** OH*-chemiluminescence flame images at the reference operating point of the $NG_{pp}$-, $NG_{tp}$-, $k_{70}$- and $k_{30}$-configuration.

occurs at the radially outer region near the flame tip. This is consistent with previous findings [6]. The flame shape for kerosene combustion in the $k_{70}$-configuration is generally similar to the natural gas cases, with slightly increased lift-off and reduced radial extension. The axial intensity distribution is more uniform. In contrast, the $k_{30}$-configuration exhibits a fundamentally different flame structure. Unlike the disc-like flame observed for all other configurations, the $k_{30}$-flame is notably more compact in the radial direction. This can be attributed to the narrower fuel cone angle, which results in an inhomogeneous fuel distribution with a high concentration at the middle axis.

The impact of the air mass flow on the flame geometry is shown in Figure 5.5. The black dashed contours in all images denote the 50%-isocontour of the respective reference operating point, which is depicted in the middle row. Similar to the previous observations from Bade [7], the flame shape and position remain unaffected by the changes in all four cases. This validates the strategy of maintaining self-similarity in the flow fields for the two liquid scenarios through proportional variation of the atomizing air and main air. With the position and shape of the flame remaining unchanged, modifying the mass flow rate and, consequently, the flow velocity can be understood as a variation of the convective time delay between the burner and the flame for all configurations.

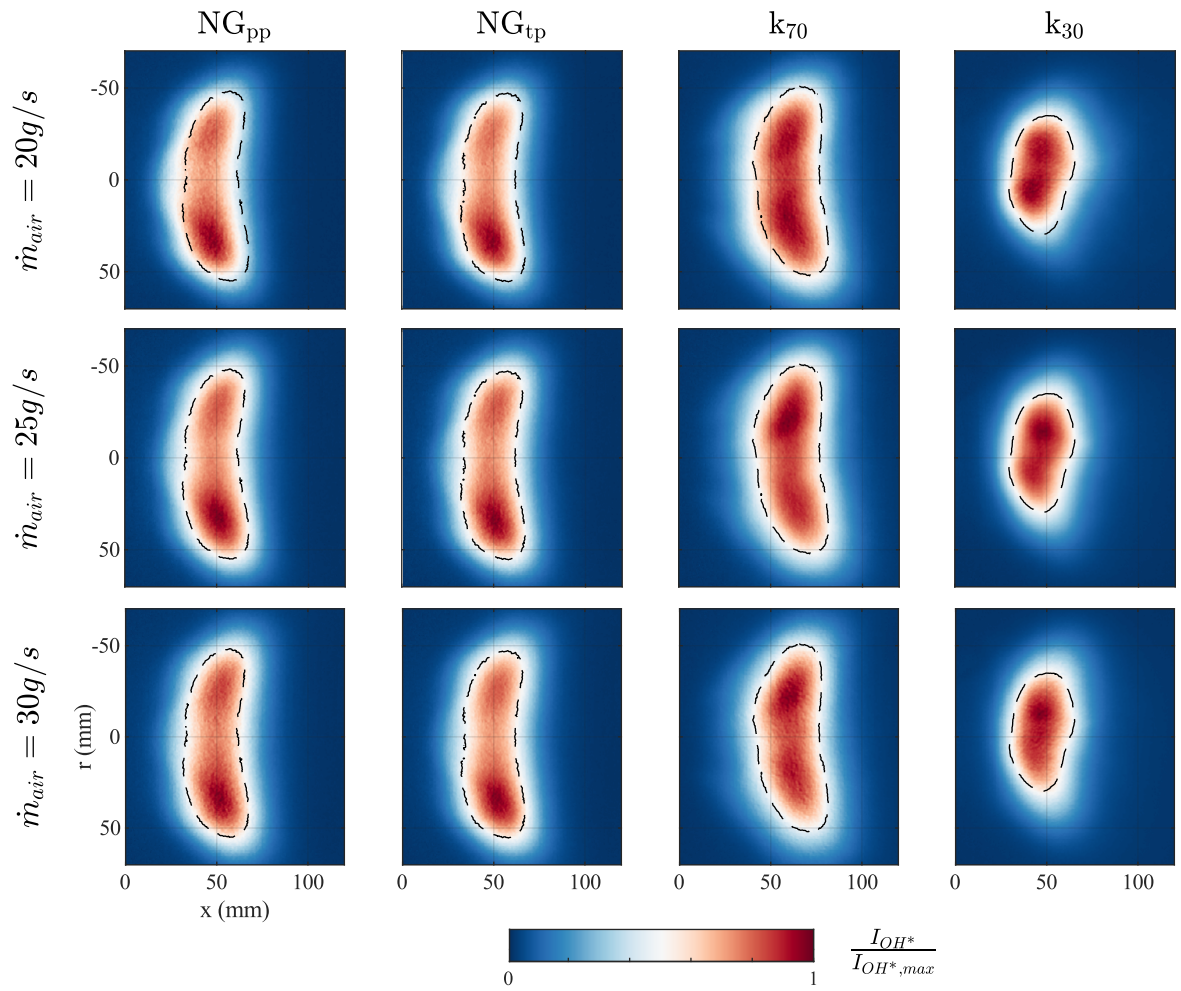


**Figure 5.5:** OH*-chemiluminescence flame images of the NG$_{pp}$-, NG$_{tp}$-, k$_{70}$- and k$_{30}$-configuration for different air mass flows at constant equivalence ratio $\phi$ = 0.675.

Figure 5.6 shows the flame images for three different equivalence ratios at constant air mass flow. For the two liquid fuel cases, this also involves a variation of the SMD, as discussed in Section 5.1. The reference operating point is depicted in the middle row, and the 50%-isocontour of the respective reference operating points is plotted as a dashed black line in all images. The results show that flame shape and position change with the equivalence ratio in all cases, but in different ways. In the two natural gas cases and the k$_{70}$-configuration, the flame contracts radially and moves

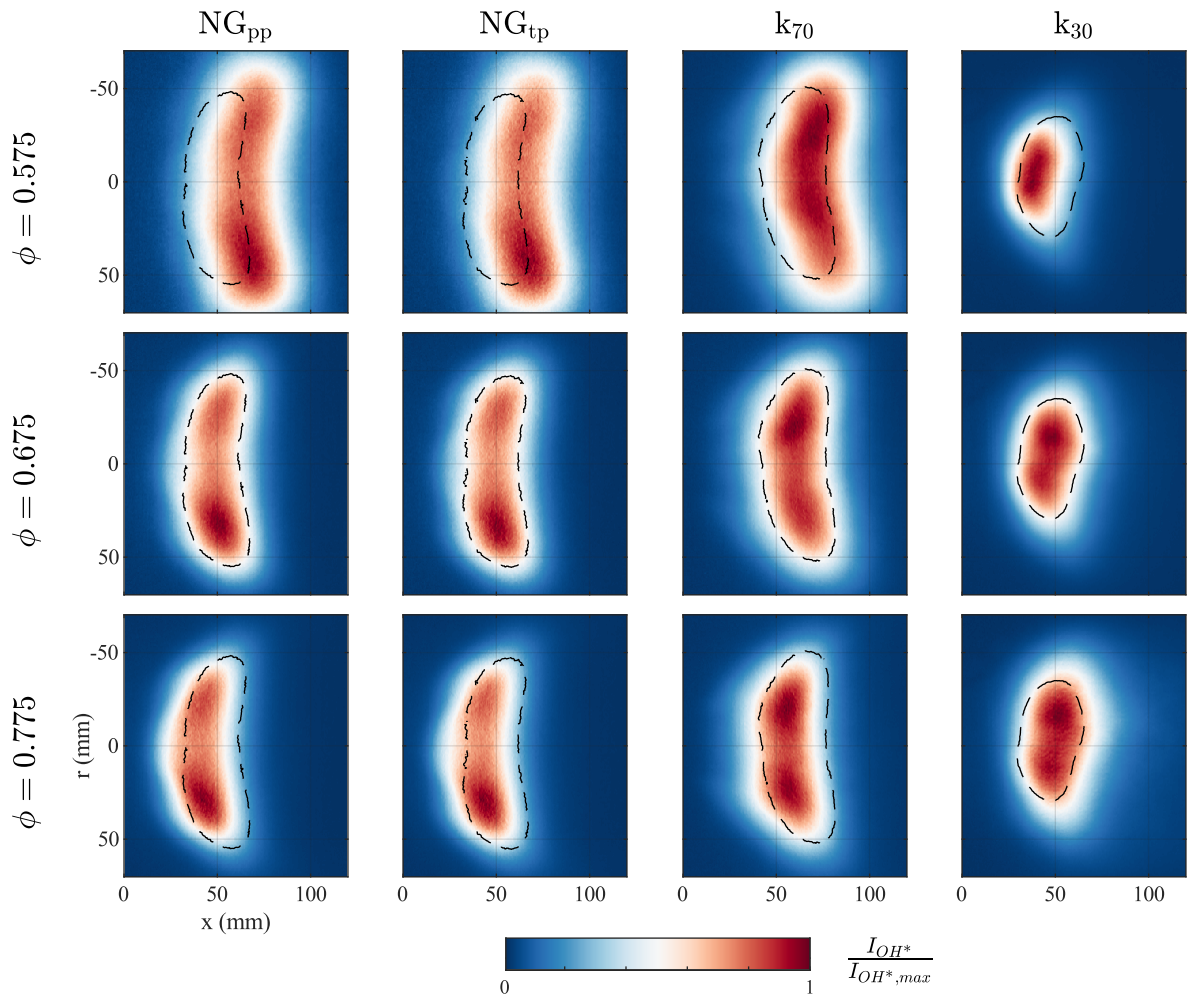


**Figure 5.6:** OH*-chemiluminescence flame images of the $NG_{pp}$-, $NG_{tp}$-, $k_{70}$- and $k_{30}$-configuration for different equivalence ratios at constant air mass flow $\dot{m}_{air}$ = 25 g/s.

upstream as the equivalence ratio increases. This can be attributed to the higher combustion temperatures at higher equivalence ratios, which increase the reactivity and burning velocity. In contrast, the trends observed for the $k_{30}$-configuration are opposite, with a leaner equivalence ratio leading to radial contraction and upstream displacement of the flame, and vice versa. A possible reason for this is the enhanced vaporization quality in the lean case. In the leanest case, the flame reaches the upper and lower combustion chamber walls in the two gas configurations.

From previous studies, it is known that the interaction with the combustion chamber wall can have an impact on the FTF [5,31,36].

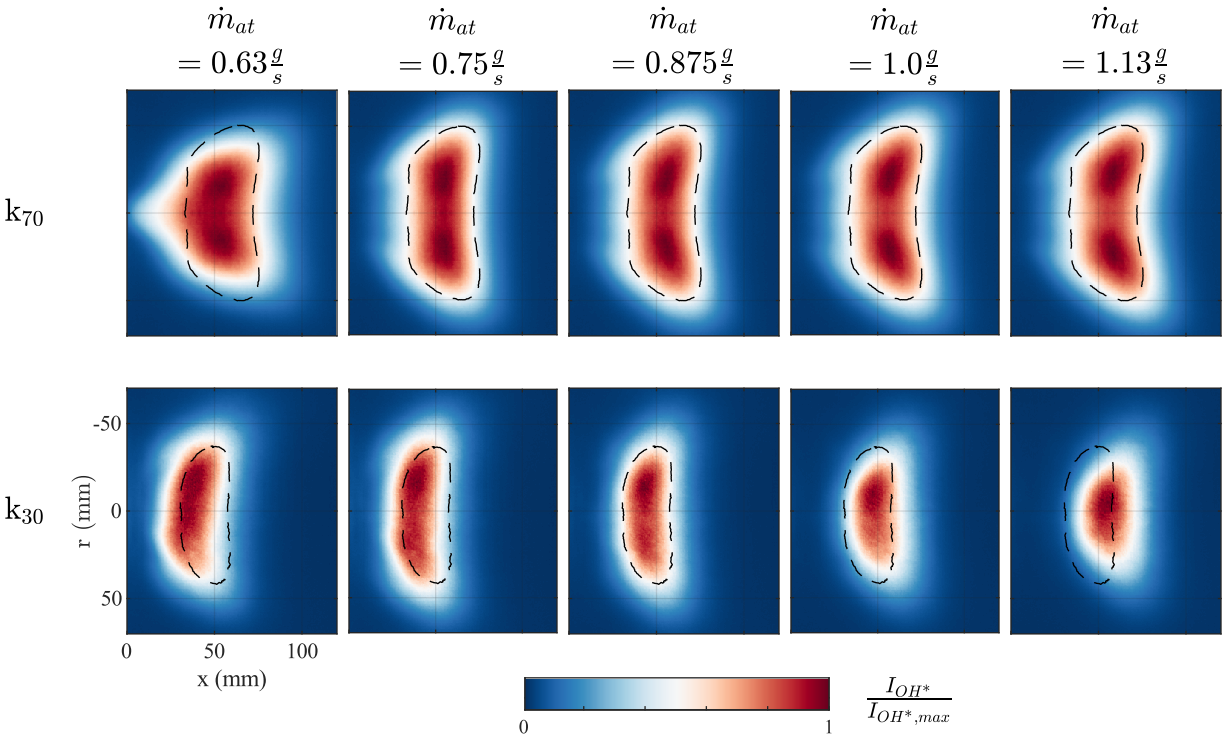


**Figure 5.7:** OH*-chemiluminescence flame images of the $k_{70}$- and $k_{30}$-configuration for different atomizing air mass flows at constant air mass flow $\dot{m}_{air}$ = 25 g/s and constant equivalence ratio $\phi$ = 0.675.

The impact of the atomizing air on the flame shape is discussed next. Figure 5.7 shows flame images for five different atomizing air mass flows ranging from $\dot{m}_{at}$ = 0.63 g/s to $\dot{m}_{at}$ = 1.13 g/s. The $k_{70}$-configuration is displayed in the upper row, and the $k_{30}$-configuration in the lower row. The left image in both rows corresponds to the case with the lowest atomizing air mass flow and the coarsest atomization.

In the $k_{70}$-configuration, the flame shape is almost unaffected by atomizing air mass flow changes over a wide range. Only at the lowest atomizing air mass flow the flame shape changes abruptly due to the transition of the prevailing flame holding mechanism and the flame anchors

in the mixing tube. The liquid fuel injection is located so far upstream that neither droplet diameter nor axial momentum have any impact on the flame shape, as long as they do not fall below a critical minimum. It can therefore be concluded that mixture quality and fuel distribution in the combustion chamber are not affected by changes in the atomizing air mass flow in the $k_{70}$-configuration.

In contrast, in the $k_{30}$-configuration, the flame shape gradually changes with $\dot{m}_{at}$. As the atomizing air mass flow increases, the flame contracts radially. This is in line with the observations for the lean equivalence ratio case. Combining the observations from Figures 5.7 and 5.3 reveals that although the flame volume increases with decreasing $\dot{m}_{at}$, the $NO_x$ emissions increase. This further indicates the presence of strong mixture inhomogeneities in the cases with low atomizing air mass flow.

## 5.4 Summary of the Stationary Operation Characteristics

To summarize, the analysis of the stationary operation yielded the following results:

- In the $k_{70}$-configuration, the fuel always enters the combustion chamber in a fully evaporated state. This can be deduced from an assessment of the droplet's vaporization time, calculated based on the droplet size measurements, and by analyzing the levels of $NO_x$ emissions, which approximate those of natural gas.
- The stationary combustion properties and trends for the $NG_{pp}$-, $NG_{tp}$- and $k_{70}$-configuration are very similar. The fuel is well premixed and distributed over the entire burner outlet cross section, thus resulting in a disc-like flame shape and low $NO_x$ emissions. The flame shape is mainly determined by the flow field.
- The results for the $k_{30}$-configuration are fundamentally different from the other three configurations. Due to the low premixing

length, the fuel is not fully evaporated nor distributed over the entire cross section at the burner outlet. The flame shape is mainly determined by inhomogeneous radial fuel distribution. This results in a radially more compact flame shape and a more diffusive combustion character, which is indicated by the increased $NO_x$ emissions. The flame shape trends in response to variations of $\phi$ and $\dot{m}_{at}$ are opposed between the $k_{30}$-configuration and all other configurations.

In addition, the following conclusions that affect the flame dynamics can be drawn about the different test series:

- Flame shape and position are invariant with respect to the main air mass flow for all configurations. A variation of the air mass flow at constant equivalence ratio is therefore associated with a variation of the convective time delay between burner and flame. $NO_x$ emissions and droplet size are also constant over the air mass flow. This suggests that, besides the convective time delay variation, the main air mass flow variation does not have an effect that is relevant to the flame dynamics.
- Owing to the definition of the operating range, a variation of the equivalence ratio in liquid operation is associated with a change of the ALR at the nozzle and thus of the droplet size.

# 6 Dynamic Properties of Burner and Flame

This chapter presents the experimentally determined dynamic properties of burner and flame. First, the burner scattering matrices for the different configurations with and without liquid fuel injection nozzle are compared with each other. It is shown that the installation of the nozzle does not affect the acoustic properties of the burner. The acoustic forcing level is briefly discussed. After this, FTFs for the different configurations and operating points specified in Section 3.3 are presented. The chapter focuses on describing the observed FTFs and their trends, while most of the interpretation is carried out in the following Chapter 7.

## 6.1 Burner Scattering Matrices

In the following section, experimentally determined scattering matrices of the gas burner without kerosene injection lance are compared with the scattering matrices of the burner with a kerosene injection lance in the $k_{70}$- and $k_{30}$-configuration. The aim is to assess the influence of the injection nozzle on the burner acoustics. The measured scattering matrices are shown in Figure 6.1. All presented matrices are measured without fuel injection at the reference operating point at a main air mass flow of $\dot{m}_{air}$ = 25 g/s and a preheating temperature of $T_{pre}$ = 573 K in the plenum. In the configurations with nozzle, the atomizing air mass flow is $\dot{m}_{at}$ = 0.875 g/s. The axial reference locations of the transfer matrix are at the burner in- and outlet, respectively.

It can be seen that the scattering matrices of all three configurations

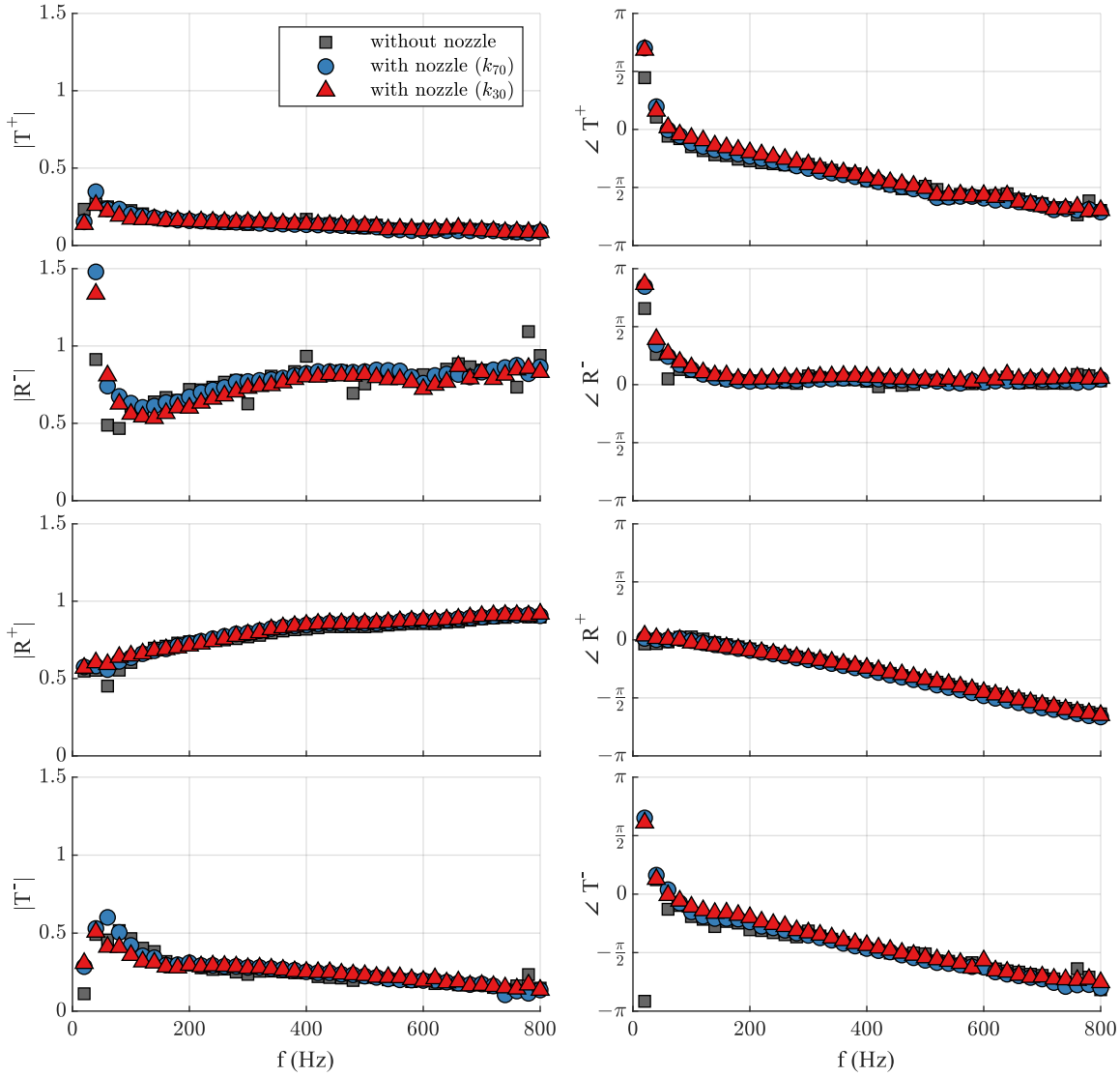


**Figure 6.1:** Burner scattering matrices of the NG-, $k_{70}$- and $k_{30}$-configuration at constant air mass flow $\dot{m}_{air} = 25$ g/s.

agree very well in amplitude and phase for all four elements. In all three configurations, the amplitudes of the transmission coefficients $T^+$ and $T^-$ reach their maximum at low frequencies of 60 Hz and 80 Hz, respectively, and decline towards zero for higher frequencies. Except for the very low frequencies, $f < 80$ Hz, the phase drop of both elements is linear. The downstream reflection coefficient $R^-$ has an amplitude response that reaches its minimum value of around 0.5 at a frequency of 140 Hz, and

then approaches 1 as the frequency increases. The corresponding phase remains almost constant at zero. The amplitude of $R^+$ increases continuously from 0.5 at 0 Hz to 1 at high frequencies. The phase angle drops linearly with increasing frequency. The downstream reflection coefficient $R^-$ exhibits slightly increased scattering at low frequencies. This can be attributed to the weaker acoustic forcing capability of the downstream siren. In summary, the results show that adding the fuel injection nozzle in any configuration does not significantly influence the acoustic scattering behavior of the burner. The burner scattering matrices provide the basis for the determination of the FTFs, which are presented next.

## 6.2 Acoustic Forcing

Figure 6.2 shows the amplitude of the normalized velocity fluctuations at the burner outlet at the reference operating point under upstream forcing for all four configurations. This serves as a measure to determine the acoustic forcing amplitude. The fluctuations have been calculated from the acoustic field upstream of the burner and the burner scattering matrix.

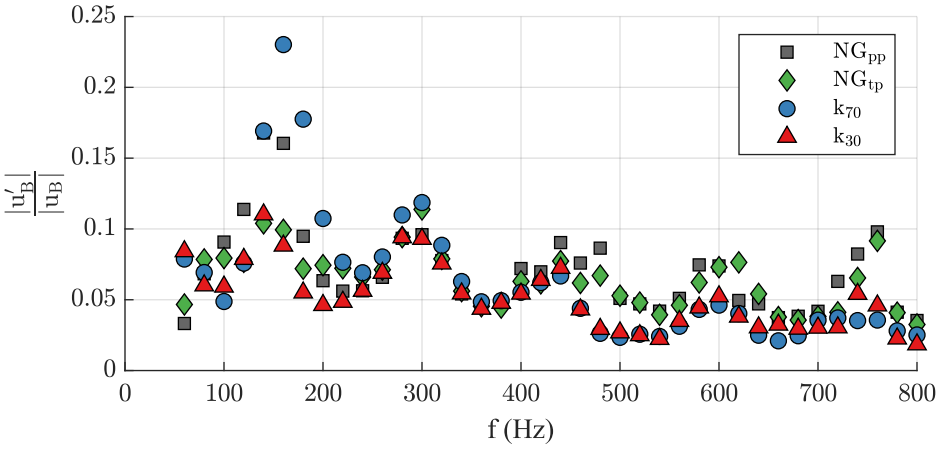


**Figure 6.2:** Normalized velocity oscillation amplitudes at the burner outlet at the reference operating point of the $NG_{pp}$-, $NG_{tp}$-, $k_{70}$- and $k_{30}$-configuration.

Similar trends can be observed for all four configurations. For most frequencies, the relative forcing level is below 10%. A linear flame response and, thus, a linear superposition of the contributing flame response mechanisms can be assumed for this forcing level. The forcing level decreases with increasing frequencies. This trend is superimposed by maxima that regularly occur at intervals of 150 Hz. Under these conditions, the flame may exhibit non-linear effects, and no linear superposition of the contributing flame response mechanisms can be assumed [17,81]. Vogel [94] showed that these frequencies correspond to the eigenfrequencies of the plenum, which causes the amplification of the forcing level. For downstream excitation, the forcing level is generally lower and does not exceed 10%.

## 6.3 Flame Transfer Functions

Figure 6.3 shows the FTFs at the reference operating point of the four different configurations. The two natural gas cases are plotted in the first row, while the second row shows the two kerosene cases. The left plots show the amplitudes; the corresponding phase values are plotted on the right side.

Black squares depict the FTF for the perfectly premixed natural gas configuration. The amplitudes and phases show the typical features of perfectly premixed FTFs. The low frequency limits are $\lim_{f\to 0}|\mathrm{FTF}| = 1$ and $\lim_{f\to 0}\angle\,\mathrm{FTF} = 0$ as discussed in Section 2.3.1. The phase function is linear, except for a phase jump at 200 Hz, which is associated with a local amplitude minimum.

Green diamonds denote the FTF for technically premixed natural gas combustion. As discussed theoretically in Section 2.3.1 and shown in Chapter 7 by means of decomposition, the differences with respect to the $\mathrm{NG_{pp}}$-configuration can be attributed to the presence of equivalence ratio fluctuations. The low frequency limits $\lim_{f\to 0}|\mathrm{FTF}| = 0$ and $\lim_{f\to 0}\angle\,\mathrm{FTF} = \pi/2$ are in line with the theoretical considerations from Sec-

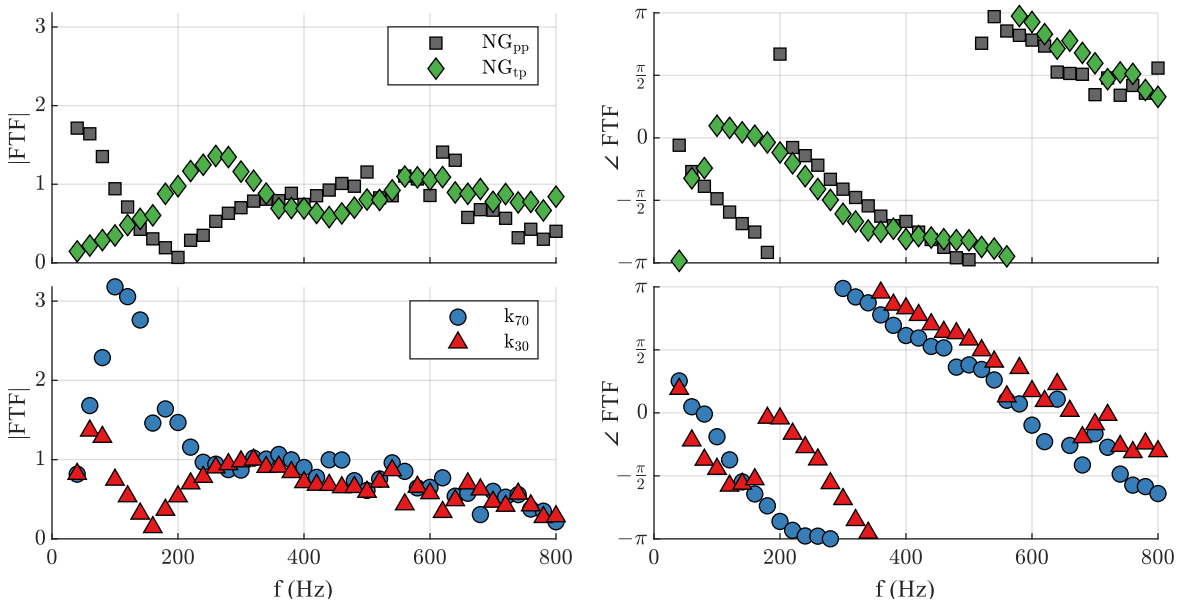


**Figure 6.3:** FTFs at the reference operating point of the $NG_{pp}$-, $NG_{tp}$-, $k_{70}$- and $k_{30}$-configuration depending on $f$.

tion 2.3.1. In contrast to the observations from the $NG_{pp}$-configuration, the FTF has no local amplitude minimum and phase jump at 200 Hz. Instead, a local amplitude maximum at 300 Hz can be observed. Between 300 Hz and 500 Hz, the phase slope is very flat. For $f > 400$ Hz, the amplitudes and phases for the two natural gas configurations converge.

The FTF for the highly premixed kerosene configuration $k_{70}$ is depicted by blue circles in the second row of Figure 6.3. The partially premixed $k_{30}$-configuration is plotted as red triangles. It can be seen that the $k_{30}$-FTF has generally low amplitude values, which is in line with the diffusive combustion character. For very low frequencies $f < 60$ Hz as well as for $f > 300$ Hz, the two FTFs agree in amplitude and phase, while they deviate between 60 Hz and 300 Hz. Similar to the technically premixed natural gas FTFs discussed before, both FTFs approach a low frequency amplitude limit of $\lim_{f\to 0}|\mathrm{FTF}| = 0$ and $\lim_{f\to 0}\angle\mathrm{FTF} = \pi/2$. Between 60 Hz and 300 Hz, the two curves deviate strongly. In the highly premixed $k_{70}$-configuration, the FTF has a distinct amplitude peak with a maximum value of $|\mathrm{FTF}| > 3$ at 120 Hz. In contrast to this, in the partially premixed

$k_{30}$-configuration, the FTF has a local amplitude minimum with an amplitude of zero and a phase jump at 160 Hz. The phases of the two FTFs also differ between 160 Hz and 300 Hz. For $f > 300$ Hz, the FTFs of the two kerosene configurations converge, with amplitudes decaying from |FTF| = 1 at 300 Hz to |FTF| = 0.5 at 800 Hz and a linear phase slope.

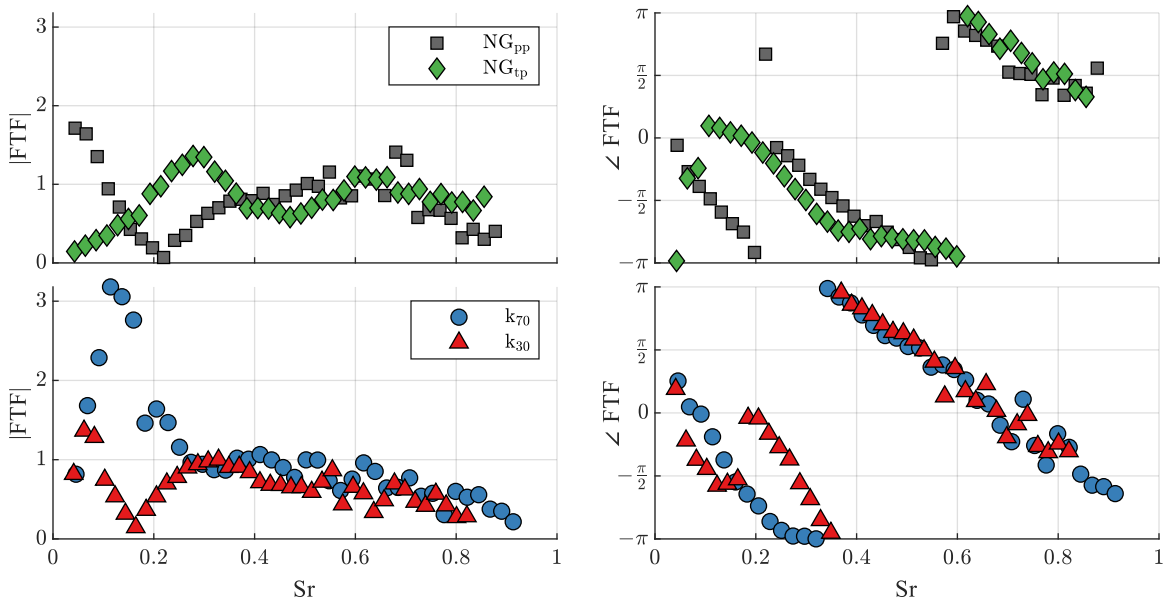


**Figure 6.4:** FTFs at the reference operating point of the $NG_{pp}$-, $NG_{tp}$-, $k_{70}$- and $k_{30}$-configuration depending on $Sr$.

For the comparison across different operating conditions, FTFs are often plotted over the dimensionless Strouhal number $Sr$, which relates the frequency to the convective time scale [5,32,56]. For the natural gas configuration of the current burner, this has been discussed in detail by Bade [6]. The Strouhal number is defined as follows:

$$Sr = \frac{f x_{cg}}{u_B}. \tag{6.1}$$

Herein, $x_{cg}$ is the axial coordinate of the flame center of gravity, which is determined from the stationary flame images as described in Section 4.1.1. The mean flow velocity at the burner outlet $u_B$ is calculated from the mass flow in the burner outlet plane.

Figure 6.4 shows the previously discussed FTFs over the Strouhal num-

ber. The Strouhal notation causes an individual axial scaling of the FTF curves, depending on the corresponding flame lift-off. As discussed in Section 5.3, the axial lift-off distance of the flame is similar in all four configurations. Consequently, the relative position of the FTFs to each other changes only slightly compared to the notation over the frequency.

### 6.3.1 Air Mass Flow Variation

The FTF sensitivity on the main air mass flow is assessed first. As discussed in Section 5.3, the variation of the air mass flow can be interpreted as a variation of the convective delay times in the combustor for all configurations due to the self-similar flame geometries. Figure 6.5 shows FTFs for $\dot{m}_{air}$ = 20 g/s, $\dot{m}_{air}$ = 25 g/s and $\dot{m}_{air}$ = 30 g/s at constant equivalence ratio $\phi$ = 0.675 for all four configurations. The FTFs are plotted over the frequency. The blue symbols in each plot correspond to the lowest mass flow, and the red symbols correspond to the highest mass flow.

In all four configurations, the FTFs have a similar shape but behave differently along the frequency axis. This can be seen especially from the phases. The phase drop increases with decreasing mass flow in all four cases. A decreased mass flow corresponds to longer convective time delays. The FTF notation over the Strouhal number plotted in Figure 6.6 compensates for the differences in the convective delay between the burner outlet and the flame.

It can be seen that in the Strouhal notation, the three curves for the different air mass flow rates are similar in all four configurations. Only a minor deviation can be observed in the two kerosene cases. This indicates that the observed FTF trends for the air mass flow variation can be entirely attributed to changes in the convective delay time between burner outlet and flame.

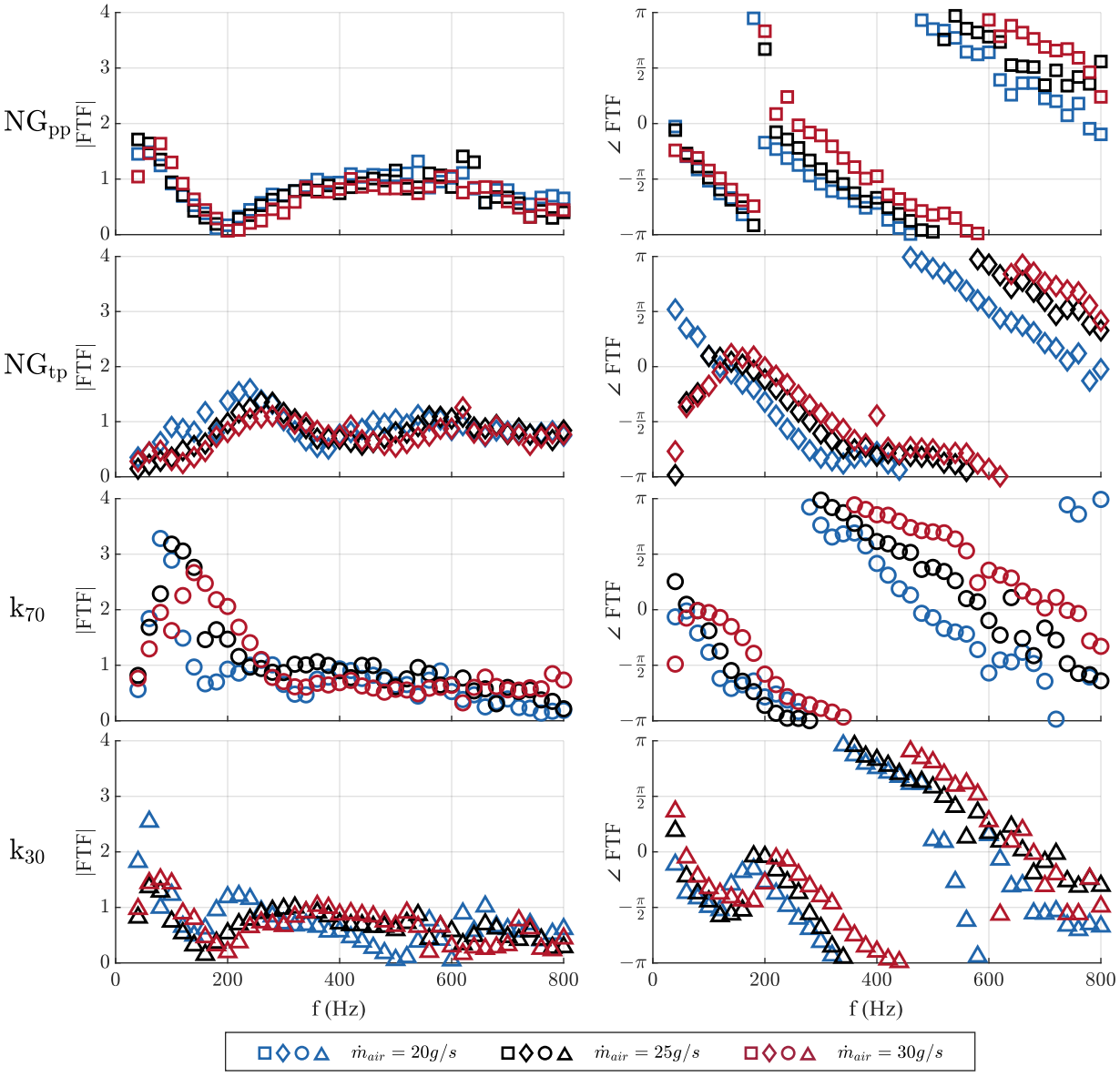


**Figure 6.5:** FTFs of the $NG_{pp}$-, $NG_{tp}$-, $k_{70}$- and $k_{30}$-configuration for different air mass flows at constant equivalence ratio $\phi = 0.675$ depending on $f$.

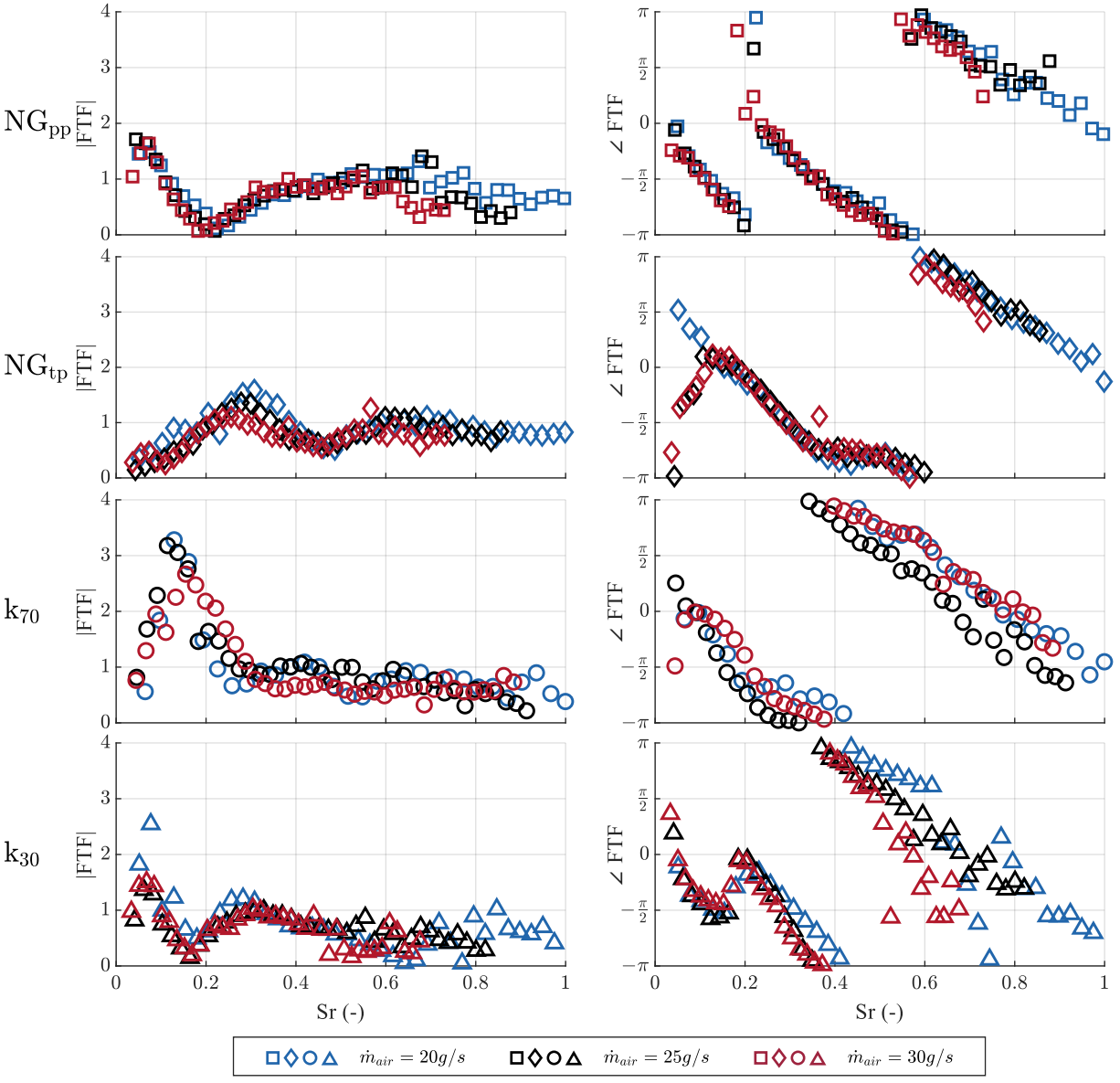


**Figure 6.6:** FTFs of the $NG_{pp}$-, $NG_{tp}$-, $k_{70}$- and $k_{30}$-configuration for different air mass flows at constant equivalence ratio $\phi = 0.675$ depending on $Sr$.

### 6.3.2 Equivalence Ratio Variation

Next, the sensitivity of the FTFs on the equivalence ratio is discussed. Figure 6.7 shows the FTFs for three different equivalence ratios $\phi$ = 0.575, $\phi$ = 0.675 and $\phi$ = 0.775 at constant air mass flow $\dot{m}_{air}$ = 25 g/s over the frequency. The blue symbols denote the leanest case.

In all cases, the equivalence ratio significantly affects the FTFs in amplitude and phase. Except for the $k_{30}$-configuration, the peak amplitude increases, and the phase drops stronger with decreasing equivalence ratio in all cases. In the $NG_{pp}$-configuration, the local minimum and the phase jump are additionally at lower frequencies with decreasing equivalence ratio. In the $NG_{tp}$- and $k_{70}$-configuration, the FTF exhibits a local minimum and a phase jump in the high equivalence ratio case.

In the $k_{30}$-configuration, the peak amplitude declines, and the phase slope flattens with decreasing equivalence ratio, which is opposite to the observations for all other configurations. The local amplitude minimum and the associated phase jump are shifted towards lower frequencies with decreasing equivalence ratio.

The FTF plot over $Sr$ is given in Figure 6.8. In contrast to the observations from the main air mass flow variation, the FTFs still differ in amplitude and phase when plotted over $Sr$. The frequency shift of the local minima in the $NG_{pp}$- and $k_{30}$-configuration is still visible. The phases are only similar in the $k_{30}$-configuration for $Sr > 0.2$. However, at the same time, the amplitude differences increase when plotted over $Sr$. In the $NG_{pp}$- and $NG_{tp}$-configuration, the phases of the $\phi$ = 0.675 and $\phi$ = 0.775 cases are similar for high frequencies, but the phase for the leanest case deviates from the other two.

The observed FTF trends in response to changes in the equivalence ratio can thus not be attributed to changes in the convective delay time between burner outlet and flame. This is discussed in detail in Chapter 7.

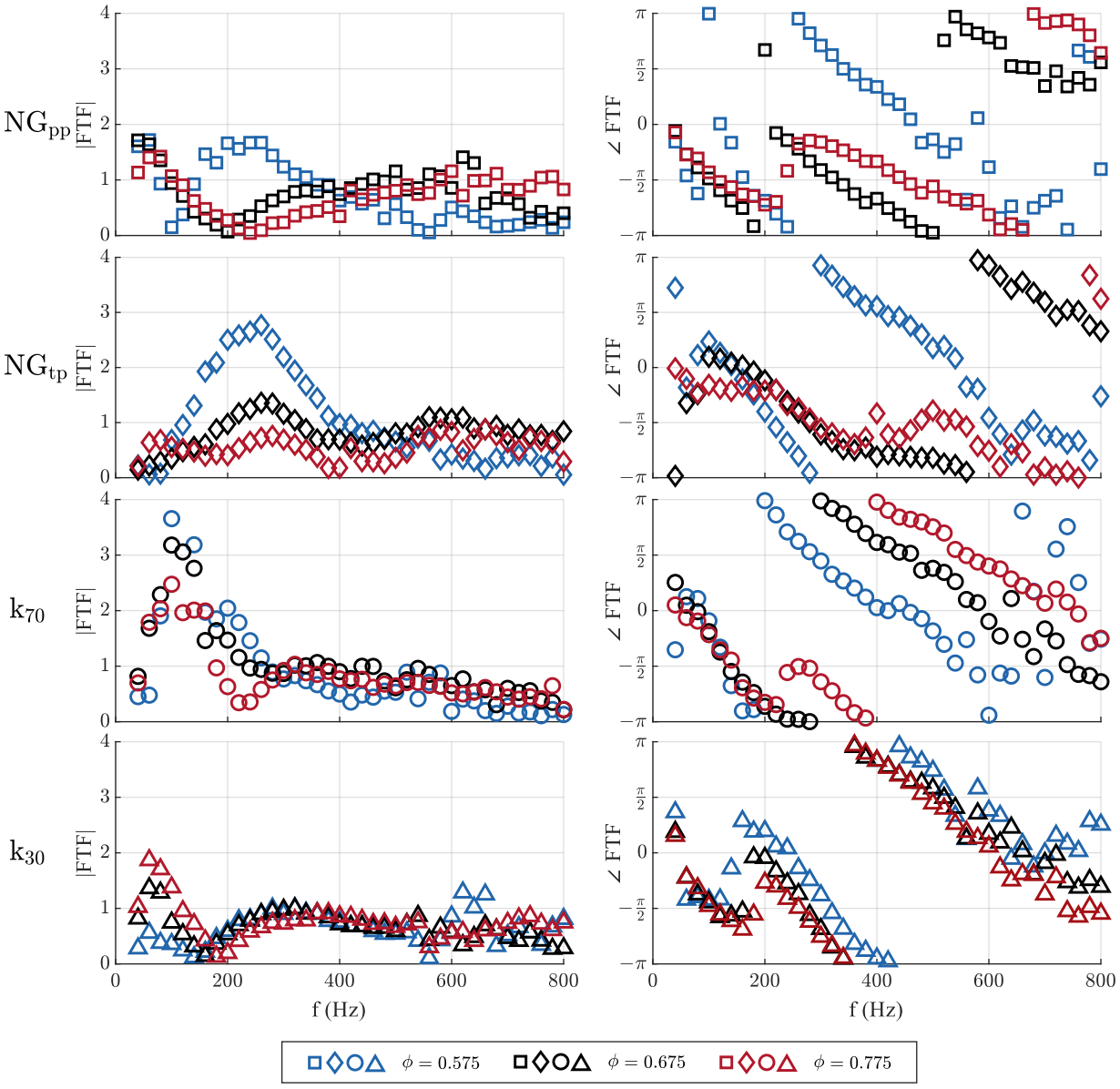


**Figure 6.7:** FTFs of the $NG_{pp}$-, $NG_{tp}$-, $k_{70}$- and $k_{30}$-configuration for different equivalence ratios at constant air mass flow $\dot{m}_{air}$ = 25 g/s depending on $f$.

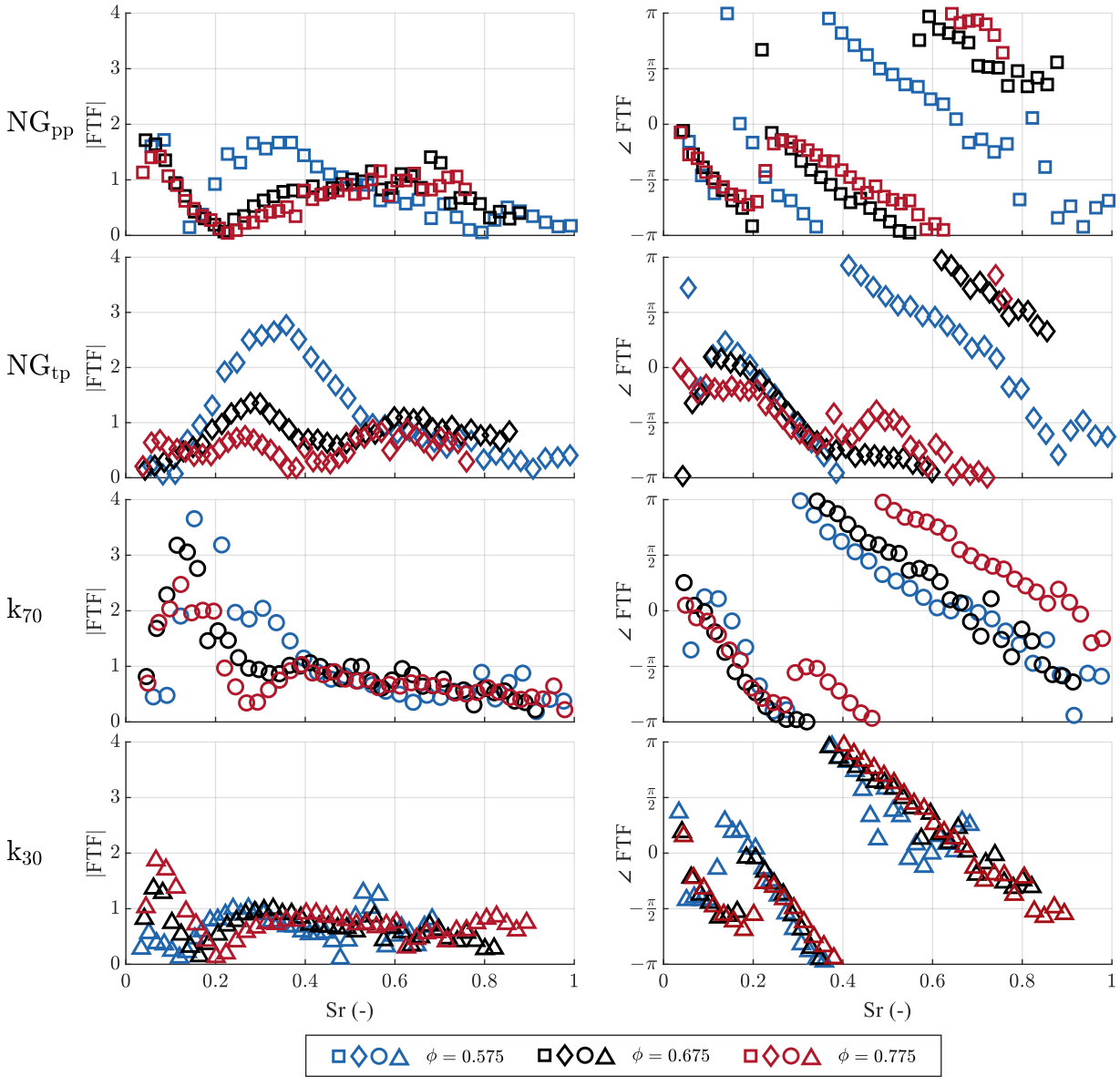


**Figure 6.8:** FTFs of the $NG_{pp}$-, $NG_{tp}$-, $k_{70}$- and $k_{30}$-configuration for different equivalence ratios at constant air mass flow $\dot{m}_{air}$ = 25 g/s depending on $Sr$.

### 6.3.3 Atomizing Air Mass Flow Variation

Figure 6.9 shows the FTFs for five different atomizing air mass flow rates at constant main air mass flow $\dot{m}_{air}$ = 25 g/s and equivalence ratio $\phi$ = 0.675 in the $k_{70}$- and $k_{30}$-configuration. Blue symbols denote the lowest atomizing air mass flow corresponding with the coarsest droplets. The highest atomizing air mass flow with the finest droplets is represented by red symbols.

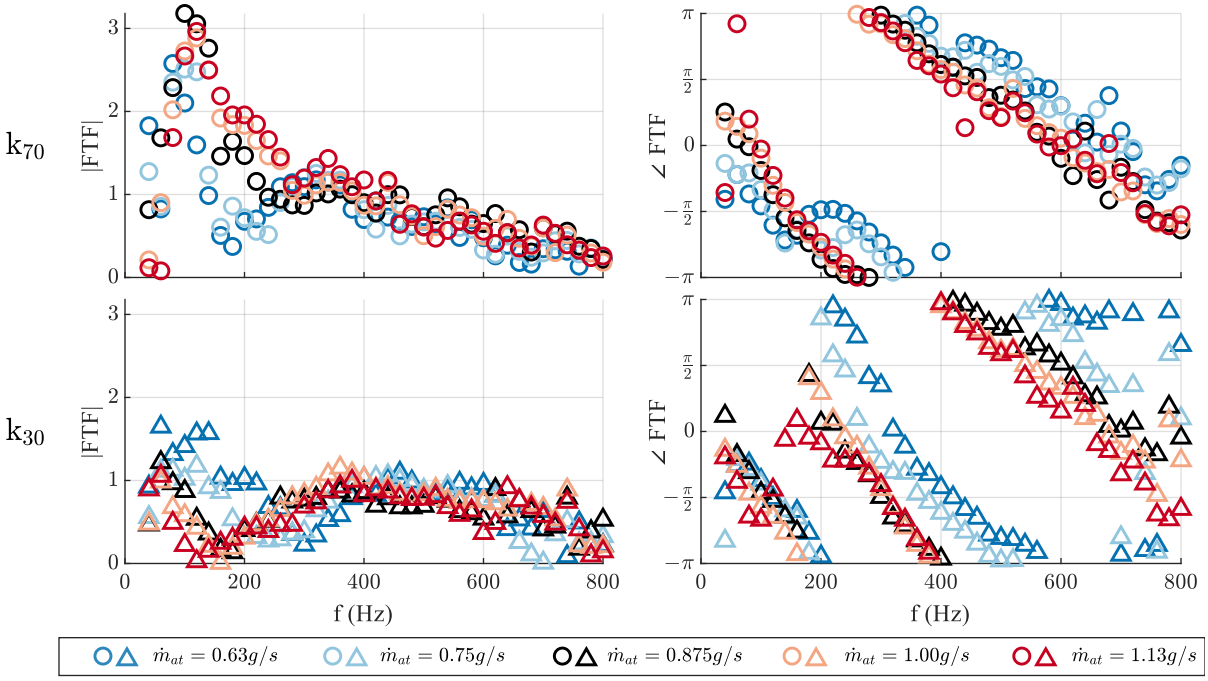


**Figure 6.9:** FTFs of the $k_{70}$- and $k_{30}$-configuration for different atomizing air mass flows at constant air mass flow $\dot{m}_{air}$ = 25 g/s and constant equivalence ratio $\phi$ = 0.675 depending on $f$.

The $k_{70}$-configuration is analyzed first. Although, as discussed in Chapter 5, the atomizing air mass flow does not have an impact on flame shape and $NO_x$ emissions, the FTF is strongly affected in the frequency range between the amplitude maximum at 100 Hz and 300 Hz. A high atomizing air mass flow results in a linear phase slope without phase jump and a flat amplitude decay after the maximum. This increases the amplitude between 100 Hz and 300 Hz. Vice versa, a lower atomizing air mass

flow decreases the FTF amplitude for frequencies above the amplitude maximum and leads to the formation of an amplitude minimum with an associated phase jump at 180 Hz. For $f > 300$ Hz, the amplitudes and phases of the different atomizing air mass flows are similar. Although, as discussed in Section 5.3, the flame shape for the lowest atomizing air mass flow is significantly different from all others, the corresponding FTF does not differ significantly from the others.

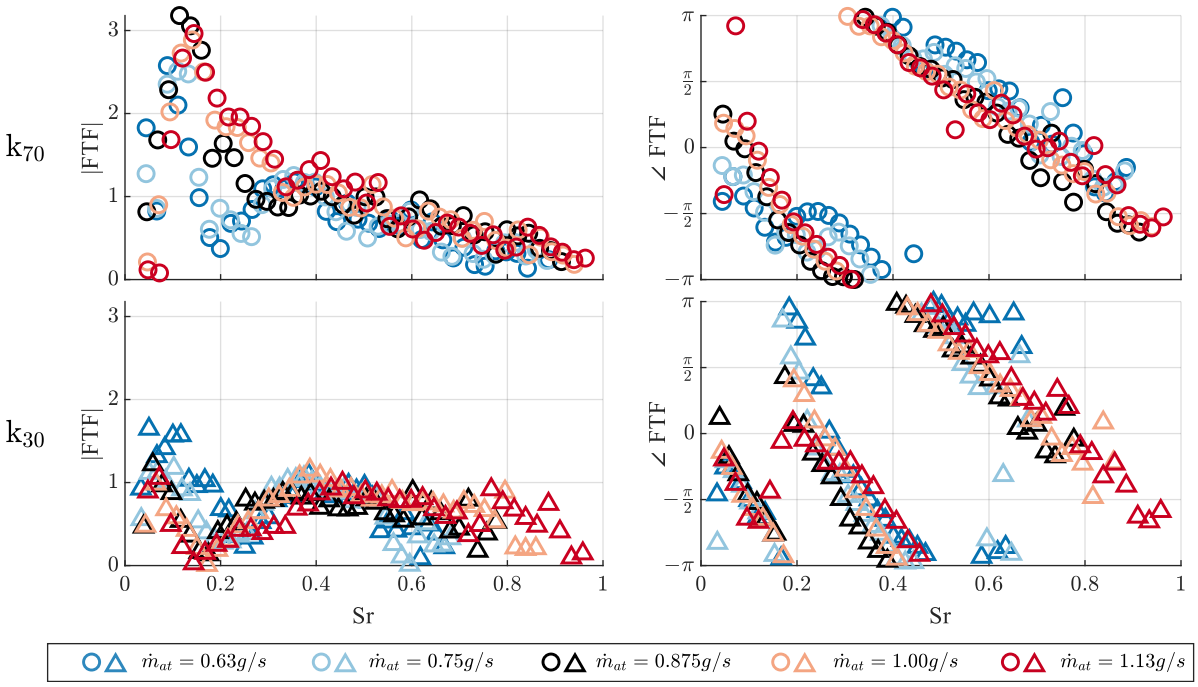


**Figure 6.10:** FTFs of the $k_{70}$- and $k_{30}$-configuration for different atomizing air mass flows at constant air mass flow $\dot{m}_{air}$ = 25 g/s and constant equivalence ratio $\phi$ = 0.675 depending on $Sr$.

In the $k_{30}$-configuration, the effect of the atomizing air mass flow variation on the FTF is fundamentally different. A lower atomizing air mass flow leads to an amplitude increase in the low frequency range and shifts the local minimum to higher frequencies, thus enlarging the low frequency regime range. This is in line with the observations from the equivalence ratio variation discussed before. For high frequencies, the amplitudes converge. The phase slope increases with increasing $\dot{m}_{at}$.

In Figure 6.10, the FTFs are given over the Strouhal number. No change can be observed for the $k_{70}$-configuration. In the $k_{30}$-configuration, the phases converge due to the different axial scaling.

# 7 Analytical Modeling and Analysis

The analytical FTF model introduced in Section 4.3 is applied in this chapter to reproduce the experimentally obtained FTFs from Chapter 6. For this purpose, parametric scaling rules are derived that allow to calculate the model parameters as functions of the flame geometry.

Following the idea of Schuermans et al. [81] and Freitag [33], the parametric scaling rules for perfectly premixed natural gas FTFs are adopted for the technically premixed natural gas configuration. In the technically premixed case, they are merely supplemented by scaling rules for the two additional parameters representing the equivalence ratio fluctuations: Furthermore, the parametric scaling rules for the perfectly premixed natural gas FTFs are also applied to the FTF model of the $k_{70}$-configuration. This is motivated by the conclusion drawn in Chapter 5 that the fuel spray is fully evaporated at the combustion chamber inlet, which leads to the assumption that the mass flow and swirl fluctuation mechanisms apply to the $k_{70}$-configuration in a similar way as to the natural gas cases. The parameters representing the equivalence ratio fluctuation coupling are separately fitted for the $k_{70}$-configuration to account for the different inertia of the droplets compared to natural gas as discussed in Section 4.3. It is shown that the fitted parameters agree well with the experimentally determined parameters from Vogel et al. [96].

The validity of the introduced model can be concluded by its ability to accurately describe the flame dynamics in three different configurations across the entire operating range in a single approach, with good agreement between the model predictions and experimental data. The model is therefore interpreted physically as a decomposition of the FTF into the different contributing mechanisms in the following.

In contrast, for the $k_{30}$-configuration, it was not possible to derive a set of model parameters that satisfactorily reproduced the flame dynamics over the entire operating range. This can be interpreted as a further indication that the flame driving mechanisms are fundamentally different in this case.

To further validate the method, the modeling approach is additionally applied to experimentally determined FTFs from an industrial burner design. The results can be found in Appendix A.4.

## 7.1 Parameter Scaling Rules

As discussed in Section 4.3, the applied model contains three terms representing the impact of mass flow fluctuations (index M), swirl fluctuations (index S), and equivalence ratio fluctuations (index $\phi$), respectively. From the combination of Equations 4.13, 4.14 and 4.15, according to Equation 4.11, the analytical model FTF formulation for technically premixed flames reads:

$$FTF(\omega) = \underbrace{\frac{e^{-i\omega\tau_{M1}}}{1+\alpha_{M1}i\omega+(\alpha_{M2}i\omega)^2}}_{FTF_M} + \underbrace{n\cdot\left(e^{-i\omega\tau_{S1}-\frac{1}{2}\omega^2\sigma_S^2}-e^{-i\omega\tau_{S2}-\frac{1}{2}\omega^2\sigma_S^2}\right)}_{FTF_S} - \underbrace{e^{-i\omega\tau_\phi-\frac{1}{2}\omega^2\sigma_\phi^2}}_{FTF_\phi}. \tag{7.1}$$

For perfectly premixed FTFs, the $FTF_\phi$ term is omitted and the FTF composes from $FTF_M$ and $FTF_S$ only.

Based on the considerations from the model description in Section 4.3, the parameters are linearly linked to the flame geometry parameters as follows:

- $\tau_{M1}$, $\tau_{S1}$, $\tau_{S2}$ and $\tau_\phi$ represent the convective time delay between

burner outlet and flame, swirler and flame and fuel injection and flame respectively. The determining flame geometry parameter is thus the axial position of the flame. Consequently, the variables are linked to the axial position of the flame center of gravity, $x_{cg}$. Note that, due to the combination with other terms, except for $\tau_\phi$, the values cannot be interpreted as the actual delay times [33].

- $\alpha_{M1}$, $\alpha_{M2}$, $\sigma_S$ and $\sigma_\phi$ are model parameters for the time delay dispersions accounting for the spatial distributions of heat release, swirl generation, and fuel injection. The spatial distributions of heat release and swirl generation are invariant, and the release distribution is the only remaining operating point-dependent quantity. The time delay dispersion scales with the heat release distribution in flow direction, which can be approximated as being axial. The variables are therefore linked to the axial length of the combustion zone $l_{fl}$.

- The vortex interaction index $n_S$ covers the observation that vortices and, thus, the swirl fluctuation-related feedback mechanism are gaining intensity with increasing radial extension. Consequently, $n_S$ is linked to the radial flame extension $d_{fl}$.

Furthermore, the following scaling is applied to account for the effects of different main air flow velocities and droplet sizes which are not related to the flame geometry:

- In order to account for the different axial scaling of the FTFs for different main air mass flows at constant equivalence ratio, all parameters are inversely scaled with $\dot{m}_{air}$. This resembles the Strouhal scaling of the FTF applied in Chapter 6.

- In the case of liquid combustion, the atomization quality is expected to have an impact on $\tau_\phi$ and $\sigma_\phi$. This is accounted for by additionally inversely scaling the two variables with the ALR.

## 7.2 Combined Model for the $NG_{pp}$-, $NG_{tp}$- and $k_{70}$-Configuration

The scaling rules for the seven model parameters of the $NG_{pp}$-configuration as functions of the flame geometry are listed below:

$$\begin{pmatrix} \tau_{M1} \\ \alpha_{M1} \\ \alpha_{M2} \\ n_S \\ \tau_{S1} \\ \sigma_S \\ \tau_{S2} \end{pmatrix} = \left[ \begin{pmatrix} 1.53 \cdot 10^{-2}\, ms\, \frac{g}{s} \\ 2.39 \cdot 10^{-2}\, ms\, \frac{g}{s} \\ 2.67 \cdot 10^{-2}\, ms\, \frac{g}{s} \\ 3.22 \cdot 10^{-2} \frac{g}{s} \\ -2.41 \cdot 10^{-2}\, ms\, \frac{g}{s} \\ -2.65 \cdot 10^{-2}\, ms\, \frac{g}{s} \\ -6.89 \cdot 10^{-2}\, ms\, \frac{g}{s} \end{pmatrix} + \begin{pmatrix} 2.09 \cdot 10^{-4}\, \frac{ms}{mm}\, \frac{g}{s} \cdot x_{cg} \\ 1.42 \cdot 10^{-4}\, \frac{ms}{mm}\, \frac{g}{s} \cdot l_{fl} \\ 2.60 \cdot 10^{-6}\, \frac{ms}{mm}\, \frac{g}{s} \cdot l_{fl} \\ 1.99 \cdot 10^{-1}\, \frac{1}{mm}\, \frac{g}{s} \cdot d_{fl} \\ 1.06 \cdot 10^{-3}\, \frac{ms}{mm}\, \frac{g}{s} \cdot x_{cg} \\ 5.79 \cdot 10^{-4}\, \frac{ms}{mm}\, \frac{g}{s} \cdot l_{fl} \\ 2.36 \cdot 10^{-3}\, \frac{ms}{mm}\, \frac{g}{s} \cdot x_{cg} \end{pmatrix} \right] \cdot \frac{1}{\dot{m}_{air}}.$$

In addition, the scaling rules for the parameters of $FTF_\phi$ are given for the $NG_{tp}$-configuration by:

$$\begin{pmatrix} \tau_\phi \\ \sigma_\phi \end{pmatrix} = \left[ \begin{pmatrix} 2.51 \cdot 10^{-2}\, ms\, \frac{g}{s} \\ -1.49 \cdot 10^{-2}\, ms\, \frac{g}{s} \end{pmatrix} + \begin{pmatrix} 1.04 \cdot 10^{-3}\, \frac{ms}{mm}\, \frac{g}{s} \cdot x_{cg} \\ 4.63 \cdot 10^{-4}\, \frac{ms}{mm}\, \frac{g}{s} \cdot l_{fl} \end{pmatrix} \right] \cdot \frac{1}{\dot{m}_{air}}.$$

For the $k_{70}$-configuration, the scaling rules for these parameters are:

$$\begin{pmatrix} \tau_\phi \\ \sigma_\phi \end{pmatrix} = \left[ \begin{pmatrix} -9.94 \cdot 10^{-2}\, ms\, \frac{g}{s} \\ -3.41 \cdot 10^{-2}\, ms\, \frac{g}{s} \end{pmatrix} + \begin{pmatrix} 3.09 \cdot 10^{-3}\, \frac{ms}{mm}\, \frac{g}{s} \cdot x_{cg} \\ 7.21 \cdot 10^{-4}\, \frac{ms}{mm}\, \frac{g}{s} \cdot l_{fl} \end{pmatrix} \right] \cdot \frac{1}{\dot{m}_{air} \cdot ALR}.$$

The resulting model parameter trends are plotted exemplarily for the equivalence ratio variation of all three configurations over the respective corresponding flame geometry length scale evaluated in Figure 7.1. The values are normalized with the parameters at $\phi = 0.675$, $\dot{m}_{air} = 25$ g/s in the $NG_{tp}$-configuration to make the comparison easier. Parameters contributing to $FTF_M$ are plotted in blue color, parameters contributing to $FTF_S$ are plotted in red color, and parameters contributing to $FTF_\phi$ are plotted in green color. In addition to the 9 parameters, the two derived values $\alpha_{M1}/\alpha_{M2}$ and $\tau_{S2} - \tau_{S1}$ are plotted as empty symbols.

The following conclusions regarding the FTF trends can be drawn from the parameters:

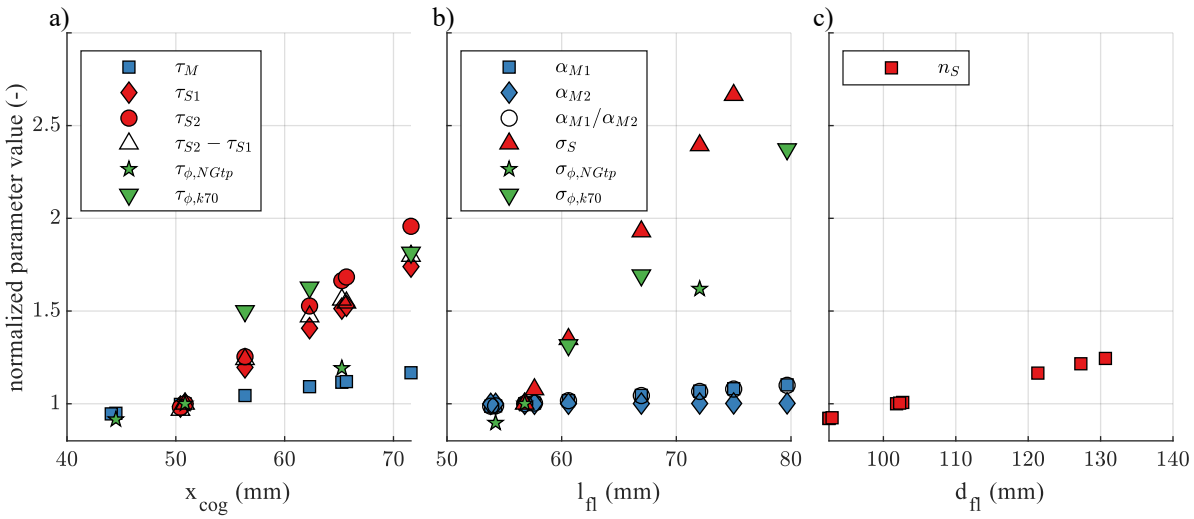


**Figure 7.1:** FTF model parameters of the $NG_{pp}$-, $NG_{tp}$- and $k_{70}$-configuration for different equivalence ratios at constant air mass flow $\dot{m}_{air}$ = 25 g/s over the corresponding flame geometry parameters: (a) $x_{cg}$, (b) $l_{fl}$ and (c) $d_{fl}$.

- As expected from the model specifications, all parameters show linear trends with regard to the respective geometry parameter and lie on a straight line in each case. The exception to this are the parameters $\tau_\phi$ and $\sigma_\phi$ corresponding to $FTF_\phi$. These form different straight lines for the $NG_{tp}$ and $k_{70}$-configurations respectively.
- The parameters corresponding to $FTF_M$ show only low sensitivity to the flame geometry, whereas the parameters corresponding to $FTF_S$ are very sensitive to the flame geometry.
- The time delays corresponding to $FTF_\phi$ have a similar slope and are merely shifted by a fixed offset. This can be interpreted as the additional acceleration time delay in the liquid case.
- The amplitude maximum of $FTF_S$ is shifted towards lower frequencies with increasing axial displacement and flame length due to the increase of the corresponding time delay difference $\tau_{S2} - \tau_{S1}$ and the dispersion term $\sigma_S$.
- The time delay difference $\tau_{S2} - \tau_{S1}$ rises with flame length, while $n_S$

increases with flame width, both of which promote an increase of the maximum amplitude of $FTF_S$. However, the increase of $\sigma_S$ reduces the amplitude maximum. Thus, no clear trend can be predicted for the amplitude maximum of $FTF_S$.

The implications of the observed trends on the mechanism superposition and the resulting FTF are discussed in the following.

### 7.2.1 Reference Operating Point

Figure 7.2 shows the flame geometry parameters, which were derived from the flame images according to the description in Section 5.3 at the reference operating point. The coordinates serve as input for the FTF reconstruction. The two natural gas cases have a nearly identical flame geometry. In the $k_{70}$-configuration, the flame lift-off and the axial extension increase by 10 mm compared to the natural gas cases.

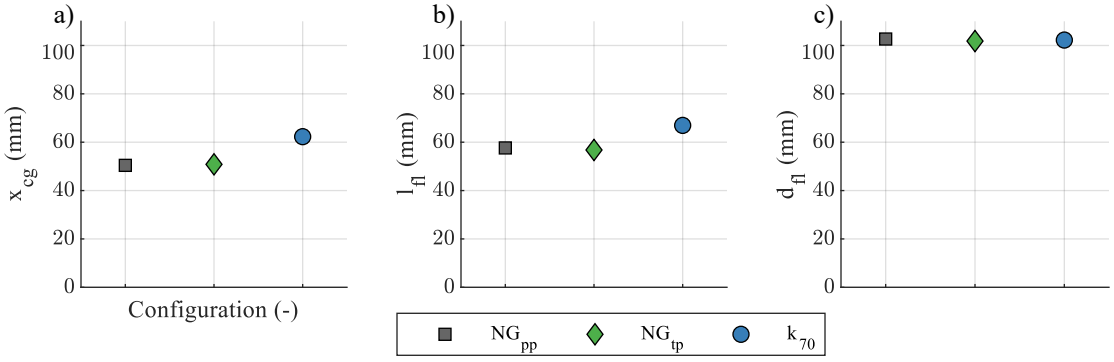


**Figure 7.2:** Flame geometry parameters at the reference operating point of the $NG_{pp}$-, $NG_{tp}$- and $k_{70}$-configuration: (a) $x_{cg}$, (b) $l_{fl}$ and (c) $d_{fl}$.

The resulting model reconstruction at the reference operating point for perfectly premixed natural gas combustion is compared to the experimental data in Figure 7.3.

The mass flow fluctuation contribution $FTF_M$ is denoted by dashed blue

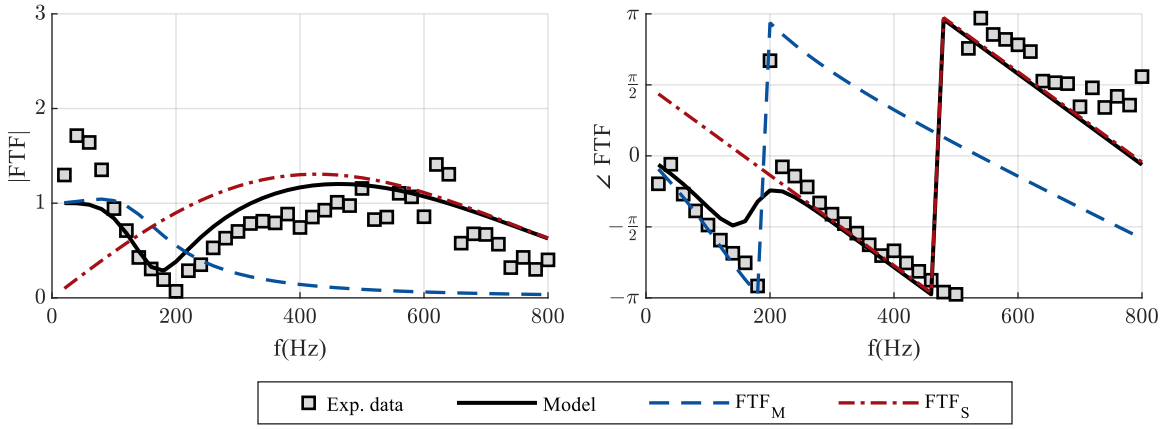


**Figure 7.3:** Comparison of model FTF and experimental data at the reference operating point of the $NG_{pp}$-configuration.

lines in the amplitude and phase plots, whereas the swirl fluctuation contribution $FTF_S$ is given by red dot-dashed lines. The resulting analytical model FTF from the superposition of the two mechanisms is plotted as a thick black line. Square symbols denote the experimental data. The model matches the experimental data very well, thus allowing for a physical analysis of the contributing terms.

In accordance with the results from Bade [6], $FTF_M$ is predominantly present at low frequencies and decays with increasing frequency. The phase is not completely linear. The phase drop is steepest at low frequencies and gradually becomes less steep as the frequency increases. Mathematically, this can be explained by the second order time delay element [33]. The swirl fluctuation $FTF_S$ contribution has a strictly linear phase slope. The amplitude maximum is at around 500 Hz. The resulting model FTF is consequently dominated by $FTF_M$ for low frequencies $f <$ 200 Hz, while for $f >$ 200 Hz, the swirl fluctuation mechanism is dominant. The local amplitude minimum at 200 Hz is caused by destructive interference of the two mechanisms, which have the same magnitude and a phase difference of $\pi$ at this frequency. The associated phase jump can be explained with the FTF phase shifting from following the phase slope of $FTF_M$ to the phase slope of $FTF_S$.

The model FTF for the technically premixed natural gas configuration at the reference operating point is given in Figure 7.4. Again, the model agrees very well with the experimental data.

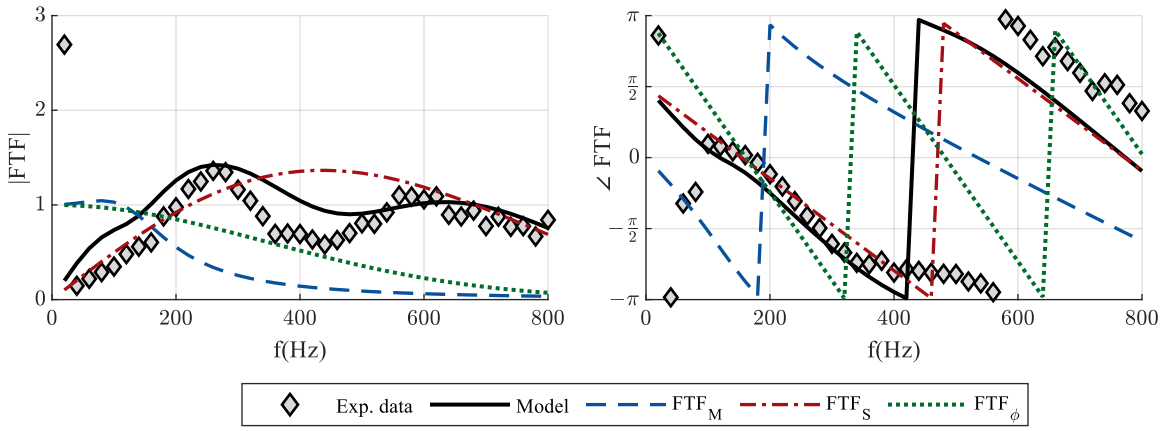


**Figure 7.4:** Comparison of model FTF and experimental data at the reference operating point of the $NG_{tp}$-configuration.

As could be expected due to the almost identical flame shape, $FTF_M$ and $FTF_S$ are similar to the previously discussed. The additional equivalence ratio fluctuation term $FTF_\phi$ is denoted by green dotted lines in both plots. Similar to the mass flow coupling mechanism, the equivalence ratio fluctuation term reaches its maximum amplitude in the low frequency range and decays with increasing frequency. The phase shift of $\pi$ between $FTF_M$ and $FTF_\phi$ leads to the two terms compensating each other for low frequencies. All three terms have different phase slopes corresponding to the different convective time delays of the respective disturbances. The phase relation between the three terms consequently changes over the frequency. The local amplitude maximum at 300 Hz can be explained by constructive interference of all three mechanisms due to the low phase difference. The dominant mechanisms in the different frequency ranges can be identified from the phase plot. For $f < 180$ Hz, the phase of the overall model FTF follows the phase of $FTF_M$ while between 180 Hz and 300 Hz, the phase of the overall FTF agrees with $FTF_\phi$. For $f > 500$ Hz, the overall FTF has the same phase as $FTF_S$. The intermediate zone with almost constant phase characterizes the transition regime between 300 Hz

and 500 Hz. For high frequencies, the equivalence ratio contribution decays, and the FTF approaches the corresponding $NG_{pp}$ curve, which is dominated by $FTF_S$.

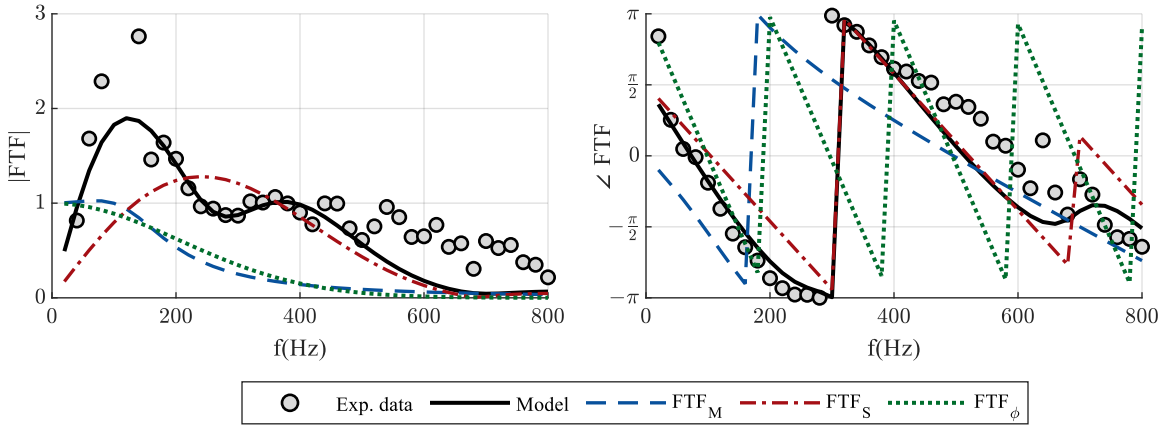


**Figure 7.5:** Comparison of model FTF and experimental data at the reference operating point of the $k_{70}$-configuration.

The model FTF at the reference operating point of the fully premixed kerosene configuration $k_{70}$ is given in Figure 7.5. Due to the same flame geometry, $FTF_M$ and $FTF_S$ are similar to the natural gas cases albeit with a slightly altered scaling of the $FTF_S$ term on the frequency axis resulting from the downstream shift of the kerosene flame. The fundamentally different shape of the overall FTF can therefore only be attributed to changes in the equivalence ratio contribution $FTF_\phi$. The phase drop is significantly larger than in the $NG_{tp}$ case. This represents the larger convective time delay of the equivalence ratio perturbations, which results from the slower droplet acceleration due to the higher inertia discussed in Section 4.3. As a consequence, the three mechanisms constructively interfere between 0 Hz and 200 Hz, which causes the formation of the strong amplitude maximum. Compared to the $NG_{tp}$ case, the $FTF_\phi$ contribution decays already at lower frequencies. This can also be attributed to the inertia of the droplets, which causes them to stop following the excitation if the excitation frequency becomes too high.

The comparison with the experimental data shows that the model underestimates the FTF amplitude in the frequency range between 80 Hz and

160 Hz. This is where the forcing amplitude was found to be exceptionally high, and nonlinear effects could be expected according to Section 6.2.

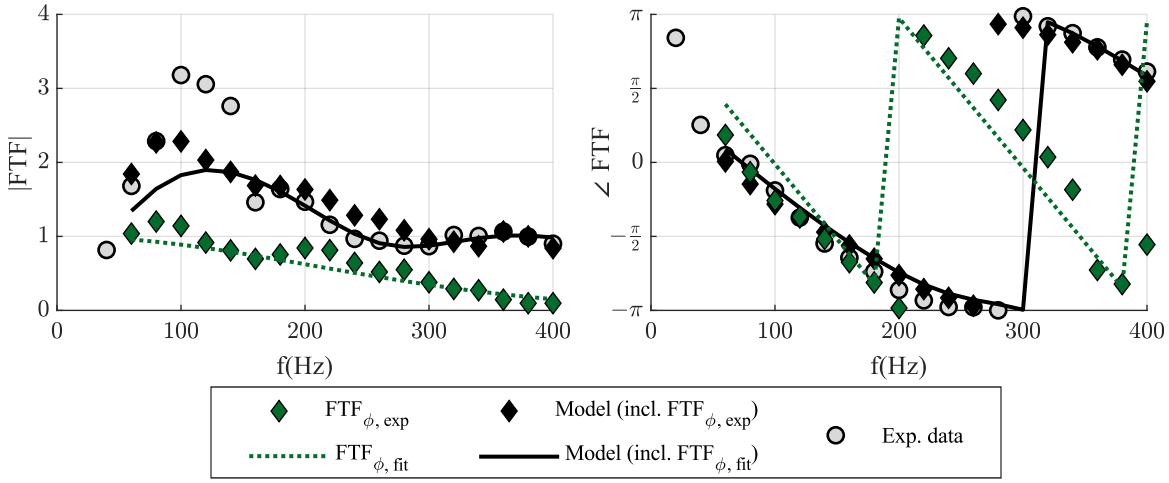


**Figure 7.6:** Comparison of experimentally determined [96] and fit-based $FTF_\phi$ at the reference operating point of the $k_{70}$-configuration.

In the following, the modeled contribution equivalence ratio fluctuations to the flame dynamics $FTF_\phi$ is validated by comparing it to experimental data from Vogel [96]. He used an optical method to determine $FTF_\phi$.

Figure 7.6 again shows the experimental data, the model FTF and the modeled equivalence ratio fluctuation term $FTF_\phi$ at the reference operating point of the $k_{70}$-configuration. Similar to the representation in Figure 7.5, the experimental data is given in grey circles, the model FTF is given as a black line, and the fitted $FTF_\phi$ is represented by a green dashed line. Additionally, the experimentally determined $FTF_\phi$ from [96] is given by green diamonds. It can be seen that the analytical model $FTF_\phi$ matches the experimental data very well in amplitude and phase. For low frequencies $f < 140$ Hz, the experimentally determined $FTF_\phi$ exceeds an amplitude of one, which the analytical $FTF_\phi$ model cannot reproduce. Black diamonds represent the FTF reconstruction using $FTF_M$, $FTF_S$ from the analytical model and the experimentally determined $FTF_\phi$. It can be

seen that the reconstructed FTF using the experimental $FTF_\phi$ matches the experimentally determined FTF slightly better than the fit-based reconstruction in the low frequency range $f < 140$ Hz.

Overall, the similarity between the experimental and fitted $FTF_\phi$ and the good agreement between the experimentally determined FTF and the model reconstruction using both variants of $FTF_\phi$ increase the confidence in the analytical model approach.

| $\dot{m}_{air}$ (g/s) | $\phi$ (-) | $\tau_{\phi,exp}$ (ms) | $\tau_{\phi,fit}$ (ms) | rel.error (%) | $\sigma_{\phi,exp}$ (ms) | $\sigma_{\phi,fit}$ (ms) | rel. error (%) |
|---|---|---|---|---|---|---|---|
| 25 | 0.575 | 5.82 | 5.65 | 3.0 | 1.21 | 1.08 | 10.5 |
| 25 | 0.675 | 4.78 | 5.06 | 5.9 | 0.72 | 0.77 | 7.4 |
| 25 | 0.775 | 4.40 | 4.66 | 6.0 | 0.68 | 0.60 | 11.6 |
| 20 | 0.675 | 5.86 | 5.88 | 0.3 | 1.01 | 1.01 | 0.2 |
| 30 | 0.675 | 4.10 | 4.22 | 2.8 | 0.39 | 0.58 | 47.4 |

**Table 7.1:** Comparison of experimentally determined [96] and fit-based values of $\tau_\phi$ and $\sigma_\phi$ for the $k_{70}$-configuration.

A comparison between the fitted and experimentally determined values of $\tau_\phi$ and $\sigma_\phi$ is given in Table 7.1 for all operating points where experimental data are available. It can be seen that the values match very well. The relative errors of $\tau_\phi$ are around 5%. For $\sigma_\phi$, the relative error differs strongly from case to case. However, the absolute errors are still very low.

### 7.2.2 Air Mass Flow Variation

The flame geometry parameters for $\dot{m}_{air}$ = 20 g/s $\dot{m}_{air}$ = 25 g/s and $\dot{m}_{air}$ = 30 g/s at $\phi = 0.675$ are given in Figure 7.7. As discussed in Section 5.3, the flame shape is self-similar over $\dot{m}_{air}$ in all configurations. The parameters, therefore, remain constant. The difference between the highest and lowest value is less than 5 mm in each dimension and for each configuration.

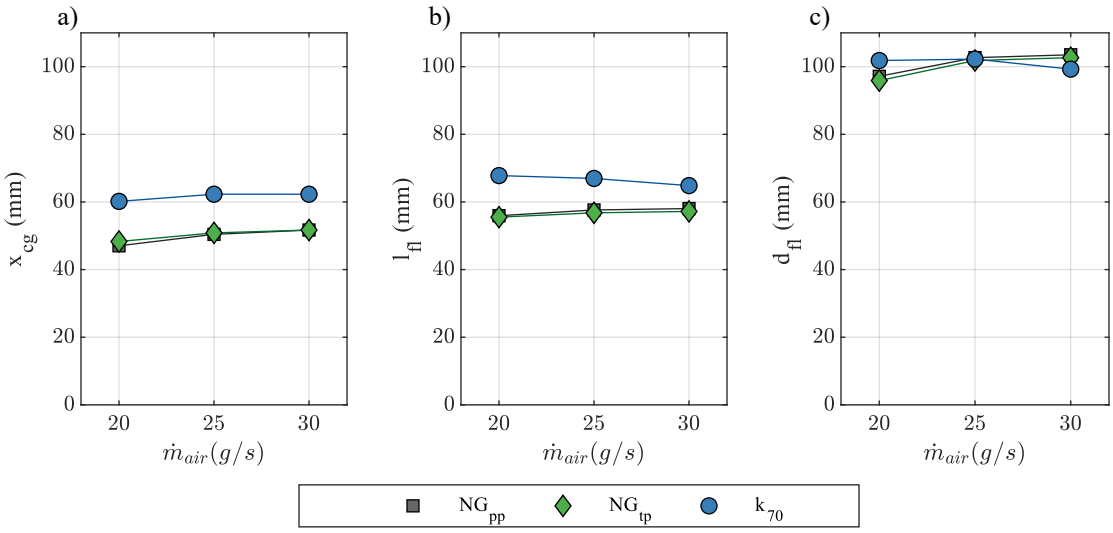


**Figure 7.7:** Flame geometry parameters of the $NG_{pp}$-, $NG_{tp}$-, $k_{70}$- and $k_{30}$-configuration for different main air mass flows at constant equivalence ratio $\phi$ = 0.675: (a) $x_{cg}$, (b) $l_{fl}$ and (c) $d_{fl}$.

The comparison between the experimentally determined FTFs and the model FTFs obtained from the geometry parameters is combined for all configurations in Figure 7.8. It can be seen that the model matches the experiment very well in all cases. Despite the flame geometry remaining constant, the model successfully reproduces the varying scaling of the FTFs along the frequency axis. This confirms the approach of scaling the model parameters inversely with $\dot{m}_{air}$.

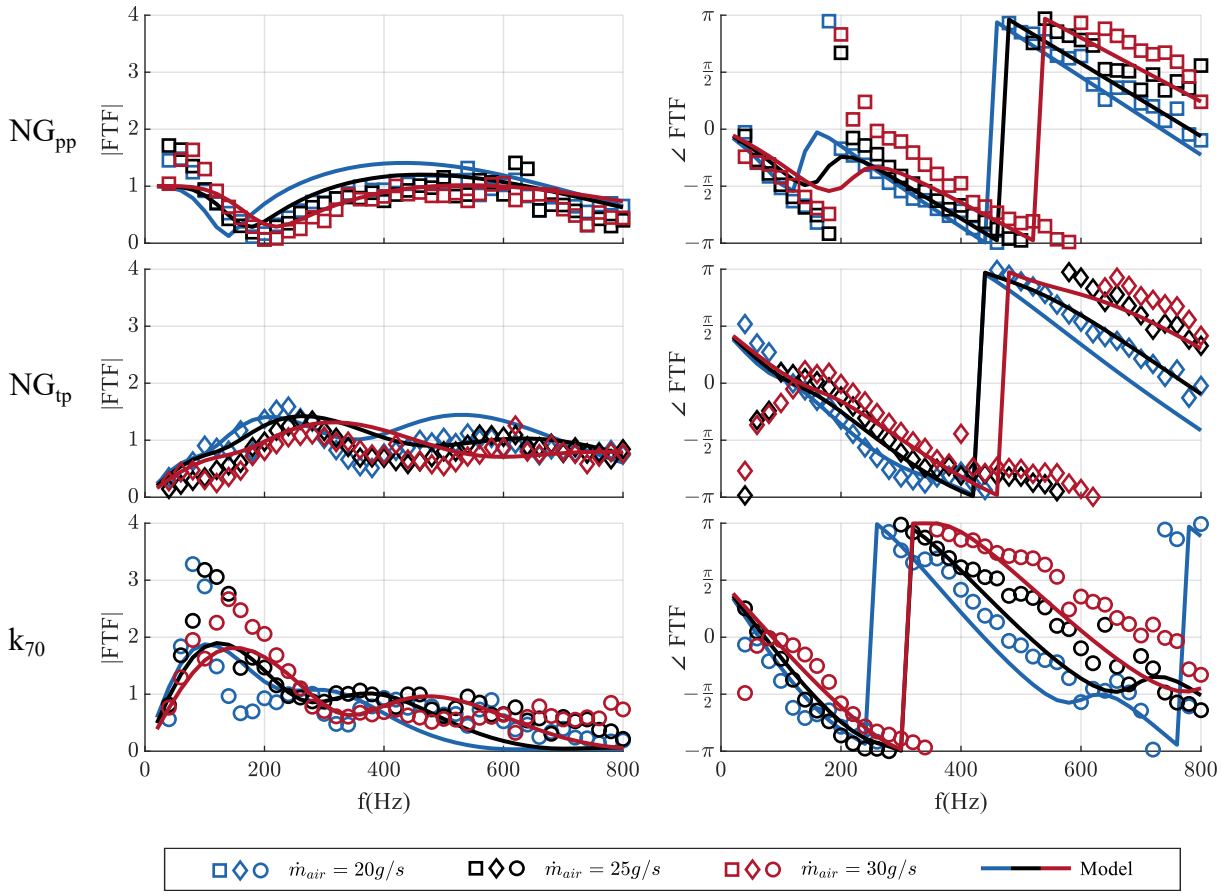


**Figure 7.8:** Comparison of model FTF and experimental data of the $NG_{pp}$-, $NG_{tp}$- and $k_{70}$-configuration for different air mass flows at constant equivalence ratio $\phi$ = 0.675.

### 7.2.3 Equivalence Ratio Variation

The flame geometry parameters for $\phi$ = 0.575, $\phi$ = 0.675 and $\phi$ = 0.775 at $\dot{m}_{air}$ = 25 g/s are given in Figure 7.9. With increasing equivalence ratio, the axial lift-off and the flame length decrease by around 20 mm between $\phi$ = 0.575 and $\phi$ = 0.775 for all configurations. The flame diameter decreases by about 30 mm.

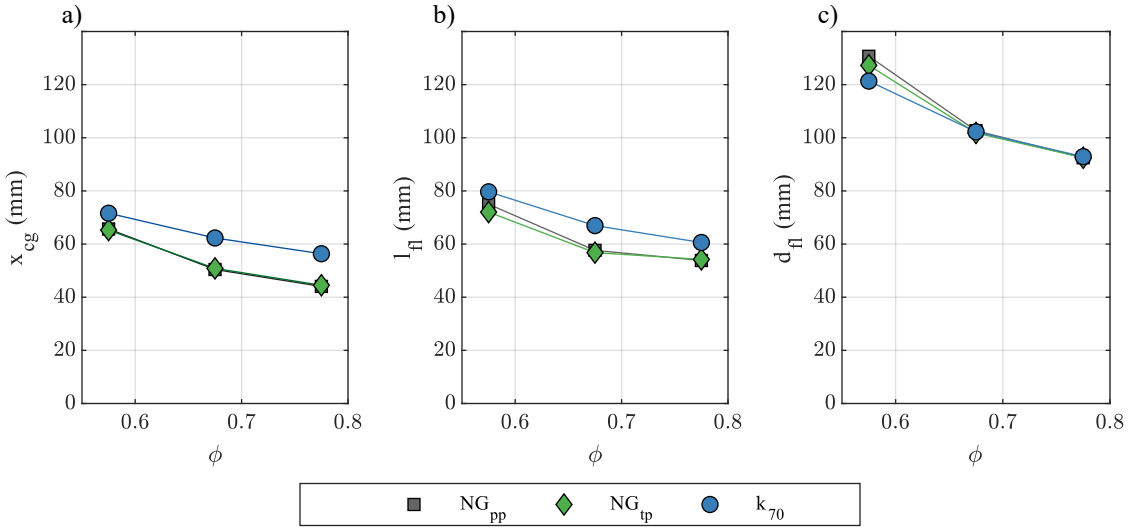


**Figure 7.9:** Flame geometry parameters of the $NG_{pp}$-, $NG_{tp}$- and $k_{70}$-configuration for different equivalence ratios at constant air mass flow $\dot{m}_{air}$ = 25 g/s: (a) $x_{cg}$, (b) $l_{fl}$ and (c) $d_{fl}$.

The implications of the observed flame geometry changes are discussed based on the results for the $k_{70}$-configuration given in Figure 7.10. The results for the two natural gas configurations are then combined in Figure 7.11 since the flame geometry changes, and therefore the implications on the FTFs are identical to the $k_{70}$ case.

Comparing the three model FTFs shows that the low frequency amplitude increase is mainly caused by a change of $FTF_S$. The increased flame length and axial lift-off in the leanest case $\phi$ = 0.575 shift the amplitude maximum of $FTF_S$ to lower frequencies and increase the phase slope. As a result, the magnitude of $FTF_S$ increases in the low frequency range, and the interference between $FTF_S$ and the other two mechanisms becomes

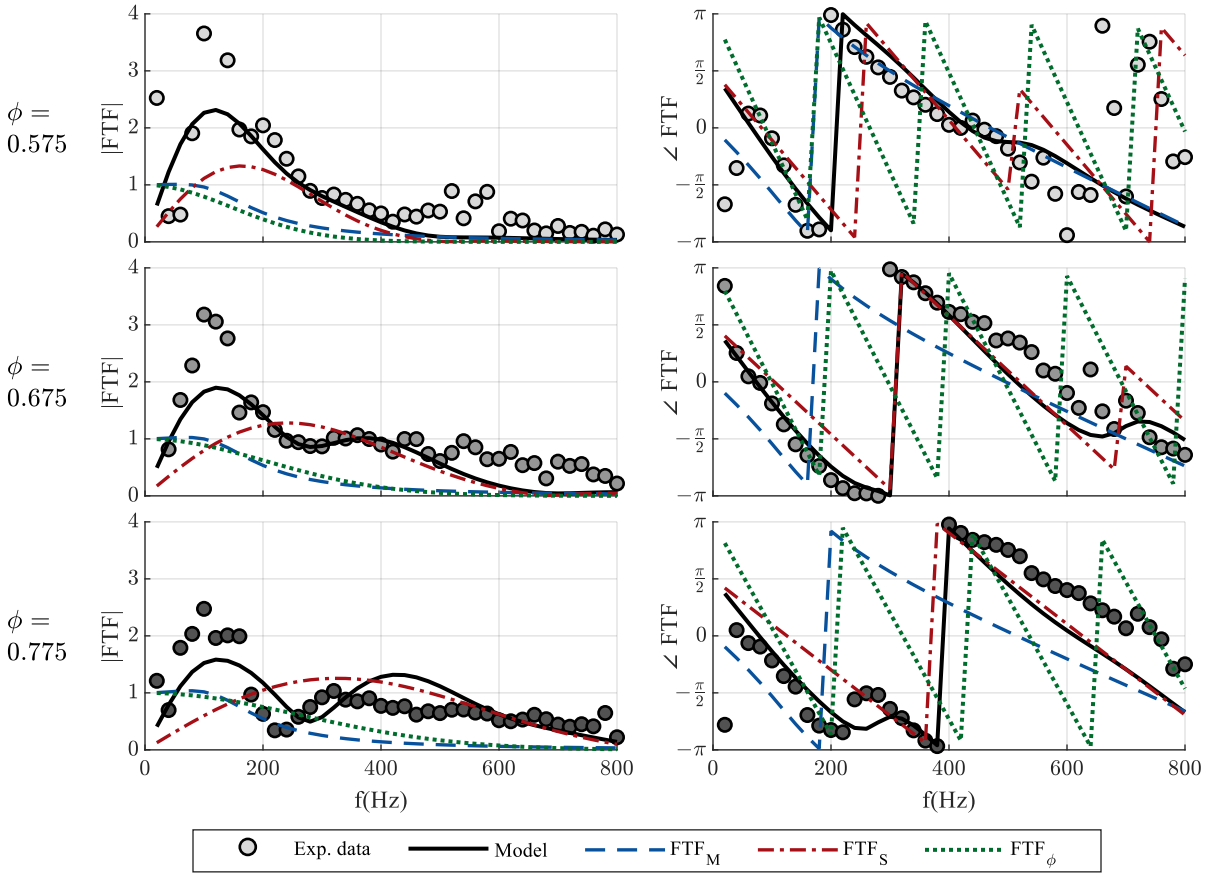


**Figure 7.10:** Comparison of model FTF and experimental data of the $k_{70}$-configuration for different equivalence ratios at constant air mass flow $\dot{m}_{air}$ = 25 g/s.

constructive. Comparing the FTFs for $\phi$ = 0.775 and $\phi$ = 0.575 reveals that this change almost doubles the low frequency amplitude peak. Although $FTF_M$ and $FTF_\phi$ also change with the equivalence ratio, this is far less significant.

The comparison of the modeled FTFs with the experimental data for the two natural gas configurations is given in Figure 7.11. Similar to the previously discussed $k_{70}$ case, the observed shift of the amplitude maximum can be mainly attributed to a change of the contribution of $FTF_S$. A slight deviation between the model and the experimental data can be observed in the leanest case. Here, the model fails to accurately reproduce the FTF

amplitude for low frequencies $f < 100$ Hz. However, as discussed in Section 5.3, the flame interacts with the combustion chamber walls in these cases. The relationship between flame geometry and FTF is, therefore, possibly influenced by additional effects which are not included in the model.

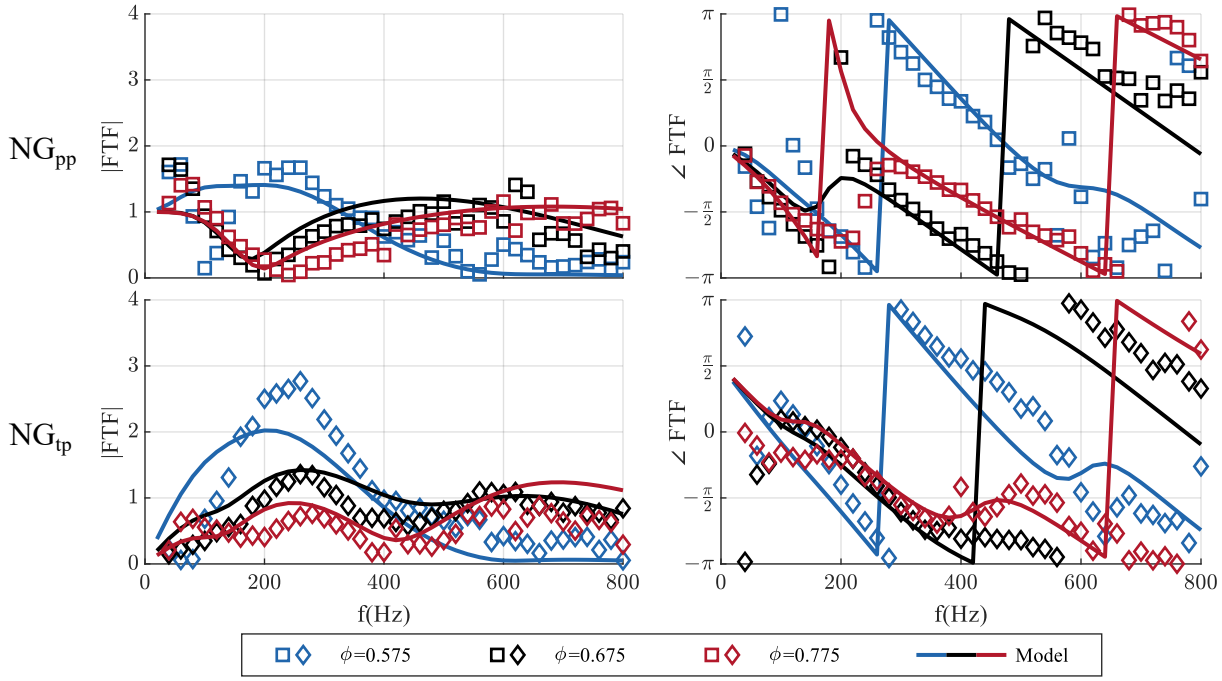


**Figure 7.11:** Comparison of model FTF and experimental data of the NG$_{pp}$- and NG$_{tp}$-configuration for different equivalence ratios at constant air mass flow $\dot{m}_{air} = 25$ g/s.

### 7.2.4 Atomizing Air Mass Flow Variation

The reconstruction and interpretation of the FTF sensitivity on the atomizing air mass flow in the k$_{70}$-configuration allows to specifically address the impact of FTF$_\phi$. As visible from Figure 7.12, the flame shape is insensitive to changes in the atomizing air mass flow over a wide range with less than 5 mm change in all parameters between $\dot{m}_{at} = 0.75$ g/s and $\dot{m}_{at} = 1.13$ g/s. This means that FTF$_M$ and FTF$_S$ remain constant, and all changes in the FTF can be attributed to FTF$_\phi$. The lowest atomizing air

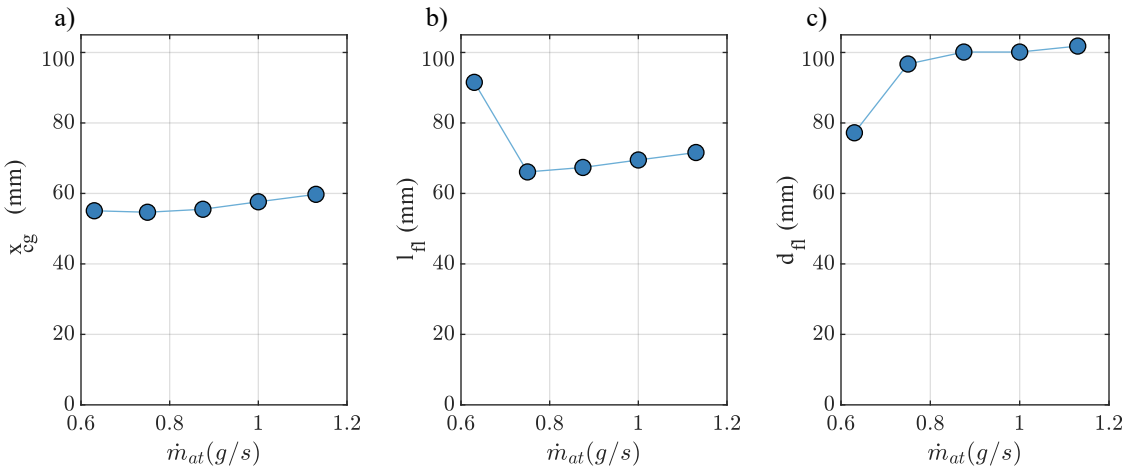


**Figure 7.12:** Flame geometry parameters of the $k_{70}$-configuration for different atomizing air mass flows at constant air mass flow $\dot{m}_{air}$ = 25 g/s and constant equivalence ratio $\phi$ = 0.675: (a) $x_{cg}$, (b) $l_{fl}$ and (c) $d_{fl}$.

mass flow case is excluded from the following analysis because $d_{fl}$ and $l_{fl}$ differ from the values at higher $\dot{m}_{at}$.

The FTF models for the $k_{70}$-configuration with various atomizing air mass flows are given in Figure 7.13. The model matches the experimental data well, thus justifying the approach of scaling the model parameters of $FTF_\phi$ with the ALR. It can be seen that the amplitude decay of $FTF_\phi$ is only marginally changed with the atomizing air mass flow, and the observed changes in the FTF can therefore be attributed to the changes in the $FTF_\phi$ phase. The low atomizing air mass flow case denoted in the upper row is associated with coarse droplets. As pointed out in Section 4.3, this leads to a higher value of $\tau_\phi$ and thus a steeper phase drop with frequency. Between 100 Hz and 200 Hz, the phases of $FTF_\phi$ and $FTF_M$ are very similar but differ from the phase of $FTF_S$ by almost $\pi$. This leads to the formation of a local amplitude minimum at 200 Hz.

With increasing atomizing air mass flow and thus smaller droplets, the phase of $FTF_\phi$ drops less steep with frequency. This leads to constructive interference of $FTF_\phi$ and $FTF_S$ at 200 Hz in the highest atomization air

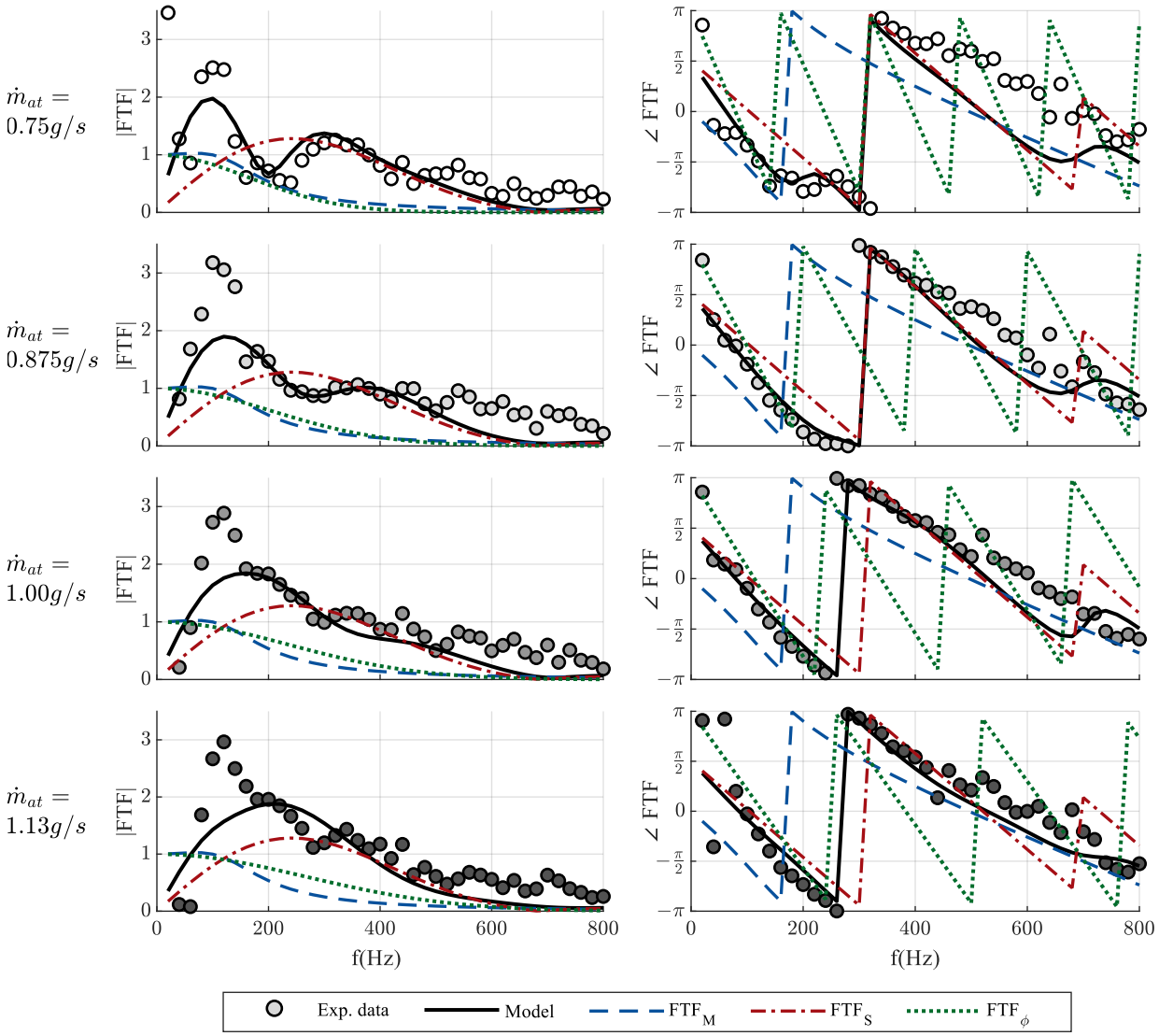


**Figure 7.13:** Comparison of model FTF and experimental data of the $k_{70}$-configuration for different atomizing air mass flows at constant air mass flow $\dot{m}_{air}$ = 25 g/s and constant equivalence ratio $\phi$ = 0.675.

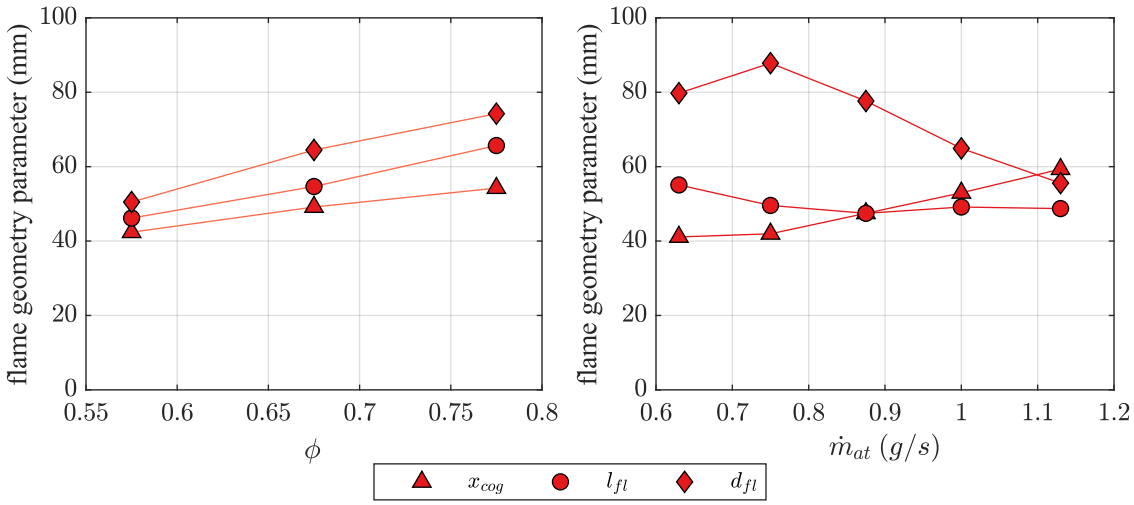


**Figure 7.14:** Flame geometry parameters $x_{cg}$, $l_{fl}$ and $d_{fl}$ of the $k_{30}$-configuration over (a) equivalence ratio and (b) atomizing air mass flow.

mass flow case, resulting in an amplitude value of |FTF| = 2.

## 7.3 $k_{30}$-Configuration

Applying the scaling rules obtained from the already discussed three cases directly to model the FTFs in the $k_{30}$-configuration does not produce any significant results. This is not surprising since the fundamental correlations between the burner, flame, and velocity field in the $k_{30}$-configuration differ significantly from those in the other three cases, as discussed in Chapter 5. However, also deriving a specialized set of scaling rules solely for the $k_{30}$-configuration was unsuccessful. This observation suggests that the dependencies of the mechanisms on the flame geometry are not the only differentiating factor in the partially diffusive $k_{30}$-configuration. Instead, the flame response is driven by distinct mechanisms that are primarily influenced by the incomplete fuel distribution and by the local atomizer flow field, rather than by the flame shape.

The two observations that contradict the applicability of the model in the

$k_{30}$-configuration are:

- The FTF does not change with the flame geometry. As visible from Figure 7.14, the flame geometry parameters change considerably with the operating point. At the same time, the FTF changes only marginally and, especially in the high frequency range, remains constant, as discussed in Chapter 6 based on Figures 6.5-6.10. The high frequency range was found to be dominated by the swirl fluctuation mechanism $FTF_S$ in the other configurations. This mechanism showed the highest sensitivity on the flame geometry. This suggests that mechanisms are present in the $k_{30}$-configuration that are independent of the flame shape.
- As shown in Figure 6.6, the $k_{30}$-FTF amplitudes of different air mass flow rates are not similar when plotted over $Sr$. From a modeling point of view, this contradicts the approach of scaling the model parameters inversely with the mass flows. From a physical point of view, this indicates that the driving mechanisms are not of convective nature.

## 7.4 Conclusions from the Analytical Model Analysis

In this chapter, an analytical FTF model was applied. A single parametric scaling rule set based on the flame geometry was derived for the $NG_{pp}$-, $NG_{pp}$- and $k_{70}$-configuration. The model was used for the analysis of experimentally determined FTF. From this, the following conclusions were drawn:

- The existence of a single parametric scaling rule set that allows to reproduce the FTFs for the three different configurations strongly suggests that the underlying mechanisms are the same for all three configurations. The only major difference between the $k_{70}$-configuration and the natural gas configurations is the increased inertia of the

droplets, which leads to a higher convective time delay of the equivalence ratio fluctuations. Besides this, the fuel type does not have an impact on the FTF as long as the spray is fully evaporated at the combustion chamber entry.

- The FTF trends for a variation of the equivalence ratio could be mainly attributed to changes in the swirl fluctuation contribution $FTF_S$.
- Changing the atomization quality affects the convective time delay of the equivalence ratio fluctuations, even if the flame shape remains unchanged. This can lead to changes in the FTF at constant flame shape and position.
- The fact that a similar set of parametric scaling rules could not be derived for the $k_{30}$-configuration suggests that the mechanisms and dependencies contributing to the FTF trends in the partially diffusive $k_{30}$-configuration fundamentally differ from the three other configurations.

# 8 FTF Prediction

Optimizing the operating point of a given system with regard to its thermoacoustic characteristics requires a considerable amount of FTF datasets for different operating conditions. This causes a high effort and high costs. Accurately predicting the FTF for a given operating point significantly reduces the effort for gaining the required datasets.

This chapter applies the analytical model from the previous chapter to predict the FTF for a given operating point. For this, the method is extended as schematically shown in Figure 8.1. Experimental flame image data and the corresponding operating conditions are provided to the POD for a relatively small number of operating points. From this, the POD is able to calculate generic flame images for any given operating point. These images then serve as input for the model described in the previous chapter. This method can be advantageous for generating a larger database or extracting information about a specific operating point in situations where the available data on flame geometry and FTF is limited to only a few operating conditions. However, it is not applicable if no a priori datasets are available. The approach is demonstrated in the following by reproducing FTFs for natural gas operation from Bade [6]. The FTFs were recorded at the same test rig and using the same burner hardware as in this thesis. Therefore, the flame images given in Section 5.3 are used as the database for the POD, and the flame-geometry-dependent parameter scaling rules derived in the previous chapter are applied without change.

POD is a mathematical technique used to reduce the dimensionality of large datasets while preserving their key features. The concept of POD is known under several names in different application fields [98]. It was first introduced in fluid dynamics to study the behavior of turbulent

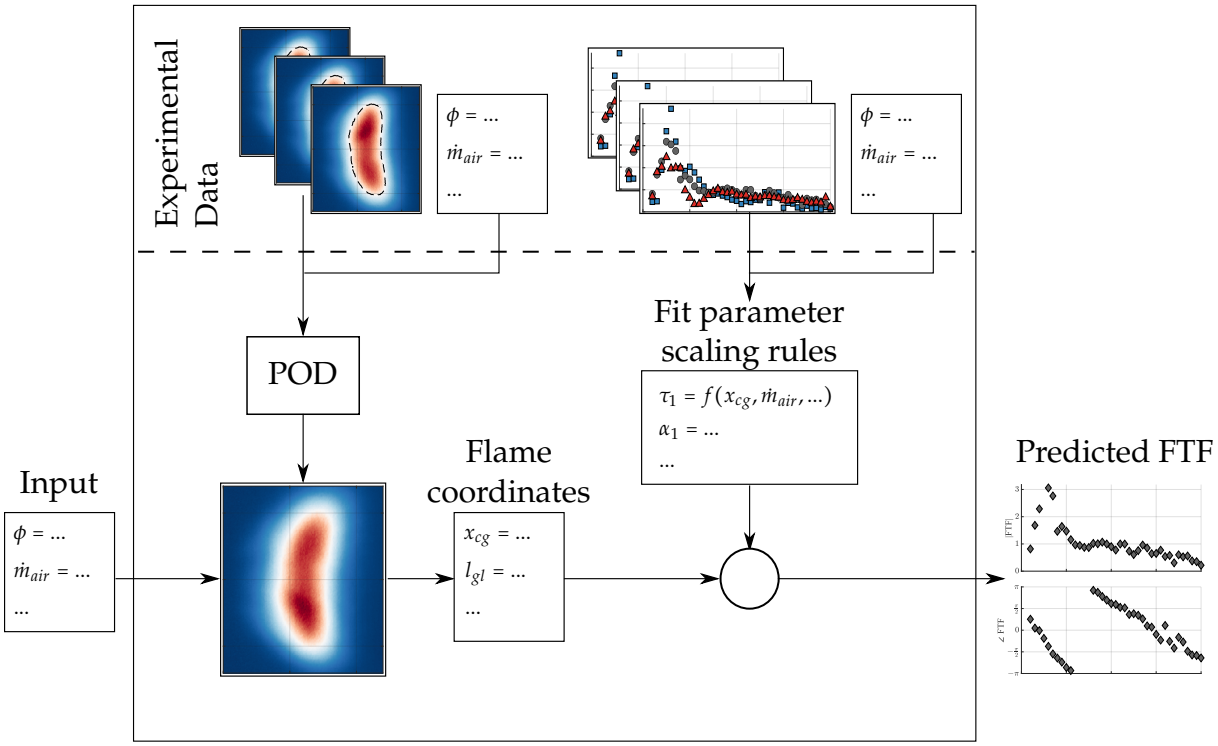


**Figure 8.1:** Schematic representation of the FTF prediction workflow, including POD.

flows and identify the most important flow structures [57, 64, 68]. In recent years, the POD has found wide application in other fields, such as image processing, where it is mainly referred to as principal component analysis [42]. In the context of combustion research, Marquez has applied POD to analyze the spatio-temporal unmixedness of fuel and air in multi-burner systems [58]. Zahn demonstrated that POD can be applied to directly determine the FTF at a given operating point [99]. This methodology offers a more straightforward means of generating FTF data. However, the presented approach of only applying the POD for generating flame images provides the advantage of maintaining causality to the flame geometry, thereby enabling a more comprehensive understanding of the underlying mechanisms.

The procedure can be described as a generalized Fourier series expansion, in which a given function is approximated based on trigonometric approach functions. However, unlike the Fourier series, an optimal

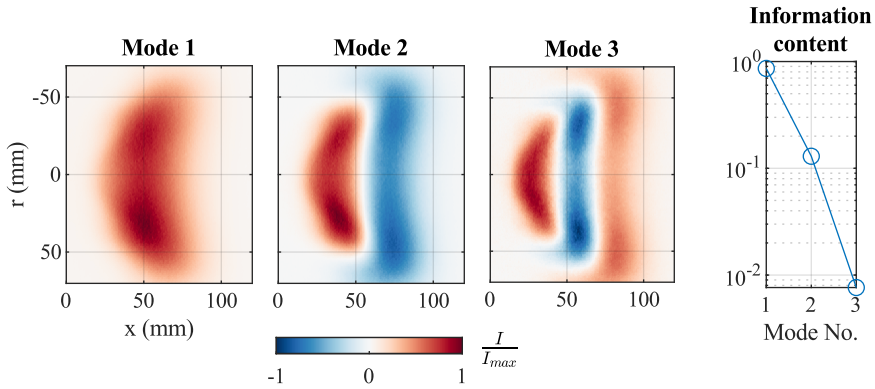


**Figure 8.2:** Flame image POD modes of the $NG_{pp}$-configuration: (a) Intensity distribution and (b) mode information content.

orthogonal basis is chosen instead of trigonometric functions. A relatively small set of measured data $X$ is used as input. Based on those data, the POD generates a set of orthonormal basis functions $\Phi_i$, called modes and corresponding operating point-dependent mode coefficients $c_i(\phi, \dot{m}_{air})$ [57]. By retaining only the $N$ most important basis functions, the POD can significantly reduce the model order while maintaining a high level of accuracy. The reduced order data $X_{POD}$ for any desired operating point can thus be approximated using the following linear combination:

$$X(\phi, \dot{m}_{air}) \approx X_{POD}(\phi, \dot{m}_{air}) = \sum_{i=1}^{N} c_i(\phi, \dot{m}_{air})\Phi_i. \tag{8.1}$$

More detailed information on POD can be found in [10, 42, 57].

The methodology is employed in the following for reproducing the FTF from Bade [6]. The process is illustrated in detail using the reference operating point as an example. The reference operating point is at $\lambda = 1.4$ and $P_{th} = 50$ kW which translates to $\phi = 0.714$ and $\dot{m}_{air} = 25$ g/s. The normalized flame images for perfectly and technically premixed natural gas combustion discussed in Section 5.3 serve as input for the POD.

The first three modes generated by the POD are shown in Figure 8.2 along with the corresponding relative information content. It can be seen that the third mode already contains less than 1% of the overall information.

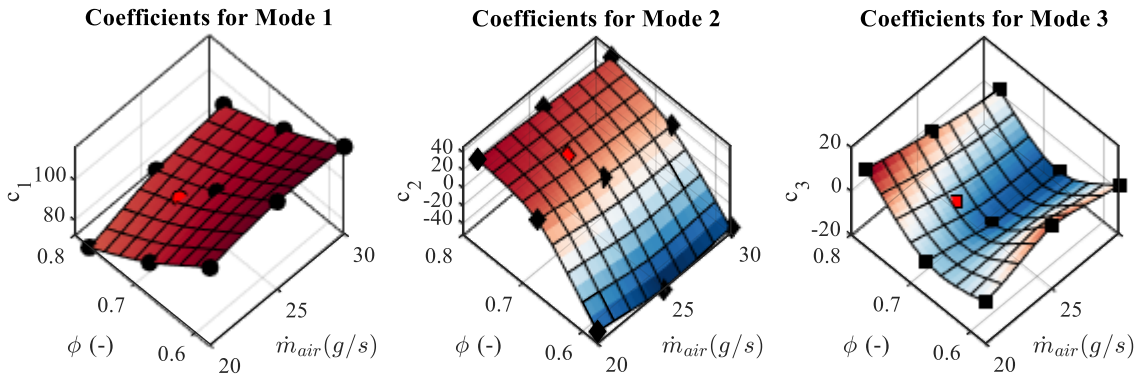


**Figure 8.3:** Evaluated POD coefficients of the $NG_{pp}$-configuration and fitted coefficient for flame image reconstruction at $P_{th}$ = 50 kW, $\lambda$ = 1.4 ($\dot{m}_{air}$ = 24 g/s, $\phi$ = 0.741).

All following modes have fever information content and can therefore be omitted. The colorbar is normalized to the maximum intensity and centered around zero for all three modes. Positive values are indicated in red color and negative values in blue color. The first mode only contains positive intensity values. It can be interpreted as the mean flame image over all operating points. The second mode is positive towards the flame root and negative in the downstream direction. It can be interpreted as a displacement along the streamlines. The third mode is positive at the flame's upstream and downstream boundaries and negative at the middle. It can be thought of as a variation of the axial flame length. According to Equation 8.1, the modes are weighted by mode-individual, operating point-dependent coefficients $c_i$ before they are summed up to obtain the reduced order flame images.

The coefficients $c_1 - c_3$ corresponding to the modes 1 to 3 are plotted in Figure 8.3. The coefficients corresponding to the experimental input data sets are given by filled black symbols. A red symbol in all three plots gives the interpolated coefficient for the desired operating point. The color of the interpolated surface again indicates positive values in red and negative values in blue. As expected from the interpretation as the

mean image, the coefficient corresponding to mode 1 is always positive. The coefficient $c_2$ is independent of $\dot{m}_{air}$ but strongly depends on $\phi$. For high values of $\phi$, $c_2$ is positive and negative for low values of $\phi$. This means that for high values of $\phi$, the flame moves towards the burner outlet, while the negative sign of $c_2$ for low values of $\phi$ means that the movement indicated by the mode shape in Figure 8.2 is inverted, and the flame is therefore shifted downstream. The coefficient $c_3$ shows no clear tendency. It can be interpreted as an elongation of the flame for high and low values of the equivalence ratio. However, this mode only contains less than 1% of the information, and the effect is, therefore, only very weak.

The flame image is then obtained by summing up the weighted modes. The modes and POD coefficient planes from Figures 8.2 and 8.3 remain identical for all operation points, and only the fitted coefficients are adapted. The flame coordinates are extracted as described in Section 4.1.1 and used as input for the FTF model.

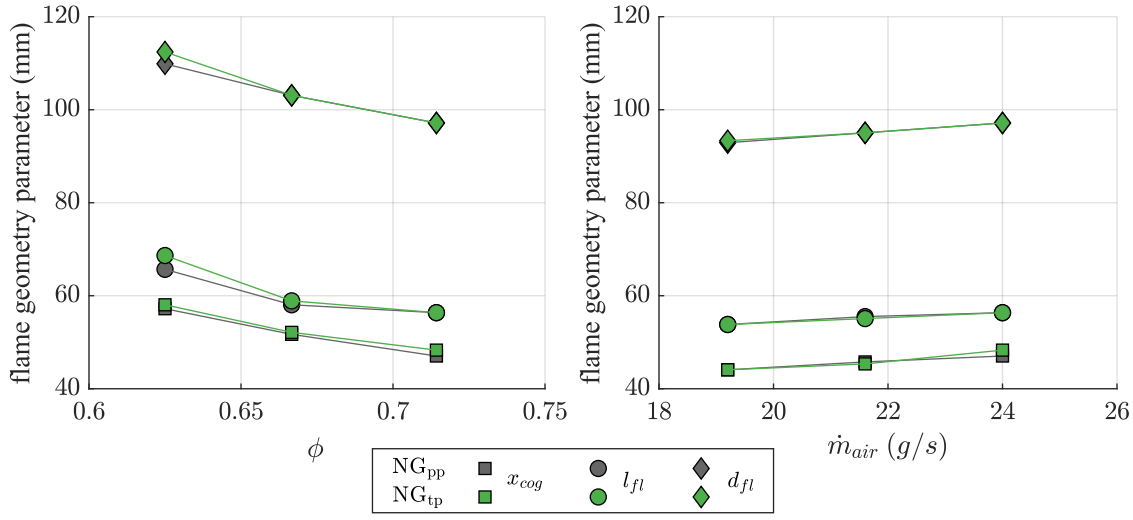


**Figure 8.4:** Predicted flame geometry parameters $x_{cg}$, $l_{fl}$ and $d_{fl}$ of the NG$_{pp}$- and NG$_{tp}$-configuration for (a) different equivalence ratios at constant thermal power $P_{th}$ = 50 kW and (b) different air mass flows at constant equivalence ratio $\phi$ = 0.714.

The resulting flame parameter trends for the operating range specified in [6] are plotted in Figure 8.4. In contrast to the operating range from this thesis, the equivalence ratio is varied at constant thermal power instead of constant air mass flow. The air mass flow, therefore, decreases with increasing equivalence ratio. No notable difference is visible between the parameters for the $NG_{pp}$- and $NG_{tp}$-configuration. All parameters decrease as the equivalence ratio increases and are insensitive towards the air mass flow. This is in line with the experimental results from Figures 7.9 and 7.7.

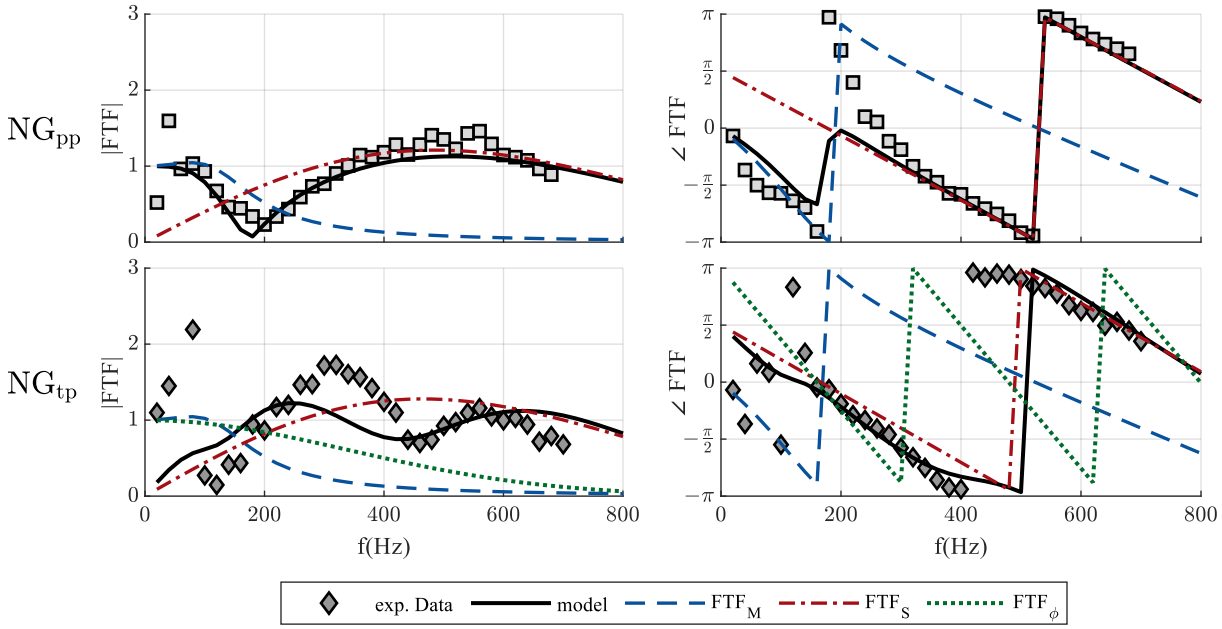


**Figure 8.5:** Comparison of predicted FTF and experimental data of the $NG_{pp}$- and $NG_{tp}$-configuration from Bade [6] at $P_{th}$ = 50 kW, $\lambda$ = 1.4 ($\dot{m}_{air}$ = 24 g/s, $\phi$ = 0.741).

The resulting predicted FTFs for perfectly and technically premixed natural gas combustion at $P_{th}$ = 50 kW and $\lambda$ = 1.4 are compared to the experimental data from Bade [6] in Figure 8.5. The experimental data are approximated very well by the prediction in amplitude and phase. The prediction results for other operating points in the range specified by Bade [6] can be found in Appendix A.3.

It can thus be concluded that the applied method is capable of predicting FTFs for a given operating point. This technique may be beneficial in scenarios where there is a need to generate a larger database or extract information about a specific operating point from a limited amount of data on flame geometry and FTF for a few operating conditions. Compared to other methods, the knowledge of flame geometry and FTF composition generated besides the FTF itself is valuable additional information and can be helpful in interpreting the resulting FTF.

# 9 Summary and Conclusion

The option of burning liquid fuels increases the fuel flexibility of gas turbines. However, gas turbines must comply with emission regulations, which requires operating under lean premixed conditions. Unfortunately, such conditions may lead to thermoacoustic instabilities. While there has been considerable research on these instabilities in lean premixed natural gas combustion, studies on lean premixed liquid fuel combustion are limited. The aim of this work was to contribute to this topic by examining the longitudinal thermoacoustic oscillations in an atmospheric lean premixed gas turbine combustor. Two liquid fuel configurations with different degrees of premixing were compared with natural gas as reference. Flame transfer functions were used to quantify flame dynamics, the potential driver of thermoacoustic instability.

Experiments were carried out in an atmospheric single burner test rig using a modular swirl burner, which was retrofitted with a twin fluid nozzle for kerosene injection. The axially movable nozzle installation allowed for realizing different degrees of fuel-air premixing in liquid operation. In total, four different configurations were investigated. Natural gas combustion in perfectly and technically premixed mode served as references. In liquid operation, a fully premixed configuration with a long premixing length and a partially premixed configuration with a short premixing length were investigated.

First, the stationary combustion characteristics were investigated. $NO_x$ emission measurements, stationary OH*-chemiluminescence flame images, and liquid fuel droplet size measurements were presented for varying air mass flow rates, equivalence ratios, and atomizing air mass flow rates. The results revealed fundamental differences in the stationary characteristics of the two liquid configurations:

- The fully premixed liquid fuel configuration was found to be very similar to the two natural gas configurations. All three configurations revealed similar, disc-like flame shapes and low $NO_x$ emissions. Based on droplet size and $NO_x$ emission measurements, it was concluded that the fuel entered the combustion chamber in a fully evaporated state. The flame was, therefore, mainly determined by the flow field in the combustion chamber. Flame shape and $NO_x$ emissions were independent of the vaporization quality at the nozzle.
- The behavior observed in the partially premixed configuration was notably different from the observed behaviour for the other three configurations. Due to the short premixing length, the fuel was not fully evaporated nor distributed over the entire cross section at the burner outlet. The flame shape was mainly determined by inhomogeneous radial fuel distribution. This resulted in a radially more compact flame shape and a more diffusive combustion character, which was indicated by the increased $NO_x$ emissions. The flame shape trends in response to variations of the equivalence ratio $\phi$ and atomizing air mass flow $\dot{m}_{at}$ were opposed between the partially premixed liquid fuel configuration and all other configurations.

The longitudinal thermoacoustic properties of the burner and the flame were discussed next. The acoustic scattering matrices of the burner, both with and without liquid fuel injection nozzle, were compared with each other in order to prove that the acoustic scattering properties remained unaffected by the installation of the nozzle. Subsequently, flame transfer functions were presented for the various operating conditions.

A high maximum amplitude in the low frequency range for all operating points characterized the flame transfer functions of the fully premixed liquid fuel configuration. In contrast, the partially premixed configuration exhibited low amplitudes throughout the operating range.

In response to variations of the operation parameters, the fully premixed kerosene configuration showed the same behaviour as the two natural

gas configurations. In contrast, the partially premixed liquid fuel configuration exhibited a fundamentally different behaviour. The atomizing air affected the flame transfer function in both liquid fueled configurations.

An analytical model was applied to gain further insight into the flame transfer function's composition from different flame response mechanisms. The different feedback mechanisms were modeled individually and then superposed. Based on the experimental observations, it was assumed that the flame response mechanisms were similar for the fully premixed kerosene configuration and the two natural gas cases. Most of the model parameters were consequently chosen identical for the three configurations. The good agreement with the experimental data over the entire operating range for three different configurations allowed for physically interpreting the model-based decomposition into the different flame response mechanisms. The key findings from these investigations can be summarized as follows:

- The existence of a single model parameter set that allowed to reproduce the flame transfer functions for the three different configurations strongly suggested that the underlying mechanisms were the same for all three configurations. Of particular importance here were the equivalence ratio fluctuations caused by the acoustic field at the point of fuel injection in the case of technical premixing. Unlike the gas, which immediately adjusted to the mean flow field after injection, the liquid droplets required extra acceleration time due to their inertia. This changed the phase relation between the equivalence ratio fluctuations and the other mechanisms contributing to the flame dynamics. This observation could explain the differences observed between the fully premixed liquid fuel configuration and the natural gas cases.

- Changing the atomization quality affected the convective time delay of the equivalence ratio fluctuations. This changed the flame transfer function, even though the flame shape and position remained constant.

- A consistent model parameter set could not be derived for the partially premixed configuration. This suggested that the mechanisms and dependencies contributing to the flame dynamics in the partially premixed configuration fundamentally differed from the three other configurations.

Finally, the derived analytical model was applied to predict flame transfer functions based on the operating conditions. The method was validated by reproducing experimental data from preceding work. A good agreement between the predicted flame transfer functions and the experimental validation data could be achieved.

While the measured flame transfer functions could be decomposed and the resulting components attributed to different flame response mechanisms for natural gas and kerosene in fully premixed operation, this could not be achieved in the partially premixed configuration. Thus, future work should aim to improve the understanding of the underlying mechanisms at lower degrees of premixing. One key point for this is the detailed investigation of the interaction between droplets, acoustic field, and heat release rate. To achieve this, performing phase-resolved measurements of droplet diameters and velocities, along with the oscillating heat release field, would be advantageous.

# A Appendix

## A.1 Droplet Evaporation Time Estimation

The evaporation time of a single spherical droplet can be estimated by applying the $D^2$ law:

$$\tau_{evap} = d^2/K. \tag{A.1}$$

The evaporation constant K depends on material properties and conditions of the liquid (index l) and gaseous (index g) phase [93]:

$$K = \frac{8\lambda_g}{\rho_l c_{p,g}} lnB + 1. \tag{A.2}$$

$\lambda$ denotes the thermal conductivity here and $c_p$ is the specific isobaric heat capacity. B is the transfer number, which is defined as:

$$B = \frac{c_{p,g}\left(T_\infty - T_{boil}\right)}{\Delta h} \tag{A.3}$$

with $\Delta h$ being the specific evaporation enthalpy.

Since kerosene is not a pure substance but a mixture of substances, it does not have a boiling point but a boiling range. The boiling temperature was thus defined as the boiling temperature at 50% recovered. According to the supplier datasheet, this is $T_{boil} = 463.78\ K$. The other values were taken from [73] for the closest matching value $T = 450\ K$ at atmospheric

pressure:

$$\rho_l = 678.9 \frac{kg}{m^3}$$
$$c_{p,g} = 2.753 \frac{kJ}{kgK}$$
$$\lambda_g = 0.09203 \frac{W}{mK}$$
$$\Delta h = 265.1 \frac{kJ}{kg}.$$

The surrounding temperature was assumed to be equivalent to the preheating temperature of the plenum, $T_\infty = 573.15\ K$.

The calculation does not take into account the increased heat transfer in a convective flow [9]. It can therefore be assumed that the calculation overestimates the evaporation time. Thus, the calculated value can be seen as an upper boundary.

## A.2 FTF Validation Using OH*-based Measurements in the $NG_{pp}$-Configuration

To validate the FTFs, the MMM-based FTF data of the $NG_{pp}$-configuration are compared to FTF obtained from a second method. As discussed in Section 4.2.2, this method relies on the pressure measurements in the plenum which are also used for the MMM and simultaneously recorded OH*-chemiluminescence time series of the flame. Figures A.1 and A.2 show that the results of the two different methods match very well over the entire operating range.

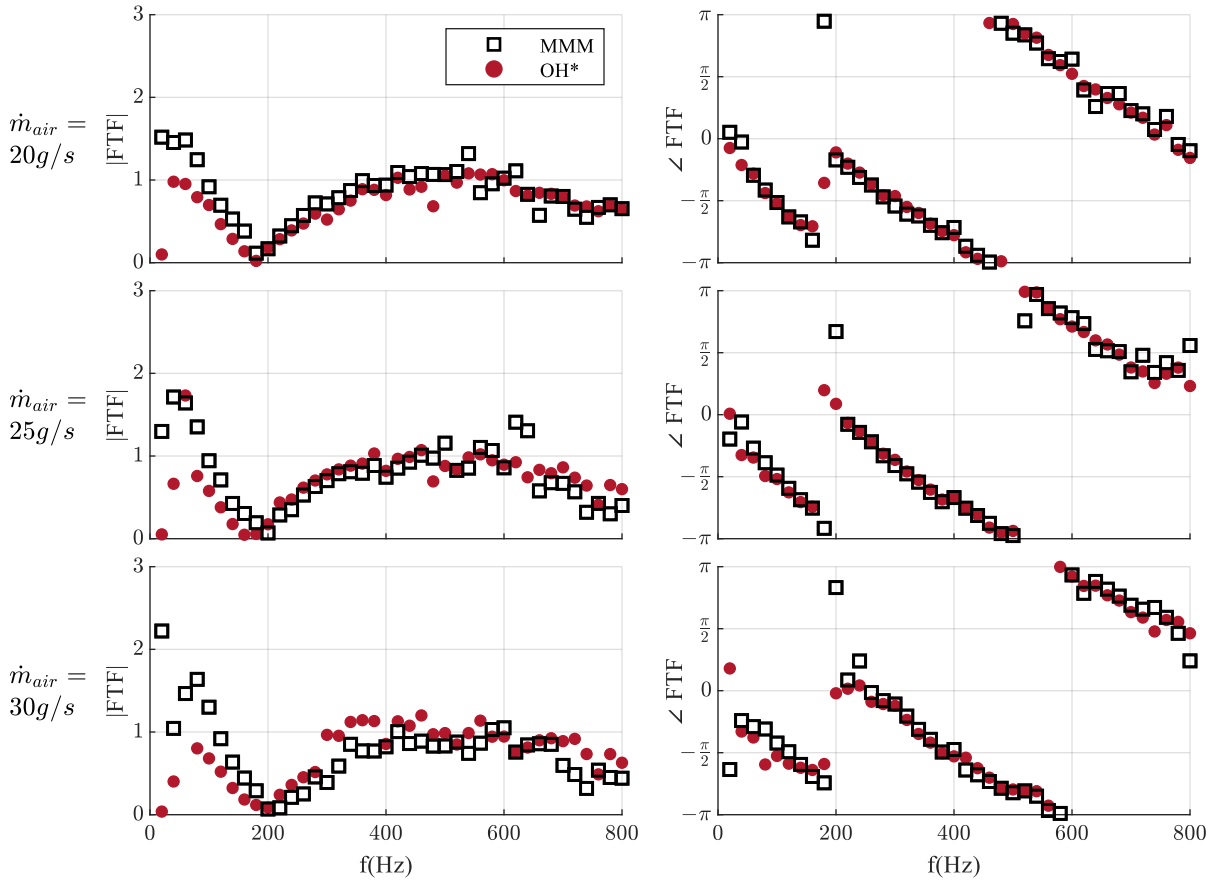


**Figure A.1:** Comparison of MMM-based FTF and OH*-based FTF of the $NG_{pp}$-configuration for different air mass flows at constant equivalence ratio $\phi$ = 0.675.

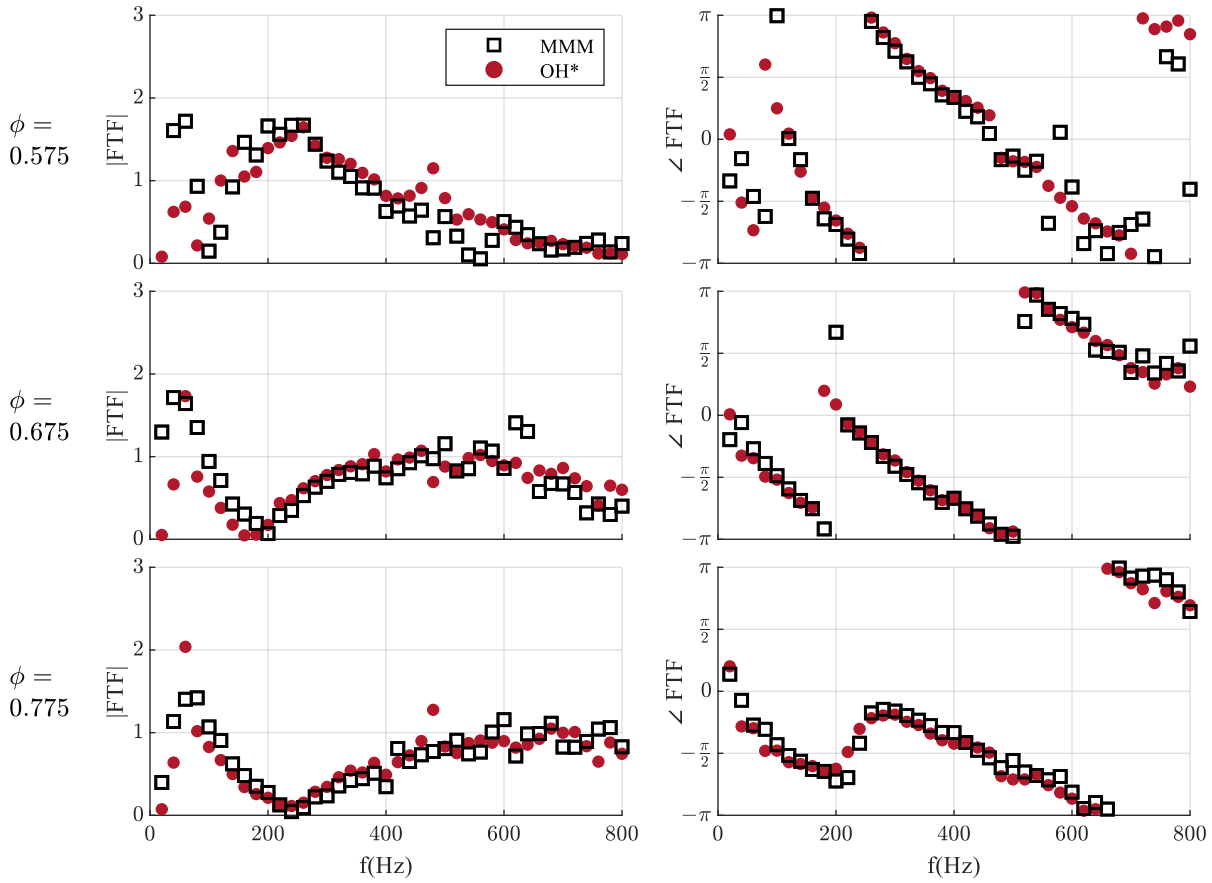


**Figure A.2:** Comparison of MMM-based FTF and OH*-based FTF of the $NG_{pp}$-configuration for different equivalence ratios at constant air mass flow $\dot{m}_{air} = 25\,g/s$.

## A.3 FTF Prediction for the Operating Range from Bade [6]

This section presents the predicted FTF according to the procedure outlined in Chapter 8 for the entire operating range specified by Bade [6]. Figure A.3 shows the predicted FTF for the thermal power variation, and Figure A.4 for the equivalence ratio variation.

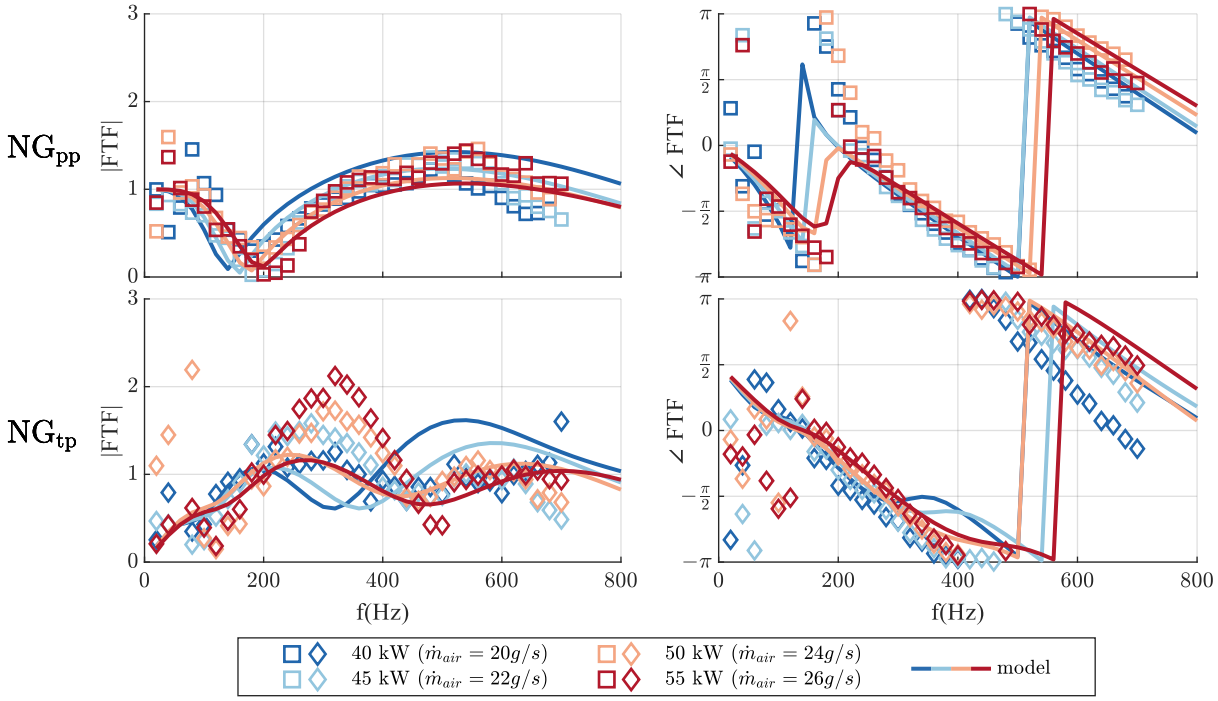


**Figure A.3:** Comparison of predicted FTF and experimental data of the NG$_{pp}$- and NG$_{tp}$-configuration from Bade [6] for different thermal power levels at constant equivalence ratio $\lambda = 1.4$ ($\phi = 0.714$).

In general, the predicted FTFs and the experimental data agree very well, particularly for the NG$_{pp}$-configuration. Only in the leanest case the prediction deviates from the experimental data. In the NG$_{tp}$-configuration, the amplitudes deviate slightly more. Since this deviation is specific to the NG$_{tp}$-configuration, it can be concluded that it is primarily caused by the equivalence ratio fluctuation term. Nevertheless, the amplitudes are still reproduced qualitatively correct, and the phases closely match the experimental data.

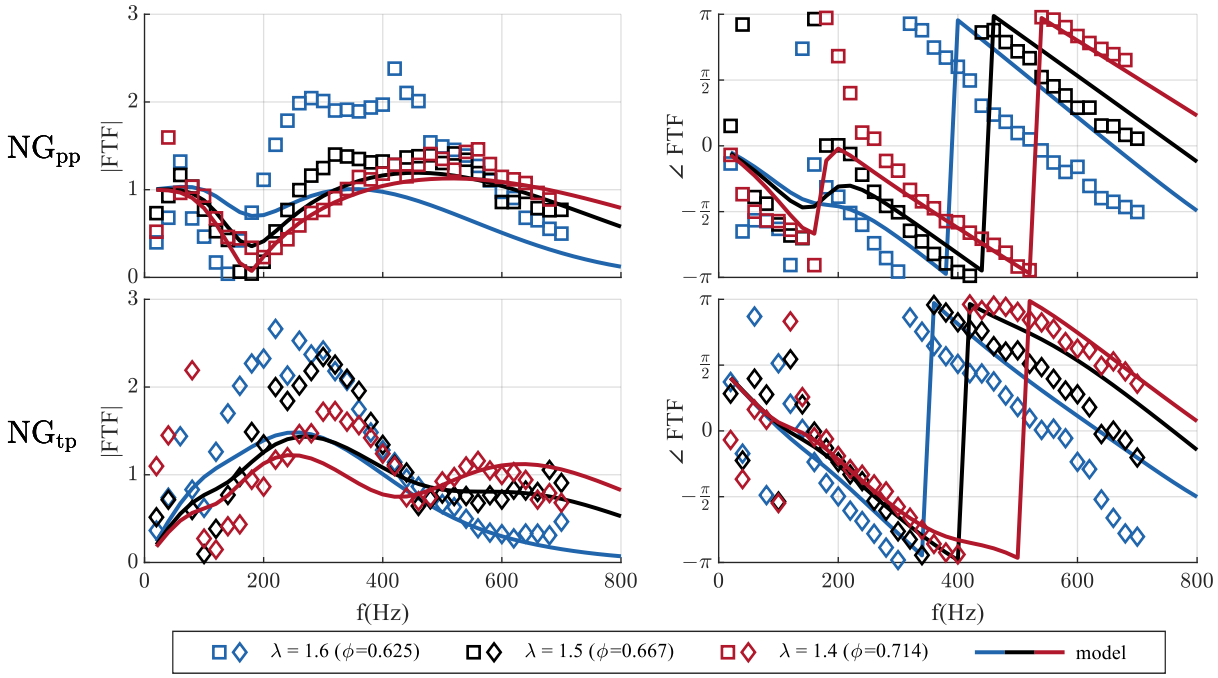


**Figure A.4:** Comparison of predicted FTF and experimental data of the $NG_{pp}$- and $NG_{tp}$-configuration from Bade [6] for different equivalence ratios at constant thermal power $P_{th}$ = 50 kW.

## A.4 FTF and Analytical Model Applied to an Industrial Burner Design

In addition to the A$^2$EV burner, the analytical model approach described in Chapter 7 is applied to an industrial burner design to decompose the FTF. The industrial burner is a GE15 dry low $NO_x$ fuel nozzle, which can be operated with natural gas in perfectly ($NG_{pp}$) and technically premixed mode ($NG_{tp}$) or with kerosene in diffusion mode. Figure A.5 schematically shows the plenum and combustion chamber sections of the test rig as presented in Figure 3.1 with the industrial burner installed.

The main part of the burner is a cylindrical tube with a constant diameter positioned ahead of the combustion chamber inlet. This tube is equipped with swirler blades and a central nozzle for liquid fuel injection. Natural gas is supplied through small holes in the swirler blades in $NG_{tp}$ operation. Liquid fuel operation is realized via an air assisted atomizer with five injection orifices at the nozzle tip, thus resulting in a non-axisymmetric diffusion flame. To ensure an acoustically clean measurement section, the interface for fuel and atomizing air supply is situated upstream of the pressure transducers. The fuel lance is connected to the plenum walls by three thin pins at the upstream mount to minimize its impact on the acoustic field.

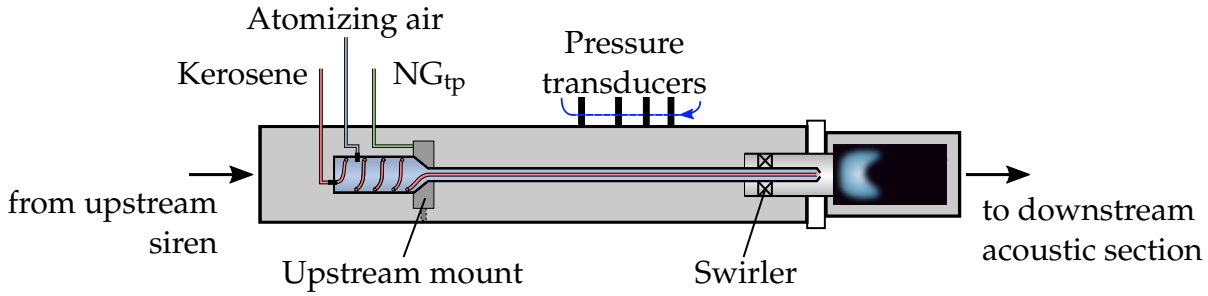


**Figure A.5:** Test rig plenum with industrial burner.

Analogous to the procedure from Chapter 7, a set of scaling rules is derived to consistently calculate the model parameters based on the flame geometry for the entire operating range. The model is applied to perfectly and technically premixed combustion for variations of equivalence ratio

and main air mass flow. Figures A.6-A.9 show that the experimental data can be reproduced very well over the entire operating range.

Similar to the results for the A$^2$EV burner, the model could not be applied to the results for kerosene combustion due to the diffusive combustion character. The FTF results for kerosene are presented without a model at the end of this section in Figure A.10.

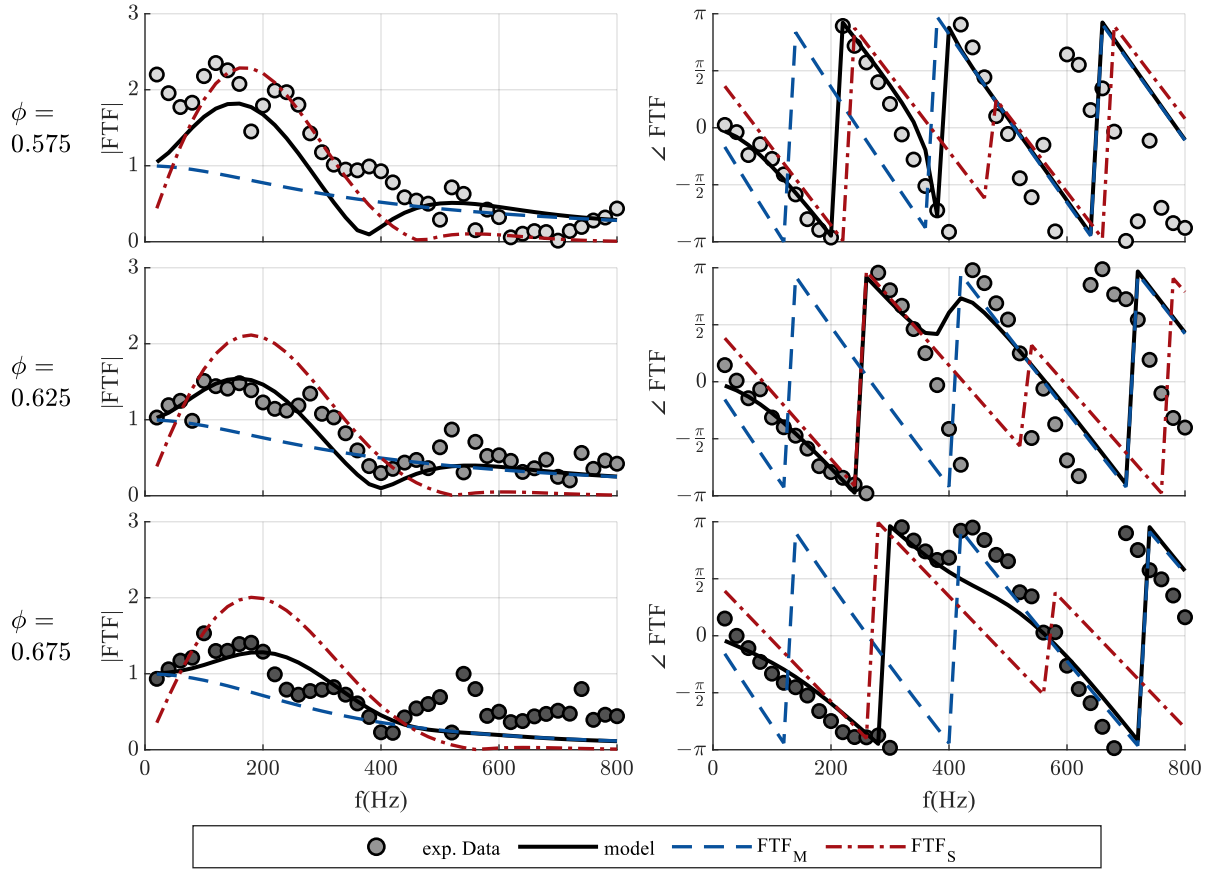


**Figure A.6:** Comparison of model FTF and experimental data of the NG$_{pp}$-configuration of the industrial burner for different equivalence ratios at constant air mass flow $\dot{m}_{air}$ = 35 $g/s$.

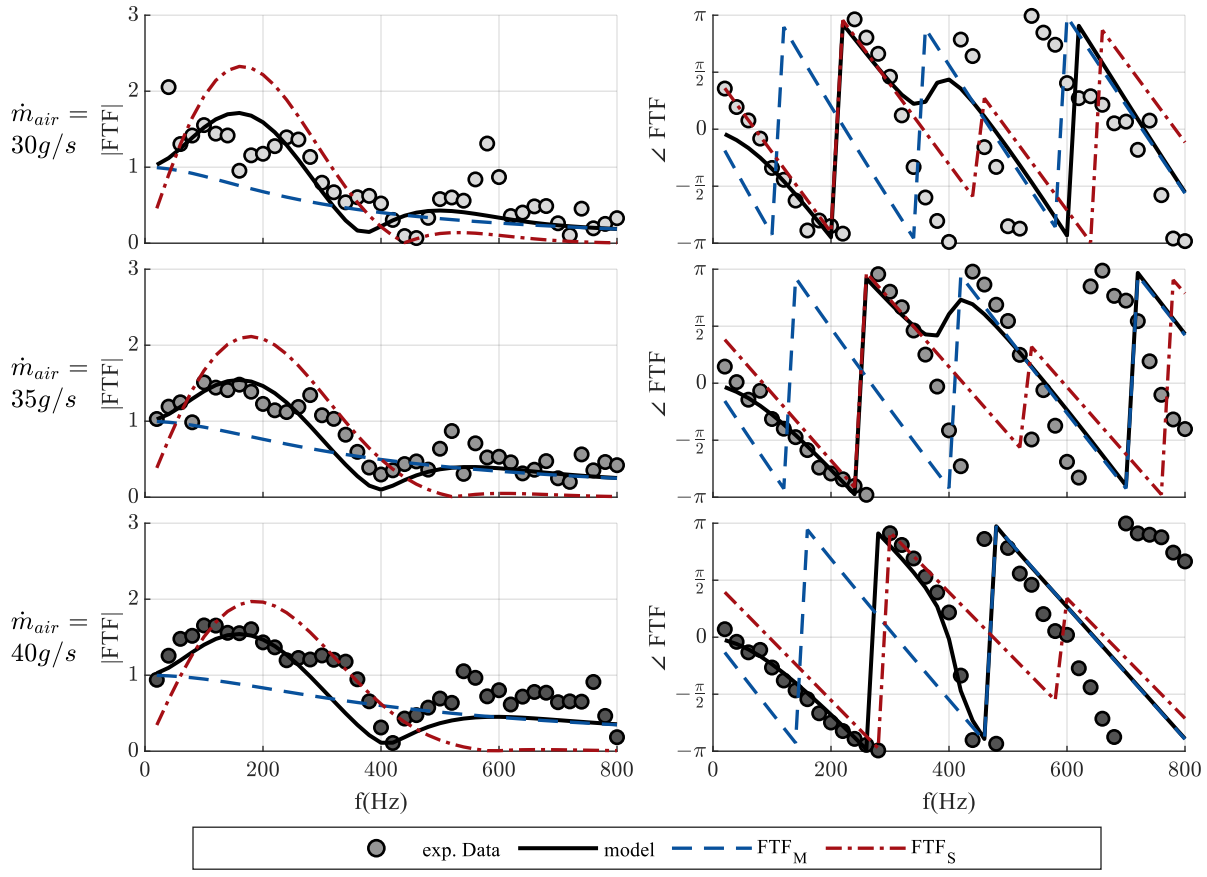


**Figure A.7:** Comparison of model FTF and experimental data of the $NG_{pp}$-configuration of the industrial burner for different air mass flows at constant equivalence ratio $\phi$ = 0.625.

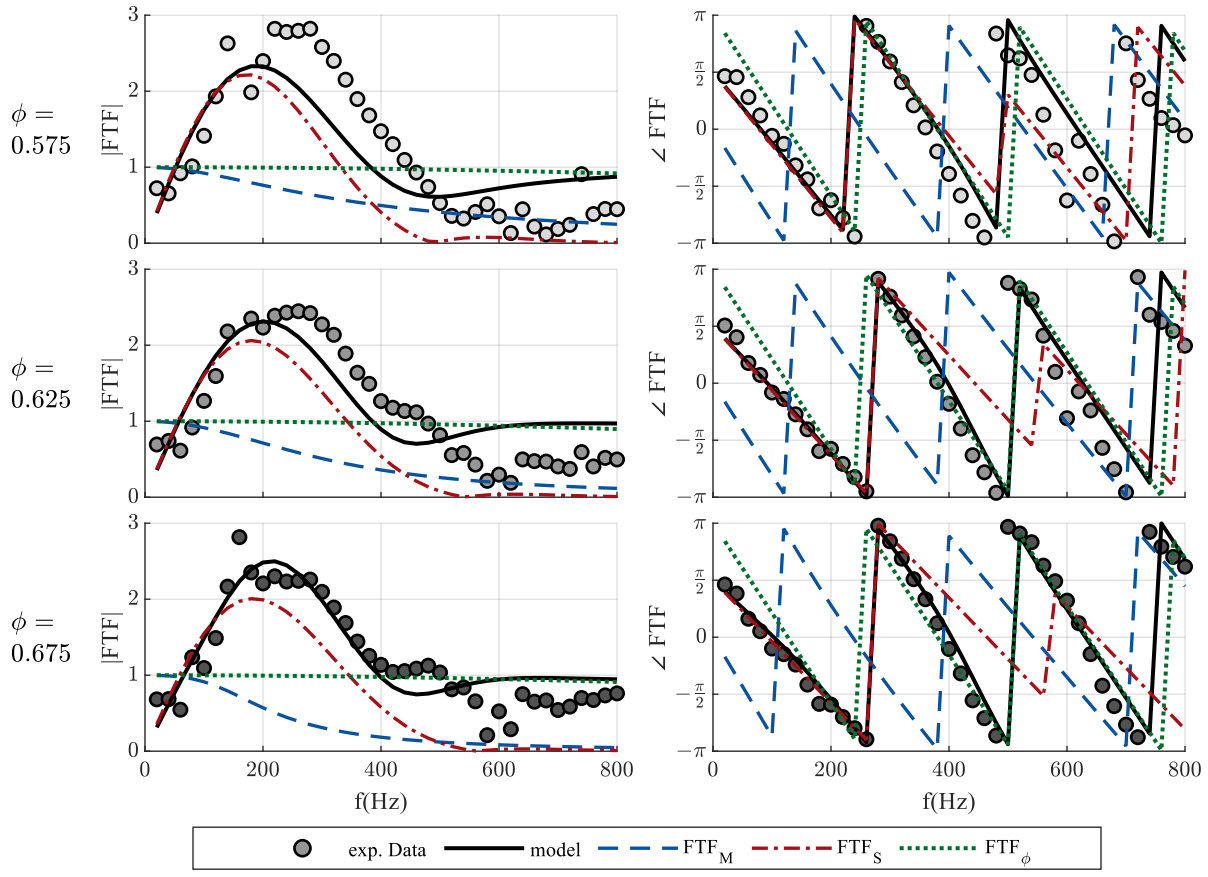


**Figure A.8:** Comparison of model FTF and experimental data of the $NG_{tp}$-configuration of the industrial burner for different equivalence ratios at constant air mass flow $\dot{m}_{air}$ = 35 $g/s$.

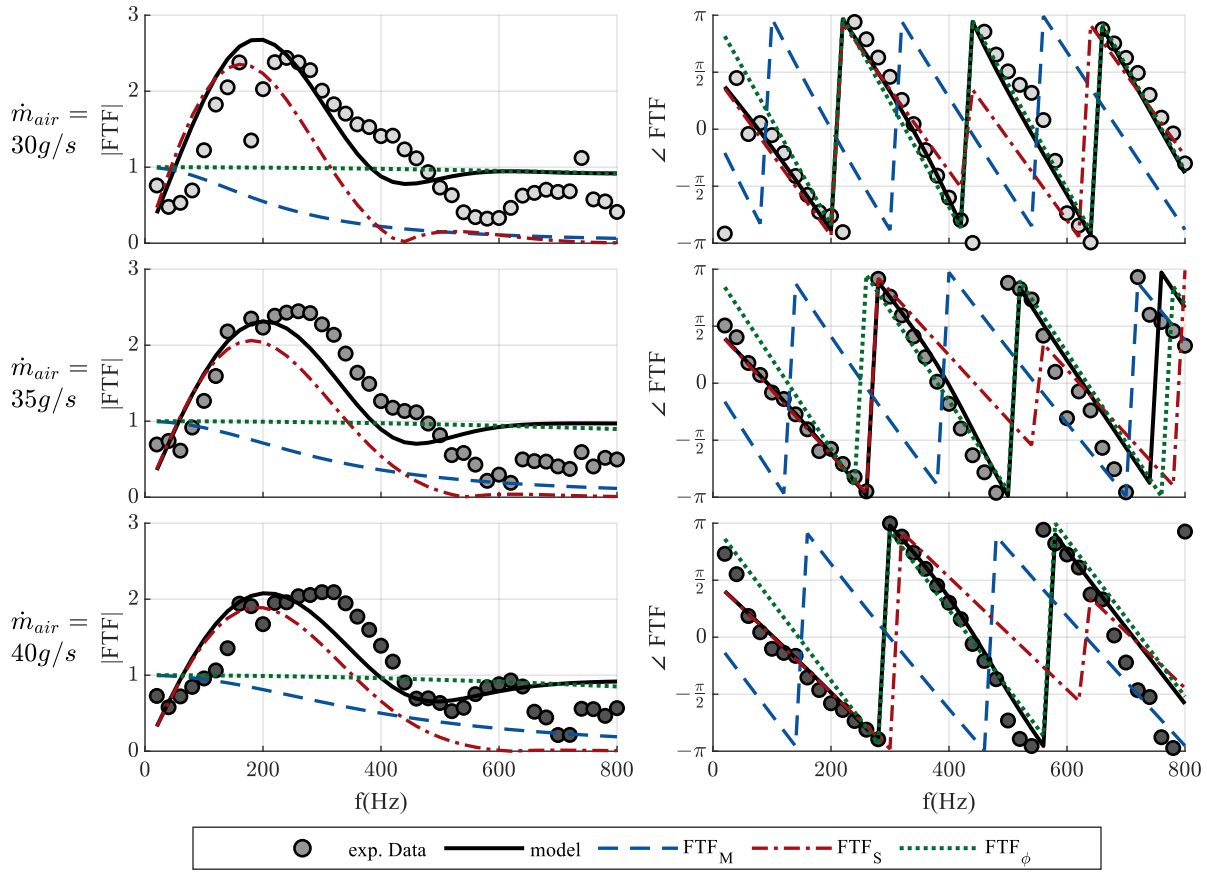


**Figure A.9:** Comparison of model FTF and experimental data of the $NG_{tp}$-configuration of the industrial burner for different air mass flows at constant equivalence ratio $\phi$ = 0.625.

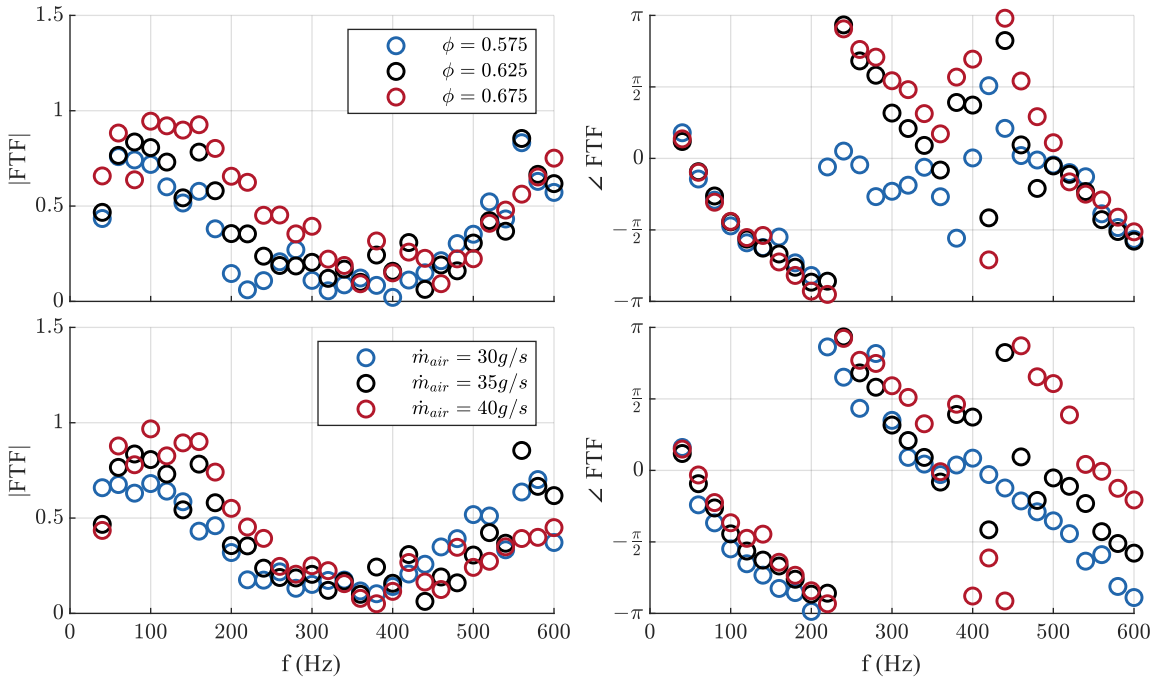


**Figure A.10:** Experimental FTF data of the kerosene configuration of the industrial burner for different air mass flows at constant equivalence ratio $\phi$ = 0.625 and different equivalence ratios at constant air mass flow $\dot{m}_{air}$ = 35 $g/s$.

# Previous Publications

Parts of this Ph.D. thesis have been published by the author beforehand in journal papers or are currently submitted as conference contributions. All of these prior printed publications are registered according to the valid doctoral regulations and listed below. Therefore, they are not necessarily quoted explicitly in the text. Whether they were referenced, depended on maintaining comprehensibility and providing all necessary context. All publications are listed below:

- Vogel, M. Bachfischer, M., Kaufmann, J., Sattelmayer T. Experimental investigation of equivalence ratio fluctuations in a lean premixed kerosene combustor. *Experiments in Fluids* 62, 5 (2021), 93.

- Vogel, M. Bachfischer, M., Kaufmann, J., Sattelmayer T. Optical equivalence ratio measurement of a dual fuel burner for natural gas and kerosene. *Fluids* 7, 2 (2022), 43.

- Kaufmann, J. Vogel, M., Papenbrock, J., Sattelmayer T. Comparison of the flame dynamics of a premixed dual fuel burner for kerosene and natural gas. *International Journal of Spray and Combustion Dynamics* 14, 1-2 (2022), 176-185.

- Kaufmann, J., Vogel, M., Sattelmayer T. Comparison of the flame dynamics of a liquid fueled swirl stabilized combustor for different degrees of fuel-air premixing. In *Proceedings of the ASME Turbo Expo* (Boston, Massachusetts, USA , 2023), GT2023-102448. *Recommended for publication in Journal of Engineering for Gas Turbines and Power*.

- Vogel, M., Kaufmann, J., Völkl, V., Hirsch, C., Sattelmayer T. Comparison of equivalence ratio fluctuations in a lean premixed combustor for kerosene and natural gas. In *Proceedings of the ASME Turbo Expo* (Boston, Massachusetts, USA , 2023), GT2023-101091.
- Tony, J., Magina, N., Han, F., Kaufmann, J., Vogel, M., Sattelmayer T. Modeling Flame Transfer Functions of an Industrial Premixed Burner. In *Proceedings of the ASME Turbo Expo* (Boston, Massachusetts, USA , 2023), GT2023-103246. *Recommended for publication in Journal of Engineering for Gas Turbines and Power*.

# Supervised Student Theses

Associated with this Ph.D. thesis, a number of student theses were supervised by the author of the present work. These were prepared at the Chair of Thermodynamics at the Technical University of Munich in the years 2017 to 2022 under the close supervision of the author. Parts of these supervised theses may be incorporated into the present thesis. The author would like to express his sincere gratitude to all formerly supervised students for their commitment and support of this research project.

| Name | Title / Thesis |
|---|---|
| Ziqi Liu | Commissioning and Characterization of a Static Mixer for the Production of Water-in-Kerosene Emulsions in terms of Stability, Bachelor's Thesis, September 2018 |
| Benedikt Xaver Scholz | Dimensioning and Design of a Unit for Investigating the Local Air/Fuel-Equivalence-Ratio of the Fresh Gas Flow in a Combustion Chamber Operated on Jet A, Semester Thesis, November 2018 |
| Muhammad Yasir | Thermoacoustic Characterization of a Single Burner Gas Turbine Combustor, Master's Thesis, January 2020 |
| Philipp Lober | Experimentelle Untersuchung zum Einfluss von Schwankungen der Gemischzusammensetzung auf die Stabilität von Sprayverbrennung, Bachelor's Thesis, October 2020 |
| Karsten Feigl | Anpassung und Inbetriebnahme eines Einzelbrennerversuchsstandes zur Untersuchung thermoakustischer Verbrennungsinstabilitäten unter besonderer Berücksichtigung des Einflusses der Betriebsparameter auf die akustischen Eigenschaften, October 2020 |
| Hartmann Hofer | Experimentelle Untersuchung der Stickoxidemissionen bei mager-vorgemischter Verbrennung unter Variation von Brennstoff und Betriebsparametern, Bachelor's Thesis, November 2021 |
| Marvin Philip Schroff | Erweiterung einer Methode zur Bestimmung der Brennkammer- und Flammentemperatur auf Basis thermoakustischer Messungen, Bachelor's Thesis, November 2021 |
| Ingy Tag Eldin | Charakterisierung der Sprayqualität von zwei Kerosininjektoren für Gasturbinen, Bachelor's Thesis, March 2022 |
| Paul Siegele | Analyse thermoakustischer Verbrennungsinstabilitäten mager-vorgemischter Drallflammen mittels Proper Orthogonal Decomposition, Bachelor's Thesis, August 2022 |

# Bibliography


[1] ÅBOM, M. A note on the experimental determination of acoustical two-port matrices. *Journal of Sound and Vibration 155*, 1 (1992), 185–188.

[2] ÅBOM, M., AND BODÉN, H. Error analysis of two-microphone measurements in ducts with flow. *The Journal of the Acoustical Society of America 83*, 6 (1988), 2429–2438.

[3] ACHURY, J., AND POLIFKE, W. Modulation of spray droplet number density and size distribution by an acoustic field. *The Journal of Computational Multiphase Flows 9*, 1 (2017), 32–46.

[4] AKIMOTO, H. *Atmospheric reaction chemistry*. Springer, Tokyo, 2016.

[5] ALEMELA, P. R., FANACA, D., HIRSCH, C., SATTELMAYER, T., AND SCHUERMANS, B. Determination and scaling of thermo acoustic characteristics of premixed flames. *International Journal of Spray and Combustion Dynamics 2*, 2 (2010), 169–198.

[6] BADE, S. *Messung und Modellierung der thermoakustischen Eigenschaften eines modularen Brennersystems für vorgemischte Drallflammen*. PhD thesis, Technical University of Munich, 2014.

[7] BADE, S., WAGNER, M., HIRSCH, C., SATTELMAYER, T., AND SCHUERMANS, B. Design for thermo-acoustic stability: Procedure and database. *Journal of Engineering for Gas Turbines and Power 135*, 12 (2013), 121507.

[8] BAUERHEIM, M., NICOUD, F., AND POINSOT, T. Progress in analytical methods to predict and control azimuthal combustion instability modes in annular chambers. *Physics of Fluids 28*, 2 (2016), 021303.

[9] CARVALHO JR, J., MCQUAY, M., AND GOTAC, P. The interaction of liquid reacting droplets with the pulsating flow in a Rijke-tube combustor. *Combustion and Flame 108*, 1-2 (1997), 87–103.

[10] CHATTERJEE, A. An introduction to the proper orthogonal decomposition. *Current Science 78*, 7 (2000), 808–817.

[11] CHISHTY, W. A. *Effects of thermoacoustic oscillations on spray combustion dynamics with implications for lean direct injection systems*. PhD thesis, Virginia Polytechnic Institute and State University, 2005.

[12] CHO, J. H., AND LIEUWEN, T. C. Modeling the response of premixed flames to mixture ratio perturbations. In *Proceedings of the ASME Turbo Expo* (Atlanta, Georgia, USA, 2003), GT2003-38089.

[13] CHRISTOU, T., STELZNER, B., AND ZARZALIS, N. Influence of an oscillating airflow on the prefilming airblast atomization process. *Atomization and Sprays 31*, 3 (2021), 1–14.

[14] CHU, B.-T. On the generation of pressure waves at a plane flame front. *Symposium (International) on Combustion 4*, 1 (1953), 603–612.

[15] CLAVIN, P., AND SIGGIA, E. D. Turbulent premixed flames and sound generation. *Combustion Science and Technology 78*, 1-3 (1991), 147–155.

[16] ĆOSIĆ, B., REISS, F., BLÜMER, M., FREKERS, C., GENIN, F., PÄHR, J., AND WASSMER, D. Development and integration of the dual fuel combustion system for the MGT gas turbine family. *Journal of Engineering for Gas Turbines and Power 144*, 2 (2022), 021021.

[17] Ćosić, B., Terhaar, S., Moeck, J. P., and Paschereit, C. O. Response of a swirl-stabilized flame to simultaneous perturbations in equivalence ratio and velocity at high oscillation amplitudes. *Combustion and Flame 162*, 4 (2015), 1046–1062.

[18] Crocco, L., and Cheng, S.-I. *Theory of combustion instability in liquid propellant rocket motors*. Butterworths Science Publication, London, 1956.

[19] Culick, F. E. Combustion instabilities in liquid-fuelled propulsion systems. In *AGARD Conference Proceedings* (1988), vol. 450, 1-73.

[20] Dowling, A. P. The calculation of thermoacoustic oscillations. *Journal of sound and vibration 180*, 4 (1995), 557–581.

[21] Dowling, A. P. Nonlinear self-excited oscillations of a ducted flame. *Journal of Fluid Mechanics 346* (1997), 271–290.

[22] Dowling, A. P. A kinematic model of a ducted flame. *Journal of Fluid Mechanics 394* (1999), 51–72.

[23] Ducruix, S., Schuller, T., Durox, D., and Candel, S. Combustion dynamics and instabilities: Elementary coupling and driving mechanisms. *Journal of Propulsion and Power 19*, 5 (2003), 722–734.

[24] Durox, D., Schuller, T., and Candel, S. Combustion dynamics of inverted conical flames. *Proceedings of the Combustion Institute 30*, 2 (2005), 1717–1724.

[25] Eckstein, J. *On the mechanisms of combustion driven low-frequency oscillations in aero-engines*. PhD thesis, Technical University of Munich, 2004.

[26] Eckstein, J., Freitag, E., Hirsch, C., and Sattelmayer, T. Experimental study on the role of entropy waves in low-frequency oscillations in a RQL combustor. *Journal of Engineering for Gas Turbines and Power 128*, 2 (2004), 264–270.

[27] ECKSTEIN, J., FREITAG, E., HIRSCH, C., SATTELMAYER, T., VON DER BANK, R., AND SCHILLING, T. Forced low-frequency spray characteristics of a generic airblast swirl diffusion burner. *Journal of Engineering for Gas Turbines and Power 127*, 2 (2005), 301–306.

[28] EL HOSSAINI, M. K. Review of the new combustion technologies in modern gas turbines. *Progress in Gas Turbine Performance* (2013), 978–953.

[29] EROGLU, A., FLOHR, P., BRUNNER, P., AND HELLAT, J. Combustor design for low emissions and long lifetime requirements. In *Proceedings of the ASME Turbo Expo* (Orlando, Florida, USA, 2009), GT2009-59540.

[30] FANACA, D. *Influence of burner-burner interactions on the flame dynamics in an annular combustor*. PhD thesis, Technical Univesity of Munich, 2010.

[31] FANACA, D., ALEMELA, P. R., ETTNER, F., HIRSCH, C., SATTELMAYER, T., AND SCHUERMANS, B. Determination and comparison of the dynamic characteristics of a perfectly premixed flame in both single and annular combustion chambers. In *Proceedings of the ASME Turbo Expo* (Berlin, Germany, 2008), GT2008-50781.

[32] FISCHER, A. *Hybride, thermoakustische Charakterisierung von Drallbrennern*. PhD thesis, Technical University of Munich, 2004.

[33] FREITAG, E. *On the measurement and modeling of flame transfer functions at elevated pressure*. PhD thesis, Technical University of Munich, 2009.

[34] GÜLEN, S. C., AND CURTIS, M. Gas turbine's role in energy transition. In *Proceedings of the ASME Turbo Expo* (Rotterdam, The Netherlands, 2022), GT2022-81802.

[35] GURUBARAN, R. K., AND SUJITH, R. I. Dynamics of spray - swirl - acoustics interactions. *International Journal of Spray and Combustion Dynamics 3*, 1 (2011), 1–22.

[36] HAUSER, M. W. *Zum Einfluss transversaler akustischer Anregung auf die Dynamik turbulenter vorgemischter Drallflammen*. PhD thesis, Technical University of Munich, 2014.

[37] HIRSCH, C., FANACA, D., REDDY, P., POLIFKE, W., AND SATTELMAYER, T. Influence of the swirler design on the flame transfer function of premixed flames. In *Proceedings of the ASME Turbo Expo* (Reno, Nevada, USA, 2005), GT2005-68195.

[38] HUANG, Y., AND YANG, V. Dynamics and stability of lean-premixed swirl-stabilized combustion. *Progress in Energy and Combustion Science 35*, 4 (2009), 293–364.

[39] IPCC. *Climate Change 2013 - The Pysical Science Basis*. Cambridge University Press, 2014.

[40] KELLER, J. J. Thermoacoustic oscillations in combustion chambers of gas turbines. *AIAA journal 33*, 12 (1995), 2280–2287.

[41] KELLER, J. J., EGLI, W., AND HELLAT, J. Thermally induced low-frequency oscillations. *Journal of Applied Mathematics and Physics 36*, 2 (mar 1985), 250–274.

[42] KIM, K. I., JUNG, K., AND KIM, H. J. Face recognition using kernel principal component analysis. *IEEE Signal Processing Letters 9*, 2 (2002), 40–42.

[43] KIM, K. T., LEE, J. G., QUAY, B., AND SANTAVICCA, D. Spatially distributed flame transfer functions for predicting combustion dynamics in lean premixed gas turbine combustors. *Combustion and Flame 157*, 9 (2010), 1718–1730.

[44] KLIMCZAK, D. Influence of Ukrainian crisis on the European gas market. *Energy & Environment 26*, 3 (2015), 425–435.

[45] KOMAREK, T., AND POLIFKE, W. Impact of swirl fluctuations on the flame response of a perfectly premixed swirl burner. *Journal of Engineering for Gas Turbines and Power 132*, 6 (2010), 061503.

[46] KOROSTELEVA, J. The implications of Russia's invasion of Ukraine for the EU energy market and businesses. *British Journal of Management 33*, 4 (2022), 1678–1682.

[47] KUNZE, K. *Untersuchung des thermoakustischen Flammenübertragungsverhaltens in einer Ringbrennkammer*. PhD thesis, Technical University of Munich, 2003.

[48] LECHNER, C., AND SEUME, J. *Stationäre Gasturbinen*. Springer, Berlin, Heidelberg, 2010.

[49] LEE, J. C. Y., MALTE, P. C., AND BENJAMIN, M. A. Low NOx combustion for liquid fuels: Atmospheric pressure experiments using a staged prevaporizer-premixer. *Journal of Engineering for Gas Turbines and Power 125*, 4 (2003), 861–871.

[50] LEFEBVRE, A. H., AND MCDONELL, V. G. *Atomization and sprays*. CRC Press, Boca Raton, Florida, USA, 2017.

[51] LEFEVBRE, AND BALLAL. *Gas turbine combustion*. CRC Press, Boca Raton, Florida, USA, 1998.

[52] LIEUWEN, T., AND ZINN, B. T. The role of equivalence ratio oscillations in driving combustion instabilities in low NOx gas turbines. *Symposium (International) on Combustion 27*, 2 (1998), 1809–1816.

[53] LIEUWEN, T. C. *Unsteady combustor physics*. Cambridge University Press, Cambridge, United Kingdom, 2012.

[54] LIEUWEN, T. C., AND YANG, V. *Combustion instabilities in gas turbine engines*. American Institute of Aeronautics and Astronautics, Reston, Virginia, USA, 2006.

[55] LINDMAN, O., ANDERSSON, M., PERSSON, M., AND MUNKTELL, E. Development of a liquid fuel combustion system for SGT-750. In *Proceedings of the ASME Turbo Expo* (Düsseldorf, Germany, 2014), GT2014-25380.

[56] LOHRMANN, M., AND BÜCHNER, H. Scaling of stability limits in lean-premixed gas turbine combustors. In *Proceedings of the ASME Turbo Expo* (Vienna, Austria, 2004), GT2004-53710.

[57] LUMLEY, J. L. Stochastic tools in turbulence. *Journal of Fluid Mechanics 67*, 2 (1975), 413–415.

[58] MACIAS, F. M., HIRSCH, C., SATTELMAYER, T., HUTH, M., AND MEISL, J. Investigating the mixture quality in multi-injector burner systems - part I: Experimental setup. *Journal of Engineering for Gas Turbines and Power 144*, 12 (2022), 121008.

[59] MARBLE, F., AND CANDEL, S. Acoustic disturbance from gas nonuniformities convected through a nozzle. *Journal of Sound and Vibration 55*, 2 (1977), 225–243.

[60] MARCH, M., RENNER, J., HIRSCH, C., AND SATTELMAYER, T. Design and validation of a novel test-rig for RQL flame dynamics studies. In *Proceedings of the ASME Turbo Expo* (Virtual Venue, 2021), GT2021-58602.

[61] MAYER, C. *Konzept zur vorgemischten Verbrennung wasserstoffhaltiger Brennstoffe in Gasturbinen*. PhD thesis, Technical University of Munich, 2012.

[62] MUNJAL, M., AND DOIGE, A. Theory of a two source-location method for direct experimental evaluation of the four-pole parameters of an aeroacoustic element. *Journal of Sound and Vibration 141*, 2 (1990), 323–333.

[63] MUNJAL, M. L. *Acoustics of ducts and mufflers*. John Wiley & Sons, 1987.

[64] NARASIMHA, R. Kosambi and proper orthogonal decomposition. *Resonance 16*, 6 (2011), 574–581.

[65] O'CONNOR, J., ACHARYA, V., AND LIEUWEN, T. Transverse combustion instabilities: Acoustic, fluid mechanic, and flame processes. *Progress in Energy and Combustion Science 49* (2015), 1–39.

[66] PASCHEREIT, C., GUTMARK, E., AND WEISENSTEIN, W. Structure and control of thermoacoustic instabilities in a gas-turbine combustor. *Combustion Science and Technology 138*, 1-6 (1998), 213–232.

[67] PASCHEREIT, C. O., SCHUERMANS, B., POLIFKE, W., AND MATTSON, O. Measurement of transfer matrices and source terms of premixed flames. *Journal of Engineering for Gas Turbines and Power 124*, 2 (2002), 239–247.

[68] PEARSON, K. On lines and planes of closest fit to systems of points in space. *The London, Edinburgh, and Dublin Philosophical Magazine and Journal of Science 2*, 11 (1901), 559–572.

[69] POINSOT, T. J., TROUVE, A. C., VEYNANTE, D. P., CANDEL, S. M., AND ESPOSITO, E. J. Vortex-driven acoustically coupled combustion instabilities. *Journal of Fluid Mechanics 177* (1987), 265–292.

[70] POLIFKE, W. Combustion instabilities. *VKI Lecture Series: Advances in aeroacoustics and applications 5* (2004), 1–44.

[71] POLIFKE, W., AND LAWN, C. On the low-frequency limit of flame transfer functions. *Combustion and Flame 151*, 3 (2007), 437–451.

[72] POLIFKE, W., PASCHEREIT, C. O., AND PASCHEREIT, K. Constructive and destructive interference of acoustic and entropy waves in a premixed combustor with a choked exit. *The International Journal of Acoustics and Vibration 6*, 3 (2001), 135–146.

[73] RACHNER, M. Die Stoffeigenschaften von Kerosin Jet A-1. Tech. rep., Deutsches Zentrum für Luft- und Raumfahrt, 1998.

[74] RAYLEIGH. The explanation of certain acoustical phenomena. *Nature 18*, 455 (1878), 319–321.

[75] RENNER, J., MARCH, M., HIRSCH, C., AND SATTELMAYER, T. Flame dynamics in the lean burnout zone of an RQL combustion chamber - response to primary zone velocity fluctuations. *International Journal of Spray and Combustion Dynamics 14*, 3-4 (2022), 238–250.

[76] RICHARDS, G. A., AND JANUS, M. C. Characterization of oscillations during premix gas turbine combustion. *Journal of Engineering for Gas Turbines and Power 120*, 2 (1998), 294–302.

[77] SANGL, J., MAYER, C., AND SATTELMAYER, T. Dynamic adaptation of aerodynamic flame stabilization of a premix swirl burner to fuel reactivity using fuel momentum. *Journal of Engineering for Gas Turbines and Power 133*, 7 (2011), 071501.

[78] SATTELMAYER, T. Influence of the combustor aerodynamics on combustion instabilities from equivalence ratio fluctuations. *Journal of Engineering for Gas Turbines and Power 125*, 1 (2002), 11–19.

[79] SCHADOW, K., AND GUTMARK, E. Combustion instability related to vortex shedding in dump combustors and their passive control. *Progress in Energy and Combustion Science 18*, 2 (1992), 117–132.

[80] SCHUERMANS, B. *Modeling and control of thermoacoustic instabilities*. PhD thesis, Ecole Polytechnique Fédérale de Lausanne, 2003.

[81] SCHUERMANS, B., BELLUCCI, V., GUETHE, F., MEILI, F., FLOHR, P., AND PASCHEREIT, C. O. A detailed analysis of thermoacoustic interaction mechanisms in a turbulent premixed flame. In *Proceedings of the ASME Turbo Expo* (Vienna, Austria, 2004), GT2004-53831.

[82] SCHUERMANS, B., BOTHIEN, M., MAURER, M., AND BUNKUTE, B. Combined acoustic damping-cooling system for operational flexibility of GT26/GT24 reheat combustors. In *Proceedings of the ASME Turbo Expo* (Montreal, Quebec, Canada, 2015), GT2015-42287.

[83] SCHUERMANS, B. B. H., POLIFKE, W., AND PASCHEREIT, C. O. Modeling transfer matrices of premixed flames and comparison with experimental results. In *Proceedings of the ASME Turbo Expo* (Indianapolis, Indiana, USA, 1999), 99-GT-132.

[84] SCHULLER, T., DUROX, D., AND CANDEL, S. A unified model for the prediction of laminar flame transfer functions. *Combustion and Flame 134*, 1-2 (2003), 21–34.

[85] SHREEKRISHNA, HEMCHANDRA, S., AND LIEUWEN, T. Premixed flame response to equivalence ratio perturbations. *Combustion Theory and Modelling 14*, 5 (2010), 681–714.

[86] SNC-LAVALIN. Regulatory overview of natural gas fuelled turbine emissions - final report. Tech. rep., British Columbia Ministry of the Environment, 2013.

[87] STADLMAIR, N., AND SATTELMAYER, T. Measurement and analysis of flame transfer functions in a lean-premixed, swirl-stabilized combustor with water injection. In *54th AIAA Aerospace Sciences Meeting* (San Diego, California, USA, 2016), 2016-1157.

[88] STADLMAIR, N. V. *Influence of water injection on the thermoacoustic stability of a lean-premixed combustor*. PhD thesis, Technical University of Munich, 2016.

[89] STEINBACH, C., RUCK, T., LLOYD, J., JANSOHN, P., DÖBBELING, K., SATTELMAYER, T., AND STRAND, T. ABB's advanced EV burner - a dual fuel dry low NOx burner for stationary gas turbines. In *Proceedings of the ASME Turbo Expo* (Stockholm, Sweden, 1998), 98-GT-519.

[90] STEINBACHER, T., MEINDL, M., AND POLIFKE, W. Modelling the generation of temperature inhomogeneities by a premixed flame. *International Journal of Spray and Combustion Dynamics 10*, 2 (2017), 111–130.

[91] STRAHLE, W. C. On combustion generated noise. *Journal of Fluid Mechanics 49*, 2 (1971), 399–414.

[92] SUJITH, R. I. An experimental investigation of interaction of sprays with acoustic fields. *Experiments in Fluids 38*, 5 (2005), 576–587.

[93] TURNS, S. *An Introduction to combustion: Concepts and applications*. McGraw-Hill series in mechanical engineering. McGraw-Hill, Boston, USA, 2012.

[94] VOGEL, M. *Determination of equivalence ratio fluctuations in a lean premixed dual fuel gas turbine combustor*. PhD thesis, Technical University of Munich, 2023.

[95] VOGEL, M., BACHFISCHER, M., KAUFMANN, J., AND SATTELMAYER, T. Experimental investigation of equivalence ratio fluctuations in a lean premixed kerosene combustor. *Experiments in Fluids 62*, 5 (2021), 93.

[96] VOGEL, M., KAUFMANN, J., VÖLKL, V., HIRSCH, C., AND SATTELMAYER, T. Comparison of equivalence ratio fluctuations in a lean premixed combustor for kerosene and natural gas. In *Proceedings of the ASME Turbo Expo* (Boston, Massachussetts, USA, 2023), GT2023-101091.

[97] WEBER, M., SONG, J., AND LEE, J. G. Characterization of dynamics of unstable fuel-rich flame. In *Proceedings of the ASME Turbo Expo* (Virtual Venue, 2021), GT2021-60121.

[98] WU, C., LIANG, Y., LIN, W., LEE, H., AND LIM, S. A note on equivalence of proper orthogonal decomposition methods. *Journal of Sound and Vibration 265*, 5 (aug 2003), 1103–1110.

[99] ZAHN, M. *Vorhersage und Optimierung des thermoakustischen Stabilitätsverhaltens von Ringbrennkammern unter Einsatz passiver Dämpfer*. PhD thesis, Technical University of Munich, 2018.

[100] ZUCCA, A., KHAYRULIN, S., VYAZEMSKAYA, N., SHERSHNYOV, B., AND MYERS, G. Development of a liquid fuel system for GE MS5002E gas turbine: Rig test validation of the combustor performance. In *Proceedings of the ASME Turbo Expo* (Düsseldorf, Germany, 2014), GT2014-26046.